



ETH Institute for  
Particle Physics

ETHZ-IPP-2009-07

# Elastic $J/\psi$ Production at low $Q^2$ at HERA

FLORIAN HUBER

**Diploma Thesis**

supervised by  
Prof. Dr. Christoph Grab

Tutor: Michel Sauter

SWISS FEDERAL INSTITUTE OF TECHNOLOGY  
ZURICH

February 2009



## Abstract

In this diploma thesis the elastic  $J/\psi$  vector meson photoproduction ( $ep \rightarrow eJ/\psi p$ ) is studied in the decay channel  $J/\psi \rightarrow e^+e^-$  with the H1 detector at the electron proton collider HERA. The data from the runs of the year 2007 with an integrated luminosity of  $62.4 \text{ pb}^{-1}$  are used. In this time HERA operated with three different proton energies  $E_p$  called high (920 GeV), medium (575 GeV) and low (460 GeV) with integrated luminosities 45.5 (high), 5.96 (medium) and  $10.9 \text{ pb}^{-1}$  (low). The kinematical region of  $|t| < 1.2 \text{ GeV}^2$ , where  $t$  is the four momentum transfer at the proton vertex, and  $Q_e^2 < 1 \text{ GeV}$  (photoproduction) is used. Further the range of the centre of mass energy in the photon proton rest frame,  $W_{\gamma p}$ , is restricted to  $40 \text{ GeV} < W_{\gamma p} < 110 \text{ GeV}$  (high),  $20 \text{ GeV} < W_{\gamma p} < 80 \text{ GeV}$  (medium) and  $20 \text{ GeV} < W_{\gamma p} < 100 \text{ GeV}$  (low). The differential cross section as a function of  $|t|$  is well described by an exponential,  $d\sigma/d|t| \propto e^{-b_0|t|}$ , which yields to  $b_0 = 4.4 \pm 0.2(\text{stat.})$ . The cross section as a function of  $W_{\gamma p}$  is fitted by a power law,  $d\sigma/dW_{\gamma p} \propto W_{\gamma p}^\delta$ , and gives  $\delta = 0.66 \pm 0.07(\text{stat.})$ .

## Kurzfassung

In dieser Diplomarbeit wurde die elastische  $J/\psi$  Vektormeson-Photoproduktion ( $ep \rightarrow eJ/\psi p$ ) im Zerfallskanal  $J/\psi \rightarrow e^+e^-$  mit dem H1 Detektor beim Elektron Proton Kollider HERA studiert. Die Daten aus der Laufzeit vom Jahr 2007 mit einer integrierten Luminosität von  $62.4 \text{ pb}^{-1}$  wurden benutzt. In dieser Zeit arbeitete HERA mit drei verschiedenen Protonenenergien  $E_p$ , genannt hoch (920 GeV), mittel (575 GeV) und tief (460 GeV) mit integrierten Luminositäten 45.5 (hoch), 5.96 (mittel) und  $10.9 \text{ pb}^{-1}$  (tief). Die kinematische Region  $|t| < 1.2 \text{ GeV}^2$ , wobei  $t$  der Viererimpulsübertrag beim Proton Vertex ist, und  $Q_e^2 < 1 \text{ GeV}$  (Photoproduktion) wurde benutzt. Ausserdem wurde der Bereich der Schwerpunktsenergie im Photon Proton Ruhesystem,  $W_{\gamma p}$ , eingeschränkt auf  $40 \text{ GeV} < W_{\gamma p} < 110 \text{ GeV}$  (hoch),  $20 \text{ GeV} < W_{\gamma p} < 80 \text{ GeV}$  (mittel) und  $20 \text{ GeV} < W_{\gamma p} < 100 \text{ GeV}$  (tief). Der differentielle Wirkungsquerschnitt als Funktion von  $|t|$  ist gut beschrieben durch eine Exponentialfunktion,  $d\sigma/d|t| \propto e^{-b_0|t|}$ , welches zu  $b_0 = 4.4 \pm 0.2(\text{stat.})$  führt. Der Wirkungsquerschnitt als Funktion von  $W_{\gamma p}$  ist bestimmt durch eine Potenzfunktion,  $d\sigma/dW_{\gamma p} \propto W_{\gamma p}^\delta$ , und ergibt  $\delta = 0.66 \pm 0.07(\text{stat.})$ .



# Contents

<b>1</b>	<b>Introduction</b>	<b>7</b>
<b>2</b>	<b>Theory</b>	<b>11</b>
2.1	Kinematic Variables of Electron Proton Scattering . . . . .	11
2.2	Characterisation of $J/\psi$ Production . . . . .	12
2.3	Models for Vector Meson Production . . . . .	13
2.4	Regge Theory . . . . .	14
2.5	Reconstruction of the Kinematic Variables . . . . .	16
2.6	Cross Section and Photon Flux . . . . .	16
<b>3</b>	<b>The H1 Detector at HERA</b>	<b>19</b>
3.1	The HERA Accelerator . . . . .	19
3.2	The H1 Detector . . . . .	20
3.2.1	Tracking . . . . .	21
3.2.2	Calorimetry, Muon and Forward Tagger System . . . . .	22
3.3	H1 Trigger System . . . . .	22
3.4	Fast Track Trigger (FTT) . . . . .	23
<b>4</b>	<b>Monte Carlo Simulation</b>	<b>25</b>
4.1	DiffVM generator . . . . .	26
4.2	Reweight MC . . . . .	26
4.3	Comparison of Monte Carlo with Data . . . . .	28
<b>5</b>	<b>Data Selection and Trigger</b>	<b>31</b>
5.1	Data Selection . . . . .	31
5.2	Trigger Conditions . . . . .	32
<b>6</b>	<b>Event Selection</b>	<b>33</b>
6.1	Extraction of $J/\psi$ candidates . . . . .	33
6.1.1	H1 Track Search Algorithm (Finder) . . . . .	34
6.1.2	H1 Elastic Track-Track $J/\psi$ Search Algorithm (Finder) . . . . .	34
6.1.3	Electron Identification . . . . .	34
6.1.4	Event Selection . . . . .	36
6.2	Phase Space of the Analysis . . . . .	36

---

6.3	Extract the Number of $J/\psi$ Events . . . . .	37
<b>7</b>	<b>Efficiencies</b>	<b>47</b>
7.1	Geometric Acceptance and Reconstruction Efficiency . . . . .	47
7.2	Selection Efficiency . . . . .	50
7.3	Combined Acceptance and Selection Efficiency . . . . .	53
7.4	Trigger Efficiency . . . . .	53
<b>8</b>	<b>Elastic Event Selection</b>	<b>59</b>
8.1	Forward Tagging . . . . .	59
8.2	Unfolding Procedure . . . . .	63
8.3	Forward Tagging Efficiencies . . . . .	64
<b>9</b>	<b>Cross Section Calculation and Results</b>	<b>67</b>
9.1	Systematic Uncertainties . . . . .	68
9.2	Summary . . . . .	71
<b>A</b>	<b>Bin Centre Correction</b>	<b>73</b>
<b>B</b>	<b>Kinematical limit for <math>Q^2</math></b>	<b>75</b>
<b>C</b>	<b>Minimal <math>W_{\gamma p}</math></b>	<b>77</b>
<b>D</b>	<b>Cross Section Values</b>	<b>79</b>
<b>E</b>	<b>Photon Flux Factors</b>	<b>81</b>
	<b>Bibliography</b>	<b>82</b>
	<b>Acknowledgements</b>	<b>87</b>

# Chapter 1

## Introduction

The Standard Model (SM) of particle physics, evolved and verified by many measurements, presents today the most accurate model to describe the matter and the fundamental interactions of nature. Within this framework two kinds of particles are distinguished fermions, which have half-integer spins, and gauge bosons with integer spins. Fermions are again divided in two groups: leptons and quarks. Whereas leptons, like electrons and positrons, are described as point like particles, baryones, like the stable protons, were found to have an inner structure.

The HERA accelerator was build as an electron proton collider to extend the knowledge of this inner structure of protons and also to test *Quantum Chromo Dynamics* (QCD), which describes the interaction of gluons, the self interacting carrier particles of the strong force, and quarks. For this purpose several detectors where constructed to detect the scattered particles after the collision. One of this detectors is H1, which has produced the data samples used in this thesis.

At hadron hadron interaction the class of so called *diffractive processes* were found, which eluded the description of *perturbative QCD* (pQCD) in phase space regions where no *hard scale*, for example a large momentum transfer at the electron ( $Q^2$ ) or the proton vertex ( $t$ ), exist. Instead a phenomenological model called *Regge theory* is used. In this model a so called *pomeron*, which only carries vacuum quantum numbers, and therefore is also colourless, is used as interacting particle.

Diffractive processes also occur by *ep*-scattering, which can be described by the *Vector Dominance Model* (VDM), for example by the exclusive vector meson production. Since in the *photoproduction* (in theory  $Q^2 = 0$ , but experimentally  $Q^2 < 1 \text{ GeV}^2$  is used) and at low momentum transfer at the proton vertex (low  $|t|$ ) region there is no hard scale available, description by the Regge theory will be performed.

In figure 1.1 the dependence of the *elastic* (the proton stays intact after the scattering) vector meson (VM) photoproduction cross section on the center of mass energy in the proton photon rest frame  $W_{\gamma p}$  is given for several vector mesons ( $\gamma p \rightarrow \gamma \text{VM} p$ ). But for the  $J/\psi$  VM still exists a gap between fix-target and earlier H1 measurements. The goal of this

thesis is to fill this gap by using H1 data from 2007 because in this time period also lower center of mass energies are available. The examined channel to reconstruction  $J/\psi$  events is  $J/\psi \rightarrow e^+e^-$ .

The next chapter gives an overview of the theoretical tools needed in this thesis. Chapter 3 introduces the H1 detector and its main parts, especially the components important for this thesis are discussed. The fourth chapter deals with the aspects of Monte Carlo simulation and reweighting of them. The data used for this analysis are discussed in chapter 5. Where also the trigger conditions are explained. Chapter 6 describes step by step the search algorithms and cuts used to select  $J/\psi$  candidates and also the extraction of the number of  $J/\psi$  events. The next chapter deals with aspects of inefficiencies, such as geometrical acceptance, reconstruction, selection and trigger efficiencies. In chapter 8 the procedure to separate elastic from inelastic events is described. And finally in the last chapter the (differential) elastic cross sections of  $J/\psi$  production as a function of  $|t|$  and  $W_{\gamma p}$  are given.

Some additional information are given in the appendices.

---

<sup>2</sup>According to [5]: only fixed-target results are shown which were performed on  $H_2$  and  $D_2$  targets and which have been corrected for contributions from proton dissociative processes.

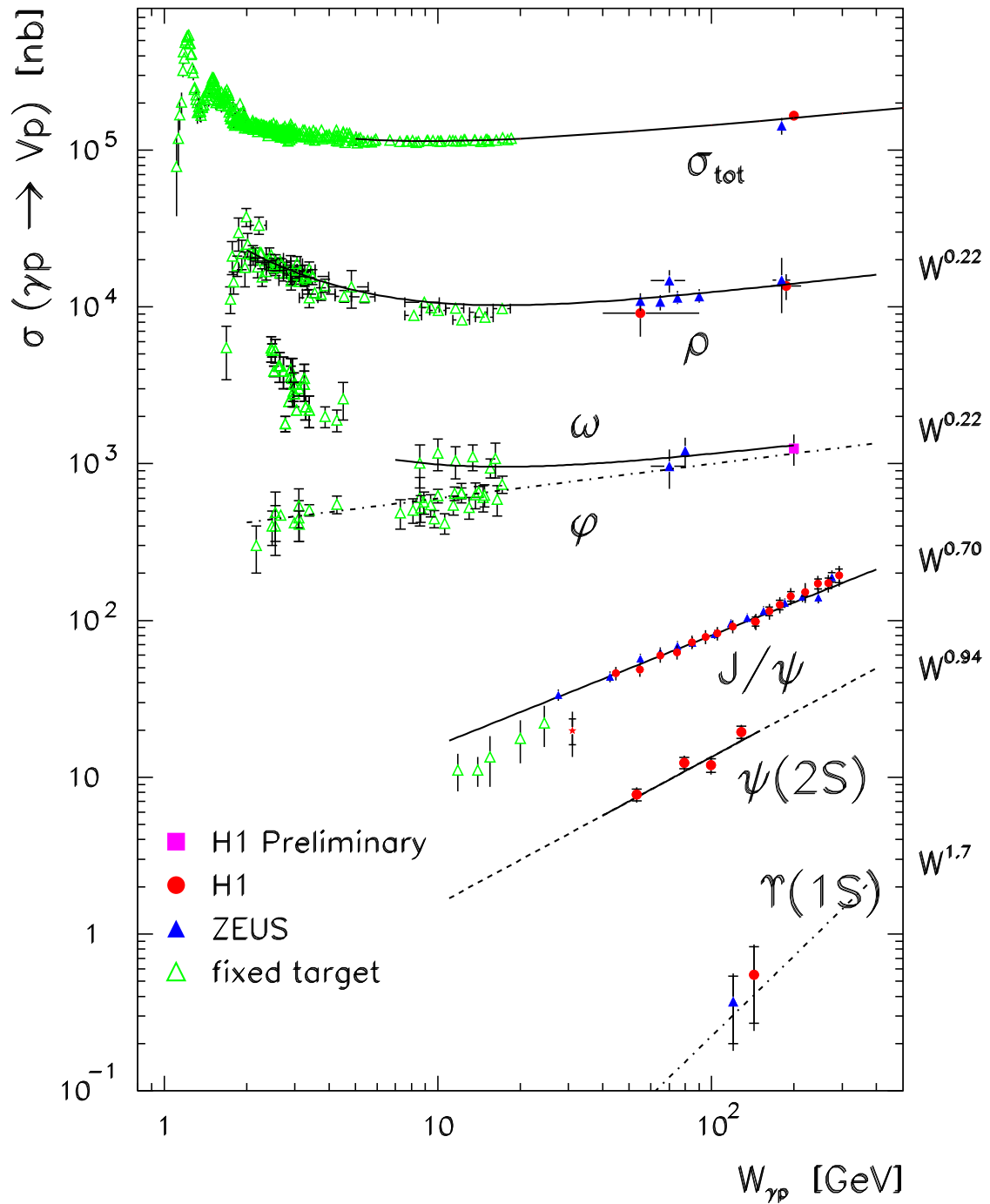


Figure 1.1: Overview of the dependence of the elastic cross section of several vector meson production and of the total photon proton cross section on the center of mass energy in the photon proton rest frame  $W_{\gamma p}$  in the photoproduction region. The figure is taken from [1]. The green triangles originate from fix-target experiments; for  $J/\psi$  they are extracted from [2, 3]<sup>2</sup>. The red circles represent the H1 measurements; for  $J/\psi$  they are extracted from [4] and the red star measurement point is coming from [5]. The blue triangles represent the Zeus measurement; for  $J/\psi$  they are extracted from [6].



# Chapter 2

## Theory

### 2.1 Kinematic Variables of Electron Proton Scattering

An electron proton ( $ep$ ) scattering process ( $ep \rightarrow eX$  or  $\nu_e X$ ) is in leading order described by exchanging a photon ( $\gamma$ ),  $Z^0$ - or  $W^\pm$ -boson. An exchange of a photon or  $Z^0$ -boson is called a neutral current (NC) process, whereas by a charged current (CC) process a  $W^\pm$  boson is exchanged. But CC processes are highly suppressed at low  $Q^2$  [7], therefore only NC are left in the region where the analysis is done. Additionally the contribution from  $\gamma$ -exchange to the NC cross section dominates the  $Z^0$ -process, because of the large  $Z^0$ -mass, thus in the following only electromagnetic interaction is considered in the electron vertex.

A generic  $ep$  scattering event is shown in figure 2.1 . The incoming electron<sup>1</sup> with momentum  $k$  exchanges a virtual photon with momentum  $q$  and leaves with a momentum of  $k'$ .  $P$  represents the momentum of the incoming proton,  $P'_X$  the momenta of the outgoing particles produced by the bursting proton. Since these 4 momenta are not Lorentzian invariant, the following variables are used to describe the scattering processes:

- The photon virtuality  $Q^2 \equiv -q^2 = -(k - k')^2$ .
- The squared centre of mass energy in the lab system  $s \equiv (k + P)^2 \simeq 4E_e E_p$  by neglecting the masses of the proton and electron.
- The squared centre of mass energy in the proton photon rest frame  $W_{\gamma p}^2 \equiv (P + q)^2 \simeq ys - Q^2$  by neglecting the masses.  $y$  means the inelasticity and is defined as  $y \equiv \frac{P \cdot q}{P \cdot k}$ .
- The squared moment transfer at the proton vertex  $t \equiv (P - \sum_X P'_X)^2$ .

In the limit  $Q^2 \rightarrow 0 \text{ GeV}^2$  the photon becomes real, that is the reason why  $Q^2$  is called virtuality. This is similar to the process where a real photon would scatter with the proton, therefore this process is called *photoproduction*. In the opposite, if  $Q^2 \gg 0 \text{ GeV}^2$ , this type of interaction is named *electroproduction* or *deep inelastic scattering* (DIS). Since  $Q^2$  is proportional to  $1 - \cos \Theta_e$ , with  $\Theta_e$  the angle between the incoming and *scattered electron* (outgoing electron in figure 2.1), the direction of the scattered electron trajectory is going to the central region of the detector with increasing  $Q^2$ .

---

<sup>1</sup>At HERA both electrons and positrons were used.

<sup>2</sup> $Q^2$ ,  $y$  and the Bjorken  $x = \frac{Q^2}{2P \cdot k}$  are related according the formula  $Q^2 = xys$ .

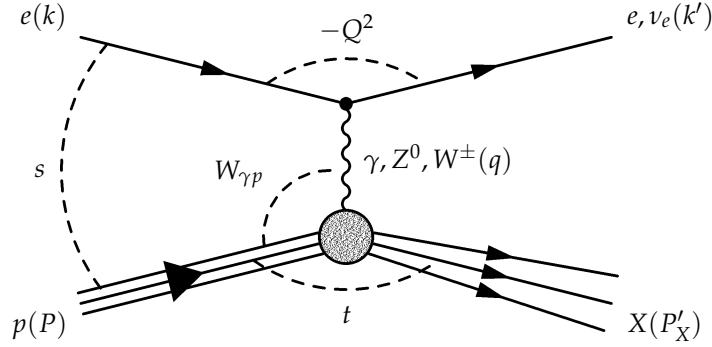


Figure 2.1: Generic Feynman diagram for  $ep$  scattering. The 4-momentum vectors of the particles are put in parentheses.

Experimentally a cut has to be applied, to distinguish the regions from each other. In this thesis events with  $Q^2 < 1 \text{ GeV}^2$  are called photoproduction events.

## 2.2 Characterisation of $J/\psi$ Production

The classification of events producing a  $J/\psi$  can be done from different viewpoints. In this thesis the experimental side is used, instead of a theoretical argumentation. Experimentally two processes are visible in the detector. First the *inelastic*  $J/\psi$  production  $\gamma p \rightarrow J/\psi X$  (see figure 2.2 (a)<sup>3</sup> and (b)), where  $X$  represents all other particles produced by the interaction. Second the *elastic*  $J/\psi$  production  $\gamma p \rightarrow J/\psi p$ , where the proton stays intact (see figure 2.2(c)).

For elastic (and partially also for inelastic)  $J/\psi$  production the proton and photon exchange a vacuum quantum number object. The behaviour of this intermediate state is specified in the theory used to describe the scattering process. In Regge theory this object is a pomeron ( $\mathcal{P}$ ), in leading order QCD a double gluon ( $gg$ ) and in higher orders of QCD a gluon ladder.

In theory often a slightly different process classification is done. A process is called *diffractive*<sup>4</sup> if a vacuum quantum number object is exchanged. This process can in leading order be illustrated by figure 2.2(b). Unfortunately the definition of a diffractive process is not unique, sometimes additional or even other criteria are used. For some examples see [9]. Therefore and because of the detector response, the proton is splitting up or not, in this thesis the above classification, which separates events only in the classes of elastic and

<sup>3</sup>The additional gluon has to be there because of colour and parity conservation and the fact that a  $J/\psi$  is colourless. Without such a gluon no colour singlet  $J/\psi$  could be produced. But a non colour singlet state of a  $c$  and  $\bar{c}$ , whereas they are hadronizing separately, is still possible, it is called *open charm production*. Theoretically possible is also a  $J/\psi$  formed by a colour octet  $c\bar{c}$  pair, in this case the additional gluon ( $g$ ) would not be needed. But this process is dominated by the colour singlet production [8].

<sup>4</sup>The term *diffraction*, as it is used in optical wave theory, is not out of place. Indeed for hadron hadron interaction the same behaviour as for optical waves was shown to be valid (see [9] and more detailed [10]).

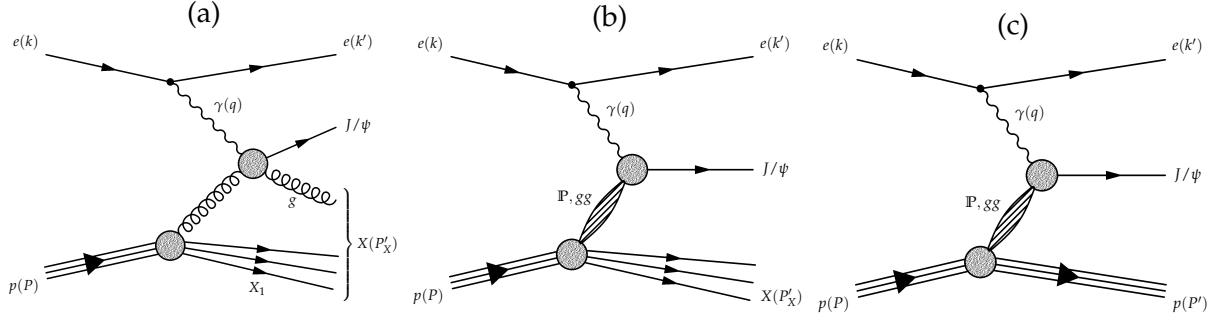


Figure 2.2: Generic leading order Feynman diagrams for inelastic (a) and (b), and for elastic (c)  $J/\psi$  production.

inelastic events, is used.

## 2.3 Models for Vector Meson Production

Due to perturbation theory one can describe the photon as superposition of a bare photon state  $|\gamma_B\rangle$  and of a  $q\bar{q}$  state, created by fluctuation of the photon. If the virtuality is small then the fluctuation is long lived and one can look at it as a vector meson. Therefore a photon can be written as

$$|\gamma\rangle = \sqrt{Z_3}|\gamma_B\rangle + c\sqrt{\alpha}|h\rangle,$$

where  $|h\rangle$  is a hadronic state [11] and must have the same quantum numbers as the photon ( $J^{CP} = 1^{--}$ ).  $Z_3 = 1 - c^2\alpha$  is needed to get the proper normalisation and  $\alpha$  means the electromagnetic coupling constant. It was shown that, if the target particle is a hadron for example a proton, then the hadronic state of the photon will dominate the process and the interaction is similar to proton proton interaction [9].

In the non-perturbative VDM (Vector Dominance Model) model<sup>5</sup> one assumes that only the hadronic part interacts with a hadronic target and that the hadronic state of the photon is a superposition only of vector mesons. Since in this thesis only  $J/\psi$  are considered, one can set  $c\sqrt{\alpha}|h\rangle = \frac{e}{f_{J/\psi}}|V_{J/\psi}\rangle$ . With  $e$  the electric charge and  $f_{J/\psi}$  a constant.

Therefore in this model the  $\gamma p$  interaction is similar to hadron-hadron interaction. By increasing  $Q^2$  (or  $t$ , or  $p_t$ ) the virtuality will increase too and thus one expects that the description of  $\gamma p$  scattering will fail in the high  $Q^2$  (and  $t, p_t$ ) region [11]. But on the other side the description by perturbation quantum chromodynamics (pQCD) should be appropriate. Therefore both models supplement each other in these two separated regions.

<sup>5</sup>Actually the VDM model only considered the vector mesons  $\rho^0$ ,  $\omega$ ,  $\phi$  since those were the only one known at that time. If the heavier vector mesons  $J/\psi$  and  $\Upsilon$  are taken into consideration as well, one speaks of the generalised vector dominance model (gVDM or GDM). For simplicity in this thesis it will be referred as VDM.

## 2.4 Regge Theory

Regge theory is a very successful theory to describe hadron hadron scattering  $A + B \rightarrow C + D$ . It connects the spin  $J$  and the square mass  $m^2$  for particles with the same “internal” quantum numbers, such as isospin, strangeness, baryon number and so forth. As described in the last section according to the VDM  $\gamma p$  interaction is similar to hadron-hadron interaction, therefore it is also possible to use Regge theory for  $ep$  scattering in low  $Q^2$  domain.

The first hadron hadron interactions studied, like  $\pi p \rightarrow \rho p$  processes, could well be described by the exchange of a pion. But for other processes, like  $\pi p \rightarrow \pi p$ , the exchange of a pion is not allowed, because of G-parity violation. Using a  $\rho$  instead of a  $\pi$  is possible and showed a good agreement with the data [7]. Therefore it was proposed the exchange of a so called reggeon, which is equivalent to the exchange of particles with different spins (see figure 2.3).<sup>6</sup>

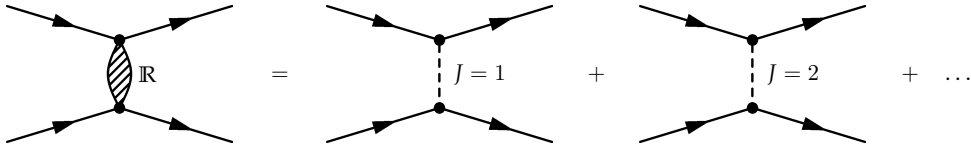


Figure 2.3: A reggeon exchange can be seen as the exchange of many particles with different spins  $J$ .

The Regge theory assumes that there exist bound states with angular momentum  $J_B$ , mass  $M_B$  and resonances with  $J_R$  and  $M_R$ . The bound states create a pole at  $t = t_B \equiv M_B^2$ , the resonances at  $t = t_R \equiv M_R^2 - iM_R\Gamma$  of the partial wave amplitude  $f_j(t)$  for  $j = J_B$  and  $j = J_R$ , respectively. Now it is possible to interpolate  $f_j(t)$  between the integer values  $j$  to get  $f(j, t)$ , where  $l$  can be complex, and demand that  $f(j, t) = f_j(t)$ . Then it is possible to interpret the sequence of the poles as a single moving Regge pole with  $l = \alpha(t)$  [7]. The function  $\alpha(t)$  is called Regge trajectory with  $\alpha(t_i) = J_i$ . One can then write the connection between them as

$$J = \text{Re}(t_j).$$

As an example in figure 2.4(a) the trajectory for  $\rho$  is given and in 2.4(b) the so called

<sup>6</sup>A general reason why single particle exchange cannot describe two-body scattering in the high energy region is the fact, that the transition amplitude

$$T(s, t) \xrightarrow{s \rightarrow \infty} s^J,$$

where  $s$  and  $t$  are the Mandelstam variables ( $s = (p_A + p_B)^2 = (p_C + p_D)^2$  and  $t = (p_A - p_C)^2 = (p_B - p_D)^2$ ), violates the (Martin-)Froissart bound for  $J > 1$  and therefore unitarity [9]. The (Martin-)Froissart theorem says, that the total cross section in the high energy region has to be limited by

$$\sigma \leq c \ln^2 s \quad \text{for } s \rightarrow \infty,$$

where  $c$  is a constant.

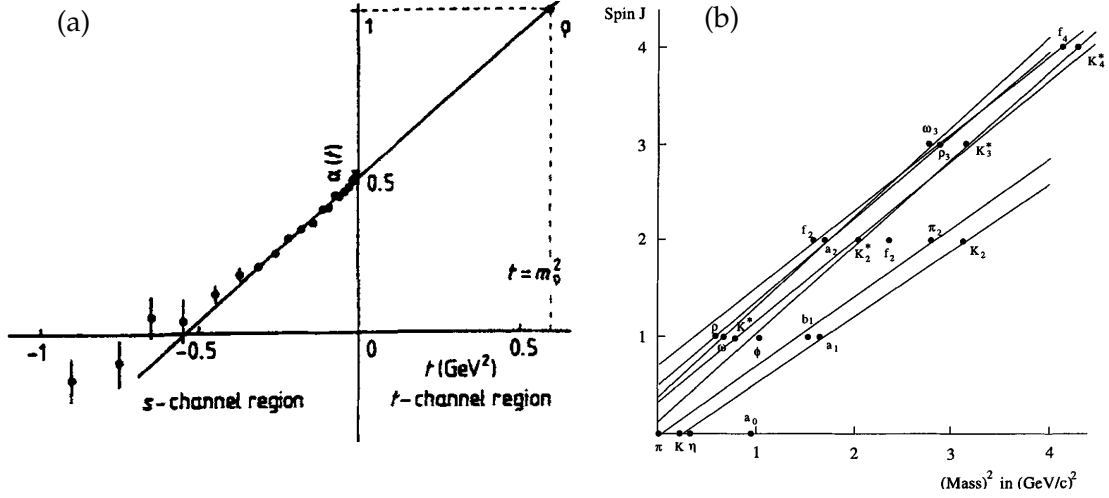


Figure 2.4: (a) The  $\rho$  trajectory extracted from the reaction  $\pi^- p \rightarrow \pi^0 n$  [7]. (b) Chew-Frautschi plot shows different Regge trajectories in the  $J$ - $M^2$  plane.

Chew-Frautschi plots, which shows different trajectories. It is remarkable that the Regge trajectories are linear. Therefore it is possible to express  $\alpha$  by

$$\alpha(t) = \alpha_0 + \alpha' t.$$

With the use of the Regge trajectory it is possible to write the transition amplitude for the two-body scattering as

$$T_s(s, t) \propto s^{\alpha(t)}$$

and if the full calculation is taken in to account one can derive [7]

$$\frac{d\sigma}{dt} = \frac{\gamma(t)}{s_0^2} \left(\frac{s}{s_0}\right)^{2(\alpha_0-1)} e^{2\alpha' t \ln \frac{s}{s_0}}, \quad (2.1)$$

where  $s_0$  is just an arbitrary scaling factor and  $\gamma(t)$  is related to the residue of  $f(j, t)$ .

In the time of creation of the Regge theory the energies used for scattering experiments were small compared to the cm energy used at HERA. Fits for different trajectories gave  $\alpha_0 \sim 0.5$  and  $\alpha' \sim 1 \text{ GeV}^{-2}$ . Therefore it was expected that the total cross section, given by  $\sigma_{\text{tot}} \sim s^{\alpha_0-1}$ , would decrease with higher energy. But this was not the case. So a new object called pomeron ( $\mathbb{P}$ ) with vacuum quantum numbers and a trajectory  $\alpha_{\mathbb{P}}(t) = \alpha_{\mathbb{P}}(0) + \alpha'_{\mathbb{P}} t$  was introduced with  $\alpha_{\mathbb{P}}(0) > 1$  in order to describe the data.

If a fit is done of the total  $\gamma p$  cross section one finds the trajectory  $\alpha_{\mathbb{P}}(t) = 1.0808 + 0.25t$ , which was predicted by Donnachie and Landshoff before the start of HERA [9]<sup>7</sup>.

<sup>7</sup>To extend the fit range also a reggeon exchange beside a pomeron could take into account. The cross section can then be parameterised by  $\sigma_{\text{tot}} = XW^{\alpha_{\mathbb{P}}(0)-1} + YW^{\alpha_{\mathbb{R}}(0)-1}$ . This leads to fit parameters  $X = 0.0677$ ,

## 2.5 Reconstruction of the Kinematic Variables

In  $ep$  scattering processes the usual scattering variables  $(y, Q^2, x)$  can be determined by 5 different standard methods using experimentally accessible observables. This step is normally called reconstruction. (An overview and a comparison of the different methods can be found in [12]).

In this thesis the electron method is used to calculate  $Q^2$  by

$$Q_e^2 = 4E_e E'_e \cos^2 \frac{\Theta'_e}{2}, \quad (2.2)$$

where  $E_e$  and  $E'_e$  means the energy of the incoming and scattered electron and  $\Theta'_e$  the angle of the scattered electron with respect to the proton direction. To calculate  $y$  a modified Jacquet Blondel method is used, where

$$y_{mh} = \frac{(E - p_z)_\psi}{2E_e}. \quad (2.3)$$

$(E - p_z)_\psi$  means the energy minus the  $z$  component of the  $J/\psi$  momentum. The momentum difference of the incoming and outgoing proton  $t$  is reconstructed by

$$t \simeq -p_{\psi,t}^2, \quad (2.4)$$

where  $p_{\psi,t}$  is the transverse momentum component of the  $J/\psi$ . This formula is valid for small  $|t|$  and for small  $Q^2$ . It is assumed that the masses are negligible compared to the energies ( $m_e, m'_e \ll E_e, E'_e$  and  $m_p, m'_p \ll E_p, E'_p$ ). As can be seen in equation 2.4, normally is  $t < 0$ , therefore most of the time not  $t$  but  $|t|$  will be used, to get positive values.

## 2.6 Cross Section and Photon Flux

The inelastic differential  $ep$  cross section in DIS can be written (in leading order, Born cross section) as

$$\frac{d^2\sigma_{ep}}{dydQ^2} = \frac{4\pi\alpha^2}{Q^4x} [y^2xF_1 + (1-y)F_2],$$

whereas the  $F_i \equiv F_i(y, Q^2)$  for  $i \in 1, 2$  mean the proton structure functions and  $\alpha$  represents the electromagnetic coupling constant. The parity violating structure function  $F_3$  is negligible in the region  $Q^2 \ll m_{Z^0}^2$  [13]. If the longitudinal structure function  $F_L(y, Q^2) = F_2 - 2xF_1$  is introduced, one gets for the cross section by eliminating  $F_1$  in favour of  $F_L$

$$\frac{d^2\sigma_{ep}}{dydQ^2} = \frac{4\pi\alpha^2}{Q^4x} [(1-y+0.5y)F_2 - 0.5y^2F_L].$$

---

$Y = 0.129$ ,  $\alpha_{\mathbb{R}} = 1.0808$  and  $\alpha_{\mathbb{R}}(0) = 0.5475$  for the total  $\gamma p$  cross section.

For historical reasons and for the fact that the theoretical predictions normally are given for the  $\gamma p$  cross section, the  $ep$  cross section will be transformed. Following the standard approach and using the Weizsäcker-Williams approximation [14, 15, 16] at low  $Q^2$  in which the incoming electron is seen as a “bunch of photons”, one may write the  $ep$  cross section in a general form as

$$\frac{d^2\sigma_{ep}}{dydQ^2} = \mathcal{F}_\gamma^T(y, Q^2)\sigma_{\gamma p}^T + \mathcal{F}_\gamma^L(y, Q^2)\sigma_{\gamma p}^L,$$

where  $\mathcal{F}_\gamma^T(y, Q^2)$  and  $\mathcal{F}_\gamma^L(y, Q^2)$  represent the transverse and the longitudinal photon flux and  $\sigma_{\gamma p}^T$  and  $\sigma_{\gamma p}^L$  the transverse and longitudinal  $\gamma p$  cross sections with  $\sigma_{\gamma p} = \sigma_{\gamma p}^T + \sigma_{\gamma p}^L$ . In this approximation one gets

$$\mathcal{F}_\gamma^T(y, Q^2) = \frac{\alpha}{\pi y Q^2} (1 - y + 0.5y^2)$$

$$\varepsilon(y) = \frac{\mathcal{F}_\gamma^L(y, Q^2)}{\mathcal{F}_\gamma^T(y, Q^2)} = \frac{1 - y}{1 - y + 0.5y^2}.$$

Thus the  $\gamma p$  cross section is

$$\frac{d^2\sigma_{ep}}{dydQ^2} \simeq \mathcal{F}_\gamma^T(y, Q^2)\sigma_{\gamma p}^T [1 + R\varepsilon],$$

with  $R = \frac{\sigma_{\gamma p}^L}{\sigma_{\gamma p}^T}$ .

It is used that  $\varepsilon \sim 1$ , which means that all photons are transverse<sup>8</sup>. Therefore the cross section is

$$\frac{d^2\sigma_{ep}}{dydQ^2} \simeq \mathcal{F}_\gamma^T(y, Q^2)\sigma_{\gamma p}.$$

Finally the total  $\gamma p$  cross section in the visible kinematical region is given by integrating over  $y$  and  $Q^2$

$$\sigma_{\gamma p}(\langle y \rangle, \langle Q^2 \rangle) \simeq \frac{\sigma_{ep}}{\Phi_\gamma^T}$$

---

<sup>8</sup>This approximation is reasonable, because the kinematical region is restricted to  $W_{\gamma p} \leq 110$  GeV, due to the event selection (see chapter 6). This means with  $Q^2 < 1$  GeV<sup>2</sup> and  $W_{\gamma p} = \sqrt{ys - Q^2}$  that  $y \lesssim 0.25$  and thus  $\varepsilon \gtrsim 0.96$ . In [4] p. 34  $R$  is measured and it follows that for  $Q^2 < 1$  GeV<sup>2</sup> that  $R \lesssim 0.1$ . Therefore  $A$  in

$$\frac{d^2\sigma_{ep}}{dydQ^2} \simeq \mathcal{F}_\gamma^T(y, Q^2)\sigma_{\gamma p} \underbrace{\frac{1 + R\varepsilon}{1 + R}}_A,$$

is  $A \gtrsim 0.996$ . Thus by using  $A = 1$ , which is equal to  $\varepsilon = 1$ , the introduced systematic uncertainty by this approximation is expected to be small compared to the total systematic uncertainty.

where  $\Phi_\gamma^T$  means the integrated photon flux

$$\Phi_\gamma^T = \int_{y_{min}}^{y_{max}} dy \int_{Q_{min}^2}^{Q_{max}^2} dQ^2 \mathcal{F}_\gamma^T. \quad (2.5)$$

The integration range of  $y$  is directly linked to the  $W_{\gamma p}$  range (see above) which is determined by the phase space of the analysis. The upper  $Q^2$  boundary for photoproduction can be chosen experimentally and is set to  $Q_{max}^2 = 1 \text{ GeV}^2$ , but the lower one is given by  $Q_{min}^2 = \frac{y^2}{1-y} m_e^2$  (see appendix B), which is valid for large electron momentums compared to electron mass. The values of the integrated photon flux are given in appendix E.

# Chapter 3

## The H1 Detector at HERA

This chapter gives a very brief overview of the HERA accelerator and the H1 detector. The parts relevant for this analysis of the detector are described in more details others are omitted. For a nearly full description of the H1 detector see [17, 18, 19].

### 3.1 The HERA Accelerator

The HERA (Hadron Elektron Ring Anlage) accelerator – the only  $ep$ -collider ever built – was located at DESY (Deutsches Elektron Synchrotron). The operation period is divided in two main phases, called HERA I and HERA II, and ended in 2007. Between these two periods a luminosity upgrade was installed. The integrated luminosity of HERA I and II are shown in figure 3.1. Since during that time no collisions took place, it was also used to make some modifications at the detectors, for example the Fast Track Trigger for H1 was installed. In this thesis only run periods from HERA II are considered, therefore the term HERA will mean HERA II, if nothing else is noted.

The main ring of HERA had a circumference of about 6.3 km and contains the two separated beam pipes for the acceleration of the leptons<sup>1</sup> and protons. The energy of the leptons was 27.6 GeV. At HERA II the protons were nominally accelerated to 920 GeV<sup>2</sup>. At the end of HERA II operation, after a short break for modifications of about two weeks, collisions with proton energies of 460 GeV and 575 GeV were performed. The main reason was to directly measure the longitudinal structure function of the proton  $F_L$  [20].

The particle bunches were separated by a time interval of about 96 ns, which correspond to a frequency of 10.4 MHz. The beams were colliding at two points where the experiments H1 and ZEUS were located. At the other two straight parts of HERA the fix-target experiments HERMES and HERA-B were stationed.

A schematic overview of HERA and its pre-accelerators is shown in figure 3.2.

---

<sup>1</sup>Since electrons and positrons were used as particles for accelerating they will be referred as leptons.

<sup>2</sup>For HERA I it was 820 GeV

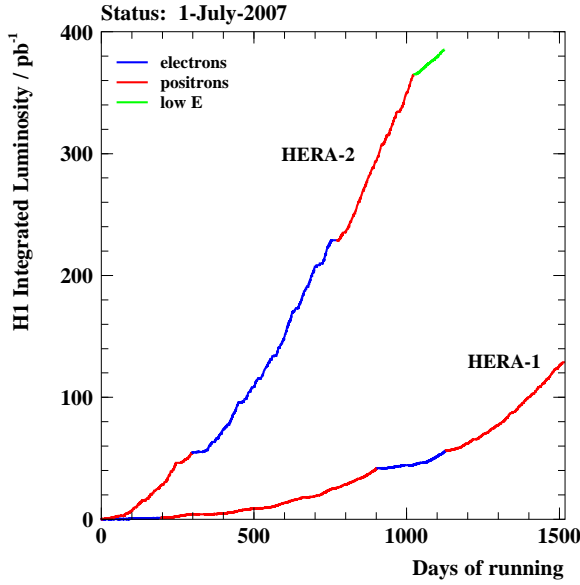


Figure 3.1: Integrated luminosity for HERA I and II.

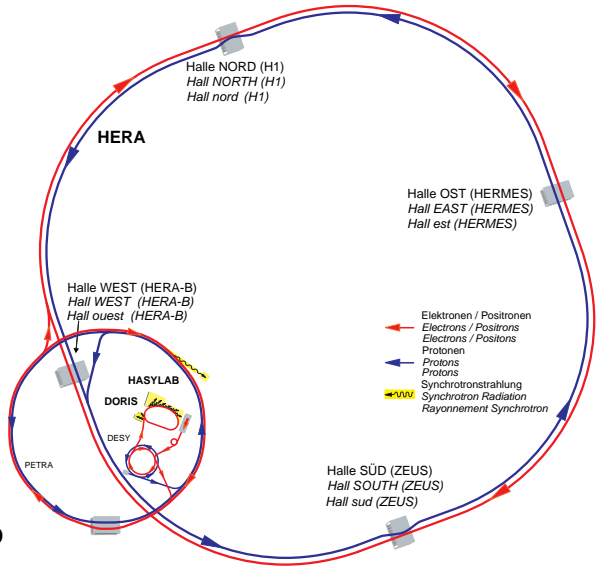


Figure 3.2: A schematic overview of HERA and its pre-accelerators.

### 3.2 The H1 Detector

The H1 detector was located in the North hall of the HERA ring and was built by a collaboration of about 400 physicists from over 40 countries. Due to the different momenta of the colliding protons and leptons the detector was built asymmetrically along the  $z$ -axis<sup>3</sup>. This means that the components in the forward and backward direction are not identical. For an overview of most<sup>4</sup> parts of the H1 detector see figure 3.3.

The detector was consisted of different subsystems. The first and most closely placed to the beam pipe was the tracking system, its sub-detectors were constructed to measure as precise as possible the trajectory of the charged particles produced by the collision. The applied magnetic field produced a bent trajectory which allowed to extract the momentum. The tracking system was surrounded by the calorimetry detectors. In the forward and central direction a liquid argon detector was placed, which primary assignment was to measured the energy of the particles. The electromagnetic part used lead, the hadronic steel as absorber plates. In the backward region a spaghetti calorimeter was used mainly to detect the scattered electron, which is essential to identify DIS processes. They all were enclosed by a superconducting magnet, which produced a field of 1.16 T. The next layer contained the muon detector and the iron return yoke, both used to return the streamlines

<sup>3</sup>The origin of the H1 coordinate system is situated in the nominal interaction point. The  $z$ -axis is oriented along the direction of the incoming proton. The positive  $z$ -direction is called forward, the negative backward direction. The  $x$ -axis points to the centre of the HERA ring, and thus the  $y$ -axis directs upwards. To express the direction of particles normally  $\Theta$  (angle between the trajectory of the particle and the positive  $z$ -axis) and  $\phi$  (angle between the  $x$ -axis and the projection of the trajectory into the  $xy$ -plane) are used.

<sup>4</sup>In this analysis the Forward Tagging System (FTS) was used too, but since the nearest FTS detector component was located 26 m from the interaction point they are not visible in figure 3.3.

of the magnetic field.

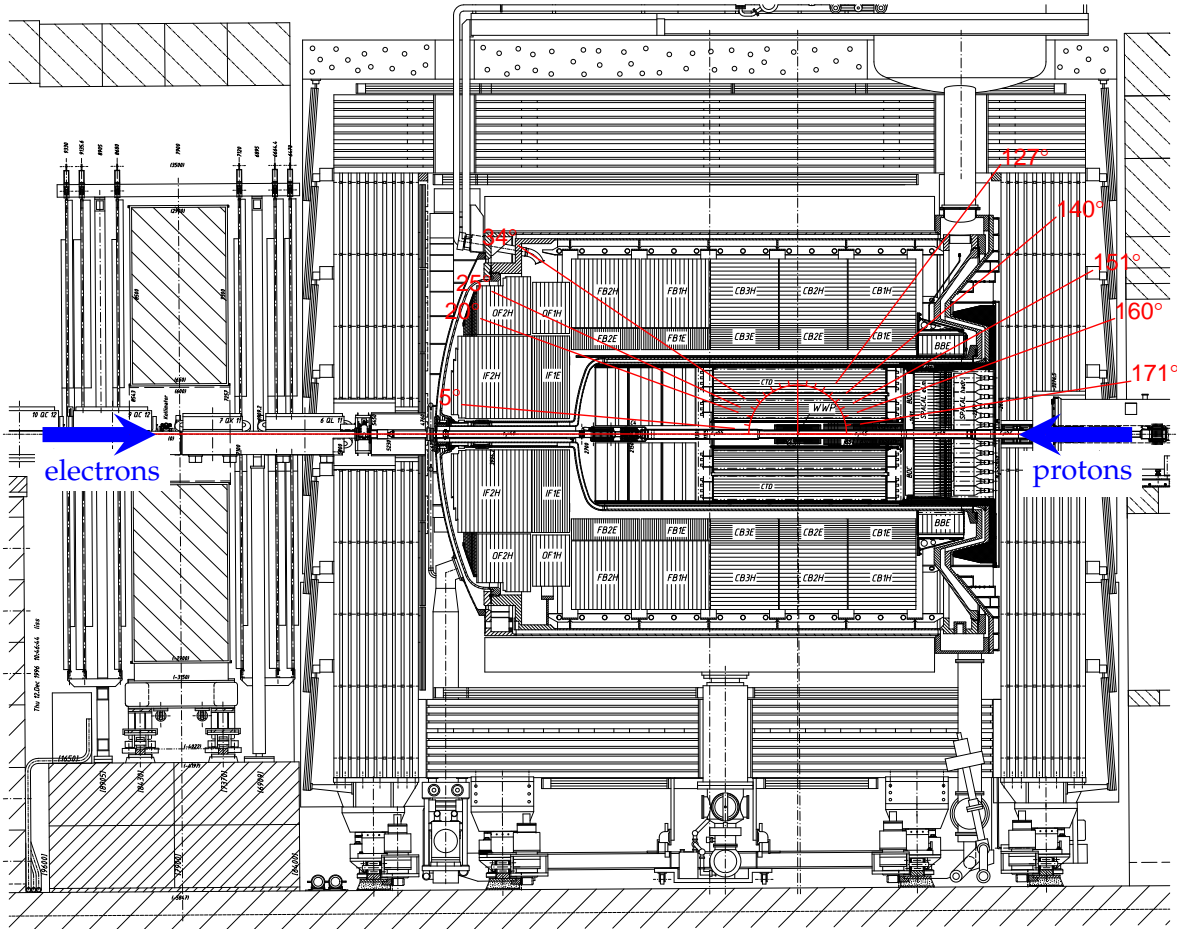


Figure 3.3: A schematic view of the H1 detector.

### 3.2.1 Tracking

The tracking system in the H1 detector consists of three detector groups Forward Tracking Detectors (FTD), Central Tracking Detectors (CTD) and Backward Tracking Detectors (BTD). In this thesis mainly the CTD are used. For an overview of the tracking systems see [17, 18].

The innermost detector in the central region is the Central Silicon Tracker (CST) with an angular coverage of  $30^\circ < \Theta < 150^\circ$  and consists of two layers of double-sided silicon detectors. The CST is enclosed by the Central Inner Proportional Chamber (CIP) which is a multiwire proportional chamber. The main tracking detector of H1 is the Central Jet Chamber (CJC) which is split in two concentric parts CJC1 and CJC2. The CJC1 contains 30, the CJC2 60 azimuthal cells with an angular coverage of  $20^\circ < \Theta < 160^\circ$  (see figure 3.4). Between them the Central Outer z-Drift Chamber (CIZ) and the Central Outer Proportional Chamber (COP) are situated.

In the forward direction the Forward Muon Detector (FMD) ( $3^\circ < \Theta < 17^\circ$ ) is lo-

cated [21].

### 3.2.2 Calorimetry, Muon and Forward Tagger System

The energy of particles is measured by the calorimetry system. In H1 it consists of two main calorimeters. In the forward and central region a Liquid Argon (LAr) detector covers the angle  $4^\circ < \Theta < 153^\circ$ . The LAr consists of two parts, the inner one uses lead absorbers and detect electromagnetic showers whilst hadronic showers usually penetrate into the outer part which uses steel absorbers [17, 18].

In the backward direction a Spaghetti Calorimeter (SpaCal) with lead-scintillating fibres is mainly used to detect the scattered electron ( $153^\circ < \Theta < 177.5^\circ$ ) [22, 19].

In the forward direction at  $z = 4.9$  m the PLUG calorimeter is situated. It consists of a lead absorber followed by four layers of scintillators and has an angular coverage of  $1.2^\circ < \Theta < 3.2^\circ$ .

Far down the beam pipe at  $z = 26, 28, 53$  and  $92$  m the four stations of the Forward Tagger System (FTS) are located, each contains four scintillators arranged around the beam pipe.

## 3.3 H1 Trigger System

The bunch crossing at HERA has a frequency of 10.4 MHz, however the interesting processes were only produced with about 1 kHz. The remaining part is caused by background processes. Still the H1 readout frequency is much lower (50 Hz) and the maximal tape write speed, of about 20 MB/s, is even lower. Thus the events actually to stored on tape have to be selected as efficient as possible and the background has to be rejected. This is performed by the triggering system, which is hierarchically designed in 4 levels. This means, that only events passed the first level trigger (L1) will be considered in the second level (L2) and only events accepted by the L2 trigger are passed to the third one (L3). The same is true for the fourth level (L4) trigger.

The L1 trigger is designed to make a first classification, therefore it is important not to lose any event. It was built without any dead time and with only  $2.3 \mu\text{s}$  to return a decision. To make this possible the information from every bunch crossing within the  $2.3 \mu\text{s}$  – which correspond to about 23 bunch crossings – were hold in a pipeline. 256 trigger elements from different sub-detectors are combined in the central trigger logic to 128 sub-triggers, i.e for every sub trigger exist a collection of conditions. But the output frequency of some L1 sub-triggers may still be too high, because the L2 input is limited by about 1 kHz. Therefore every sub-trigger has also a so called *prescale factor*  $n$ , which means only every  $n^{\text{th}}$  event, that fulfils the sub-trigger conditions, is allowed to pass to the next level.

A sub-trigger is called *raw sub-trigger*, if an event satisfies all conditions. If it also passes

the prescale condition then it is called *actual sub-trigger*.

If at least one actual sub-trigger is given for an event then the “L1Keep” signal is sent and the event is transferred to L2. At this point the dead time begins because the storing of events in the pipeline is stopped.

The L2 level is composed of three parts all providing L2 trigger elements. The first one uses a neural network, the second one combines information from tracking, calorimetry and from the muon systems and is called *topological trigger*. And the third one, the *Fast Track Trigger (FTT)*, is based on the tracking information with a high spatial resolution comparable to the one available offline [9]. The L2 has 20  $\mu\text{s}$  available for calculation and if an L2 trigger condition is satisfied, the read out of the detector starts, otherwise everything is cleared and the pipeline from L1 is filled again.

The L3 level can handle an input rate of about 200 Hz and has an output frequency of circa 50 Hz. During 100  $\mu\text{s}$  it has time to confirm or reject the decision made in L1 and L2. In case of not accepting the event by L3 the detector readout is stopped and the data taking is restarted. L3 uses the FTT environment and was designed to look for specific decay channels (see below).

The fourth trigger level (L4) does not contribute anymore to the dead time. After the event is passed to L4, the L1 pipeline filling is restarted. Therefore L4 is working asynchronous to the HERA clock. This level is not handled by hardware as the previous ones, but by software running on a PC farm. Since the full reconstruction information is available, some additional reduction of the event frequency to a tape output of about 10 Hz is done by rejecting background and downscaling different event classes, which leads to L4 scaling factors called “L4Weights”. Events passing L4 are written on tape and are accessible for an offline analysis.

### 3.4 Fast Track Trigger (FTT)

By the upgrade to HERA II the luminosity was increased. Therefore it was necessary to build new triggers which are able to reject the growing amount of background events and select with high precision the interesting physics, especially in the region of low  $Q^2$  where no calorimeter trigger could be used [23]. The Fast Track Trigger (FTT) is able to reconstruct final states from tracks on trigger level, therefore it is an accurate instrument to look for heavy flavour physics, like elastic vector meson production or  $D^*$  decays (of interest is the decay into kaons and pions ( $D^* \rightarrow D^0\pi \rightarrow (K\pi)\pi$ ), the so called “golden channel”), especially in the photoproduction region of the phase space.

The FTT provides triggers on L1 to L3 level. On L1 and L2 level the FTT uses solely the

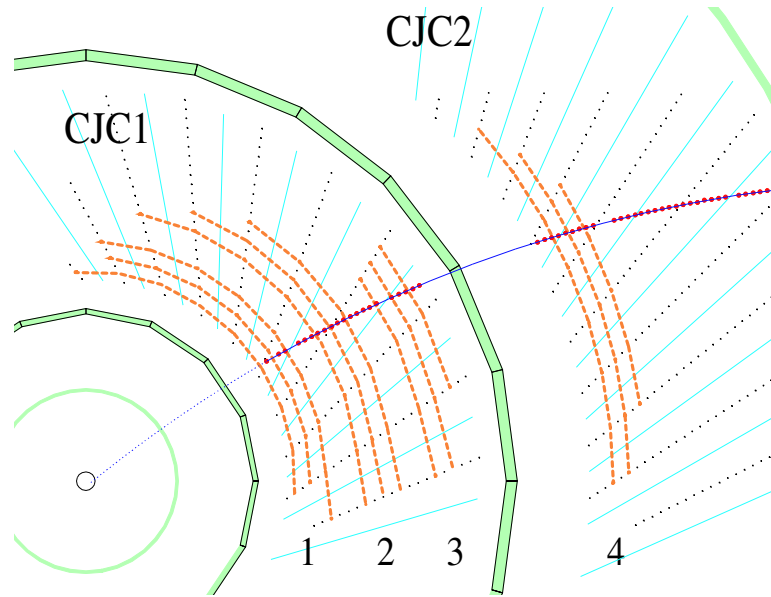


Figure 3.4: The four CJC layers used for the FTT are coloured orange. Every layer is composed of three sub layers. (Taken from [23])

information from the CJC to reconstruct the trajectory of particles. On L1 it uses four layers with three wires each (see fig. 3.4), to calculate the tracks in the  $r\phi$ -plane (only poor information about the z-axis is determined). Therefore cuts on the transverse momentum are precise, compared to earlier triggers. On L2 the granularity of the track reconstruction is improved, due to the time available for a decision. Also better z-resolution is achieved on this level. Therefore at this point precise information of  $p_t$  and z-vertex are usable to make a decision.

On L3 the information from the CJC and from other sub-detectors are combined. The L3 provides a partial event reconstruction including invariant mass and particle identification. Therefore it is possible to trigger on  $D^*$  or inelastic  $J/\psi$  events with large  $|t|$ . For more information see [9].

For the Monte Carlo Simulation (MC) (see chapter 4) the response of the FTT trigger has to be simulated. This is done by the FTT emulation software (*FTTEMU*), which is running after the *H1SimRec* program, whereas this package simulates the response of the remaining detector units.

# Chapter 4

## Monte Carlo Simulation

Monte Carlo (MC) simulations are widely used in particle physics for diverse reasons. The first is to compare theoretical models with measurements. The second is to determine fully inclusive quantities such as cross sections. This can be done e.g. by extrapolation of quantities measured in a limited visible region of the phase space to the full phase space. An other application of MC is the determination of acceptance and efficiencies.

Extrapolations used in the simulation can lead to wrong behaviour of a variable, therefore it is essential to make cross checks, to build up confidence in the simulation.

For this analysis MC simulation are used in three places. First, as mentioned above, to calculate the acceptance, second to calculate the trigger efficiencies and third for the separation of elastic and inelastic events. Although the use of MC at the first and last point is inevitable, it is not for the trigger efficiency, because it also can be determined from data. However the use of MC is reasonable because of statistical issues. (More details are given below.)

The program structure used for MC simulation in H1 is the following

- Generator: Events are generated randomly according to some theoretical distributions. Which distribution in what variable is used depends on the physical model in the event generator program. In this thesis the DiffVM generator is used. The output of the generator are events with specified 4-vectors.
- Simulation of the detector response: The passage of the generated events through the detector and the interaction with the material will be simulated. In H1 this is done by H1SIM.
- Event reconstruction: The response of the detector due to the interaction of the particles is calculated by the program H1REC, which is the same for generated as for real measured events. The programs H1SIM and H1REC are combined in one, called H1SIMREC.
- Trigger simulation: Whereas the order of the first three steps is common for particle physics event simulations, the FTT simulation (FTTEMU) and calculation based on the

information supplied by the FTT is done subsequently to above steps, due to historical reasons.

## 4.1 DiffVM generator

The DiffVM generator [24] simulates diffractive processes in the framework of Regge phenomenology and in the Vector Dominance Model.

In this model a virtual photon will be emitted by the incoming electron. In this thesis the photons are produced according to Weizsäcker-Williams Approximation [14, 15, 16]. The virtual photon fluctuates into a virtual vector meson (here a  $J/\psi$ ) and the vector meson interacts diffractively with the incoming proton by exchanging a pomeron.

There are many options which can be chosen, see [24].

In this thesis both elastic and inelastic MC are used. Normally they referred to as *elas* for elastic and *inelas* for inelas events.<sup>1</sup>

The cross section depends on  $t$  according to

$$\left(\frac{d\sigma}{dt}\right)_{elas} = \frac{d\sigma}{dt}\Big|_{t=0, W=W_0} e^{bt} \left(\frac{W}{W_0}\right)^{4\varepsilon} \quad (4.1)$$

for elastic events. It is a slightly modified version of equation 2.1<sup>2</sup>, which is predicted by the Regge Theory. For inelastic events, the distribution

$$\left(\frac{d\sigma}{dt}\right)_{inelas} = \frac{d\sigma}{dt}\Big|_{t=0, W=W_0} \left(1 - \frac{b}{n}t\right)^{-n} \left(\frac{W}{W_0}\right)^{4\varepsilon}$$

was taken. The variable  $1 + \varepsilon$  is the constant part in the pomeron trajectory  $a_p(t) \simeq \alpha_p(0) + \alpha'_p t = 1 + \varepsilon + \alpha'_p t$ .

## 4.2 Reweight MC

A MC simulation generates events according to a distribution which is given by a certain model believed to describe the underlying physics of the measurement. Often this model has some parameters which cannot be calculated by this theory and therefore have to be measured.

<sup>1</sup>The option in the generator steering file is named as “Choice of elastic or inelastic proton vertex”.

<sup>2</sup>Here the centre of mass energy in the  $\gamma p$  system  $W_{\gamma p}$  is the relevant energy scale, therefore  $s$  in equation. 2.1 has to be replaced by  $W_{\gamma p}$ .

The definition of the cross section is given in equation 9.1 and 9.2. To calculate it, several times (separation of elastic from inelastic events, acceptance, reconstruction, trigger efficiency and efficiency due to some additional cuts; see the corresponding chapters) the use of MC is needed. But these quantities itself are depending on the parameters used to generate the cross section. To solve this loop dependences an iterative procedure is used in this thesis.

Process	$b[\text{GeV}^{-2}]$	$n$	$W_0[\text{GeV}]$	$\varepsilon$	$\alpha'_p$
elastic	4.0	–	95	0.225	0.0
inelastic	1.5	2.0	95	0.225	0.0

Table 4.1: Parameter values for DiffVM generator for elastic and inelastic samples.

First two MC samples, one for elastic and one for inelastic, are generated for each energy region according to the parameters given in table 4.1. The cross section for data and MC are calculated, whereas MC is used for the missing quantities in the data cross section determination. Then they are divided. Because the efficiencies and the branching ratio are the same they are cancelling, thus the reweighting distributions for the differential cross sections are

$$R_{\text{elas}} = \frac{N_{\text{data}}^{\text{elas}}}{\mathcal{L}_{\text{data}}} \bigg/ \frac{N_{\text{diffvm}(\text{elas})}}{\mathcal{L}_{\text{diffvm}(\text{elas})}} \quad \text{and} \quad R_{\text{inelas}} = \frac{N_{\text{data}}^{\text{inelas}}}{\mathcal{L}_{\text{data}}} \bigg/ \frac{N_{\text{diffvm}(\text{inelas})}}{\mathcal{L}_{\text{diffvm}(\text{inelas})}}.$$

An example of the  $|t|$ -reweighting distributions  $R_{\text{elas}}$  for elastic and  $R_{\text{inelas}}$  for inelastic are given in figure 4.1(a) and (b). These reweighting distributions are fitted and the extracted reweight parameters are used to reweight the MC samples. The same is done for  $W_{\gamma p}$  in an additional step.

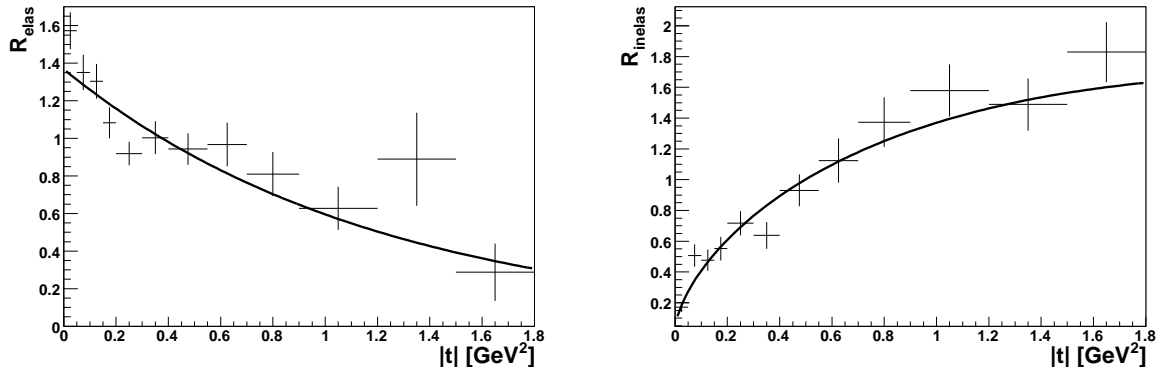


Figure 4.1: Example of the elastic (a) and inelastic (b) reweighting functions  $R_{\text{elas}}$  and  $R_{\text{inelas}}$  as function of  $|t|$  for the high energy period. The line represents the fit which is used to determine the reweight parameters.

An additional turn is not needed because the second reweighting functions are almost

flat.

The cross section in equation 4.1 shows that it depends, according to the model, on  $|t|$  and  $W_{\gamma p}$ . But in this thesis only one differential cross section are calculated and therefore the reweight procedure could only be done in  $|t|$  and  $W_{\gamma p}$  separately. Of course this introduce an error but the fits of the reweight distributions show that they still converge. That was expected because  $\varepsilon$  is estimated to be small [7].

### 4.3 Comparison of Monte Carlo with Data

To legitimate that the produced and reweighted MC can be used, in figure 4.2 and 4.3 the comparison between data and MC is shown in different variables (see caption of the figures) as an example for the low energy region. The green histograms represent the elastic MC, the blue the inelastic ones. The grey histograms are formed by stacking the two MC histograms. The red points are the data. The cuts used for this plots are given in table 6.2. Additional the cut  $2.9\text{ GeV} < m_{e^+e^-} < 3.15\text{ GeV}$  is used, to reduce background. (The definition of  $m_{e^+e^-}$  is given in equation 6.1).

As can be seen in the figures, there is still background in the data samples (difference between the grey histogram and the red points). This is due to the fact that no background MC was used. Never the less the shape of MC and data seems to agree and therefore the decision to use these reweighted MC is justified.

A possible way to subtract the background is the side band method described in [25, 26].

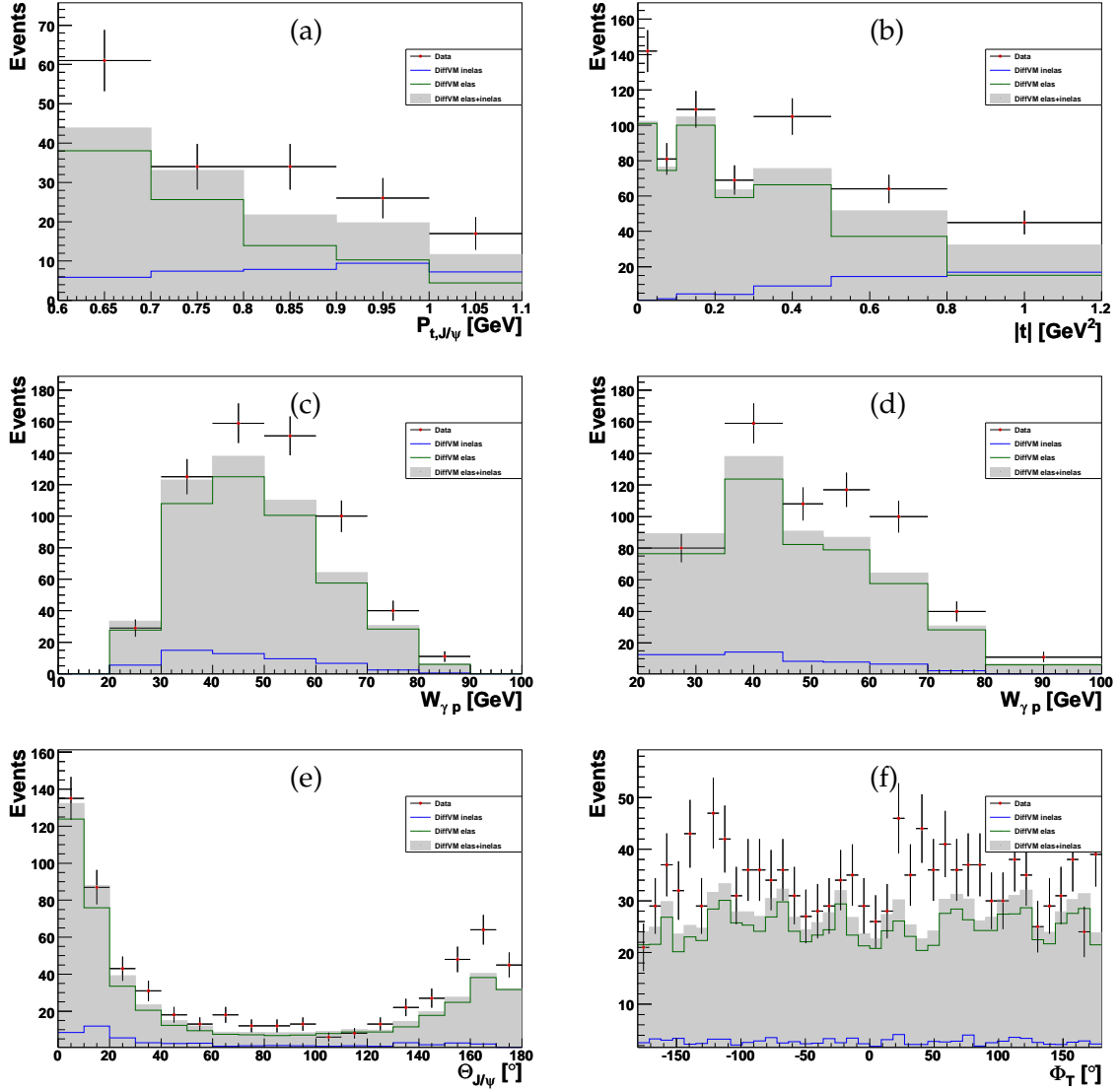


Figure 4.2: Comparison between Monte Carlo and data for the low energy period as functions of the transverse momentum of the  $J/\psi$ ,  $P_{t,J/\psi}$ , (a),  $|t|$  (b),  $W_{\gamma p}$  (c: equidistant binning, d: binning used in analysis), theta angle of the  $J/\psi$ ,  $\Theta_{J/\psi}$ , (e) and  $\phi$  angles of both tracks,  $\phi_T$ , (f). The green histogram represents the elastic, the blue the inelastic MC events; stacked they give the grey filled histogram. The red points are the data.

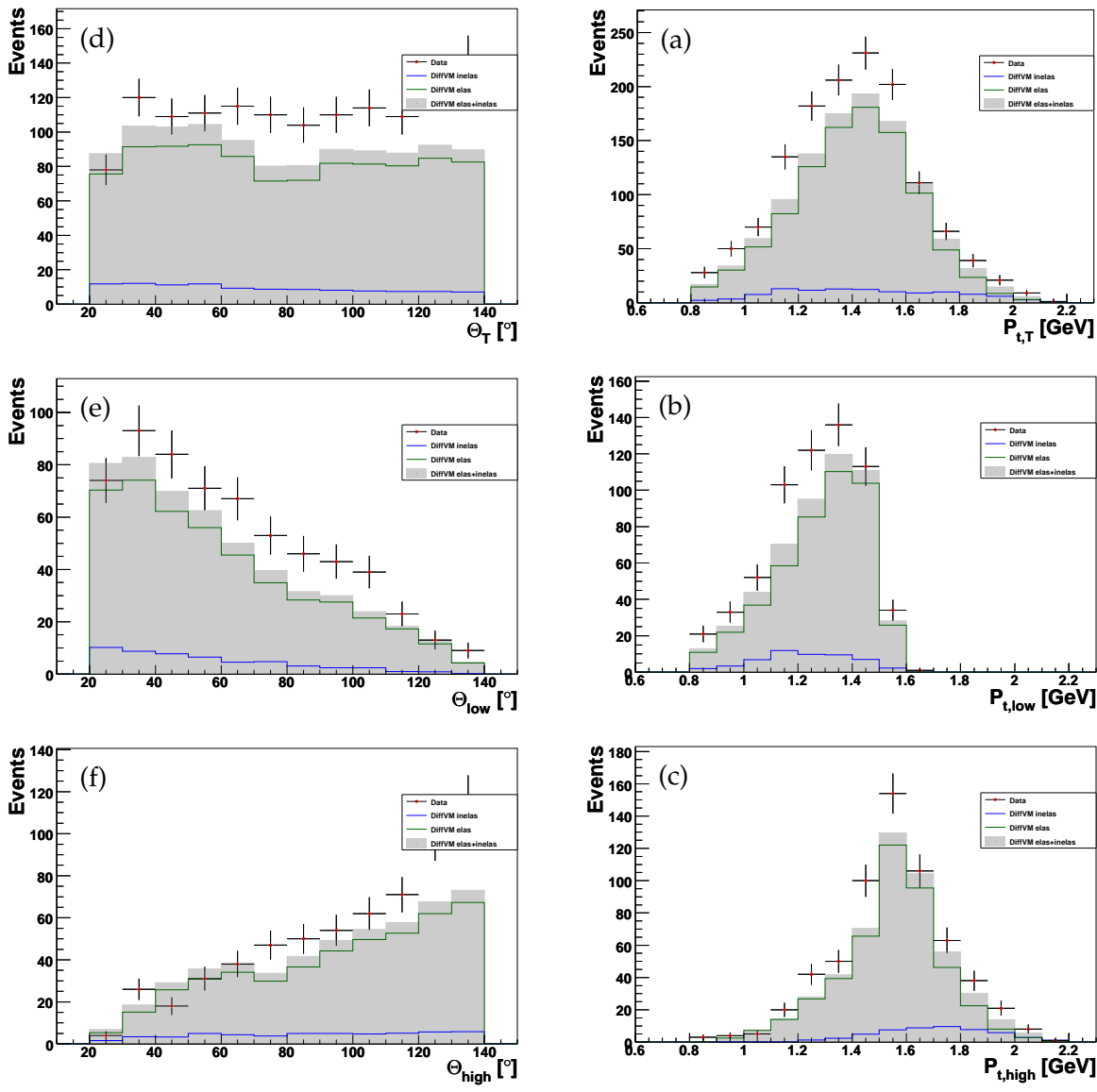


Figure 4.3: Comparison between Monte Carlo and data for the low energy period as functions of the transverse momentum of both tracks,  $P_{t,T}$ , (a), the transverse momentum of the smaller(larger)  $p_{t,}$   $P_{t,low}(P_{t,high})$ , (b,c), the theta angle of both tracks,  $\Theta_T$ , (d) and the theta angle of the smaller(larger)  $\Theta$ ,  $\Theta_{low}(\Theta_{high})$ , (e,f). The green histogram represents the elastic, the blue the inelastic MC events; stacked they give the grey filled histogram. The red points are the data.

# Chapter 5

## Data Selection and Trigger

First the data used for the  $J/\psi$  measurement are described, afterwards a short overview over the trigger conditions is given.

### 5.1 Data Selection

The data studied in this thesis were taken from the year 2007, which correspond to the run range from 492559 to 511024. The end is scheduled by the shut down of HERA. In this run period HERA was operating with positrons of 27.6 GeV energy. The protons were accelerated up to three different energies of 920 GeV, 575 GeV and 460 GeV, called high, medium and low energy period, respectively. The luminosity and the run ranges for the different energies are given in tables 5.1.

designation	proton energy [GeV]	run range	integrated luminosity [ $\text{pb}^{-1}$ ]	mean prescale factor for s59
high	920	492559 - 500611	45.5	1.05
medium	575	507842 - 511024	5.96	1.01
low	460	500918 - 507824	10.9	1.01

Table 5.1: Luminosity, run ranges and mean prescale factors for the three different energy periods.

In these ranges only runs with at least  $0.1 \text{ nb}^{-1}$  luminosity and medium or good quality are taken into account. Additionally a few run ranges are excluded, due to problems with some sub-detectors in that time. Furthermore only runs are selected, with a read-out of the detector components (CJC, CIP, LAr, PLUG, FMD, FTS, SpaCal<sup>1</sup>, TOF and LUMI), needed for this thesis, were on.

---

<sup>1</sup>The SpaCal detector is requested, because it is needed for the trigger efficiency study.

## 5.2 Trigger Conditions

To select elastically produced  $J/\psi$  events in the decay channel  $J/\psi \rightarrow e^+e^-$ , i.e. decay into two charged tracks, the sub-trigger *s59* is used. The L1 and L2 trigger conditions for *s59* are given in table 5.2. The CIP conditions are for background rejection, whereas the FTT conditions are fulfilled, if two opposite charged tracks, with transverse momentum above the threshold (given in the table), are measured in the CJC. No L3 conditions are used for the *s59* trigger.

trigger level	condition
L1	(CIP_sig > 1 && (CIP_mul < 6) && (FTT_mul_Ta < 5) && (FTT_mul_Td > 0) && veto conditions
L2	(FTT_mul_Te == 2) && (FTT_Qtot == 4)

Table 5.2: L1 and L2 trigger conditions for the *s59* subtrigger. (No L3 trigger conditions for *s59* exist.)

In the following the separate trigger conditions will briefly explained. More information about the CIP are given in [27] and for the FTT in [9].

- for L1
  - **CIP\_sig > 1**: This condition is used for background rejection. It requires, that the number of central tracks,  $N_{\text{ctr}}$ , is larger then the number of backward,  $N_{\text{bkw}}$ , and forward,  $N_{\text{fwd}}$ , tracks in the z-Vertex histogram of the CIP. It is coded in  $N_{\text{ctr}} > k(N_{\text{bwd}} + N_{\text{fwd}})$  with  $k = 1$  for CIP\_sig > 1 [28].
  - **CIP\_mul < 6**: Represents the demand to limit the maximal number of tracks to 30 and therefore rejects background mostly coming from non  $ep$ -interactions [9]. The formula for calculation is  $N_{\text{ctr}} + N_{\text{bkw}} + N_{\text{fwd}} < M$  for CIP\_mul < mul and with  $(\text{mul}|M) = \{(1|0), (2|2), (3|6), (4|10), (5|20), (6|30), (7|100), \dots\}$  [28].
  - **FTT\_mul\_Ta < 5**: The number of tracks with a transverse momentum above 100 MeV seen by the FTT is 4 or smaller.
  - **FTT\_mul\_Td > 0**: At least one FTT-track has a transverse momentum above 900 MeV.
- and for L2
  - **FTT\_mul\_Te == 2**: Calls for exactly two FTT-tracks with a transverse momentum larger than 800 MeV.
  - **FTT\_Qtot == 4**: Only events with the sum of charges of all FTT-tracks is equal to zero, are not rejected.

# Chapter 6

## Event Selection

To measure the differential elastic photoproduction cross section, the number of elastic  $J/\psi$  events within the kinematical region  $Q_e^2 < 1 \text{ GeV}^2$  as a function of the binning variable is needed. This is done in three steps. First different search algorithms, which in H1 are called finders, are applied. In addition some cuts are used on the full sample, to get a mass peak for the  $J/\psi$  events. The second step will be to fit these distributions with a combination of signal and background functions, in order to get the number of  $J/\psi$  events. And the last step will contain the separation of elastic from inelastic events.

The first two steps will be illustrated in this chapter, the last will follow in chapter 8.

### 6.1 Extraction of $J/\psi$ candidates

Since it is not possible to detect a  $J/\psi$  directly due to its too short lifetime, one is forced to look for its stable decay products. In this thesis the elastic lepton decay channel  $J/\psi \rightarrow e^+e^-$  is chosen. Thus the goal is to identify the electrons and positrons from this decay as efficient as possible and reduce the background.

The reconstruction of particles can be separated in two classes and is done due to the appearance in the sub-detector units. If the informations from the tracking system are used, then the particle is labelled with *selected track* or for short with *track*. Alternatively one attaches the reconstruction of a certain particle with *cluster*, if the information is based on the calorimetry detectors. Each class uses different search algorithms<sup>1</sup>, called finders in H1, to give information about momentum, energy and charge. But no particle identification is done at this point.

Looking for two decay products and have two distinguishing properties, track and cluster, leads to three implemented combinations of  $J/\psi$  finders within the H1 software framework: both decay particles are reconstructed by tracks (*track-track*), both by clusters (*cluster-cluster*) and the combination of one track and one cluster (*track-cluster*). Depending on the phase

---

<sup>1</sup>The search algorithm used to find a selected track is located in the class *H1CreateSelTracks* and is based on the Lee West track finder technique, see [29] or look directly into the class. For clusters the finder class *H1CreatePartEm* is used.

space, one is interested in, especially the  $W_{\gamma p}$  region, the proper combination is used. In Appendix C the  $W_{\gamma p}$  region is illustrated according to the three combinations. In this thesis only track-track events are considered, which give access to the lowest region of  $W_{\gamma p}$ <sup>2</sup>.

### 6.1.1 H1 Track Search Algorithm (Finder)

The used tracks are standard H1 tracks, also called *selected tracks* or for short seltracks. Vertex fitted tracks are divided in three groups (central, forward and combined), each with its own cuts. The names are historically based on theta region, but are changed in the release used for this analysis (h1oo 3.3.10). This means central tracks must satisfy  $1^\circ < \theta < 179^\circ$ , forward  $6^\circ < \Theta < 25^\circ$  and combined  $10^\circ < \Theta < 30^\circ$ . Additional cuts such as minimal momentum, minimal transverse momentum, track length and number of hits in the CJC are also required. Since for the used central tracks, the theta cut is almost meaningless, the other cuts will be decisive. They are primary responsible for a quality of the reconstructed trajectory. The detailed cuts are given in table 6.2. Other sources of this subject can be found in [30] or in the *H1TrkFinder* package.

### 6.1.2 H1 Elastic Track-Track $J/\psi$ Search Algorithm (Finder)

Based on the selected tracks, the  $J/\psi$  search algorithm, called H1 elastic  $J/\psi$  finder<sup>3</sup>, is used to look for elastic  $J/\psi$  candidates by applying the cuts listed in table 6.1. The theta region of the tracks is chosen such that only tracks are used which are in the acceptance of the CJC. The transverse momentum of each track needs to exceed the threshold at 0.8 GeV. The tracks must have opposite charge, otherwise the source of them could not be a neutral  $J/\psi$ . And the reconstructed mass of the  $J/\psi$  has to be larger than 1.5 GeV and smaller as 15 GeV. Reconstructed mass means, that the mass of the  $J/\psi$  is calculated by the 4-vectors of the tracks, whereas they are computed on the mass hypothesis of an electron or a muon<sup>4</sup>. Still at this point no particle identification of the tracks is done.

### 6.1.3 Electron Identification

Since no particle identification is applied on the track or elastic  $J/\psi$  finder<sup>5</sup>, the  $J/\psi$  candidate sample still contains a lot of background events. These events are mainly the composition of two pions which coincidentally fit into the mass window. The *H1SoftLeptonID* package provides a method which calculates the probability of the particle being an electron or a

<sup>2</sup>For an elastic  $J/\psi \rightarrow e^+e^-$  analysis with track-cluster and cluster-cluster see [4]; there are also the elastic channels  $J/\psi \rightarrow \mu^+\mu^-$  studied.

<sup>3</sup>Implemented in the *H1FindJPsi* class.

<sup>4</sup>The particle identification for an electron or a muon has to be done afterwards. At this point both mass hypotheses are taken into account. The fulfilling of one of them is enough to accept the event.

<sup>5</sup>The inelastic and the track-cluster  $J/\psi$  finder on the other side use a particle identification.

name of the cut variable	cut condition
Theta of a track/cluster	$20^\circ < \Theta < 165^\circ$
transverse momentum of a track	$p_t > 0.8 \text{ GeV}$
Charge	tracks must have opposite charge
reconstructed mass window	$1.5 \text{ GeV} < m_{ee}, m_{\mu\mu} < 15 \text{ GeV}$
number of tracks	$N_{\text{tracks}} = 2$

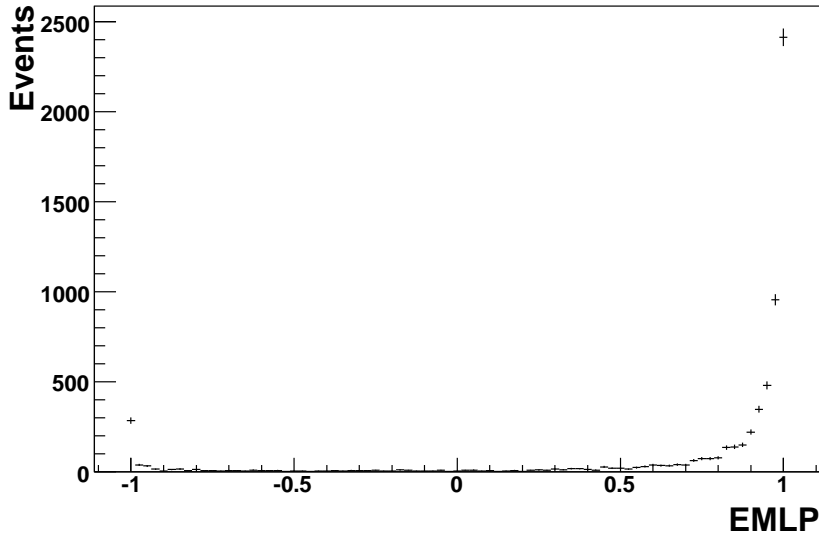
Table 6.1: Cuts applied in the H1 elastic track-track  $J/\psi$  finder.

Figure 6.1: Distribution of the *ElectronMLPDiscriminator* (EMLP) variable for an electron enriched sample. The probability that a track is caused by an electron is increasing towards +1. For this plot  $J/\psi$  candidates are taken with all cuts described in table 6.2 but without the cut  $\text{EMLP} > 0$ . To show the behaviour of this variable for one track the cut  $\text{EMLP} > 0.95$  is applied for the other one, to make sure that this track is an electron. The data are taken from the high energy period of 2007.

pion and gives the variable *ElectronMLPDiscriminator* (EMLP) back. The variable runs from  $-1$  (pion) to  $+1$  (electron). It is based on a neural network with 7 input variables. Details about the input parameters and the methods can be found in [31, 32].

The distribution of the EMLP variable is showed in figure 6.1 for an electron enriched sample. For elastic  $J/\psi$  candidates decaying into two tracks,  $\text{EMLP} > 0.95$  is demanded for the first track, in order to enrich  $J/\psi \rightarrow e^+e^-$  events. Then the EMLP value is plotted for the second track<sup>6</sup>.

For the whole analysis the cut  $\text{EMLP} > 0$  is used.

<sup>6</sup>There are events which lay below  $-1$  (underflow events). These events are extrapolated to fly in a crack and thus do not lie in the geometrical acceptance of the detector. Therefore they are cut off by the EMLP. See section 7.1.

### 6.1.4 Event Selection

To improve the quality of the events in the sample, additional cuts are applied. First the number of tracks are restricted to only two<sup>7</sup>. Therefore the possibility of inelastic events is reduced to those with decay products flying along the beam pipe and therefore cannot be detected by the tracking systems.

Second the vertex offset in the z-direction is limited by  $|z_{Vtx}| < 35$  cm. Tracks which are fitted too far away from the nominal interaction point, can indicate some trouble by the fitting procedure.

In addition an other cut on a variable called elasticity is used. The definition is

$$z = \frac{(E - p_z)_\psi}{\sum_{\text{HFS}} (E - p_z)},$$

but since the number of tracks, from which the kinematic variables of the  $J/\psi$  are calculated, is already restrict to only two, this variable is not very restrictive and has an efficiency nearly by 100 % (see table 7.5).

Finally the theta angle of the tracks is restricted to  $\theta < 140^\circ$ . This cut is needed because the electron pion separation at larger thetas is decreasing, due to the fact the EMLP is restricted to the LAr acceptance.

A summary of the main cuts used in this thesis to select the elastic  $J/\psi \rightarrow e^+e^-$  candidates is given in table 6.2.

## 6.2 Phase Space of the Analysis

In this analysis three different centre of mass energies, 320, 250 and 225 GeV, which correspond to the three different proton momentums 920, 575 and 460 GeV, are at HERA for the first time available. From this it follows, that, compared to earlier measurements, which only had data from proton momentums at 920 GeV (respectively 820 GeV for HERA I), the phase space within the acceptance of the detector is extended towards lower  $W_{\gamma p}$  values. Therefore new measuring points are expected at the lower end of  $W_{\gamma p}$  and reducing the gap between the earlier H1 measurements and the fixed target experiments. In Appendix C the minimal reachable values for  $W_{\gamma p}$  within the acceptance are calculated.

The next step is the decision about the binning of the cross sections. Of course one would like to have as many bins as possible, but one also has to look at the number of events left from the previous cuts. The  $|t|$  and  $W_{\gamma p}$  bins are chosen, such that the statistical and the estimation of the systematic error are of the same order of magnitude. However the total number of events are also taken into account, such that enough bins are left for a fit. In

<sup>7</sup>Actually the constraint to two tracks is only applied if the scattered electron, itself is not identified as a track. If this is the case, three tracks are allowed. See chapter 7.4.

<b>kinematical region</b>	
virtuality	$Q_e^2 < 1 \text{ GeV}^2$
<b>central track definition</b>	
transverse momentum	$p_t > 70 \text{ MeV}$
theta angle	$1^\circ < \Theta < 179^\circ$
number of CJC hits	$N_{\text{CJC}} \geq 0$
track length	$R_{\text{length}} \geq 10 \text{ cm}$ for $\Theta \leq 150^\circ$ $R_{\text{length}} \geq 5 \text{ cm}$ for $\Theta > 150^\circ$
radius of first hit	$R_{\text{start}} \leq 50 \text{ cm}$
dca' value <sup>a</sup>	$ \text{dca}'  \leq 2 \text{ cm}$
<b>elastic track-track <math>J/\psi</math> finder</b>	
theta of a track	$20^\circ < \Theta < 165^\circ$
transverse momentum of a track	$p_t > 0.8 \text{ GeV}$
charge	tracks must have opposite charge
reconstructed mass window	$1.5 \text{ GeV} < m_{ee}, m_{\mu\mu} < 15 \text{ GeV}$
number of tracks	$N_{\text{tracks}} = 2$
<b>selection cuts</b>	
number of tracks w/o scattered electron	$N_{\text{tracks, w/o scat elec}} = 2$
z-vertex	$ z_{\text{Vtx}}  < 35 \text{ cm}$
electron pion separation	$\text{EMLP} > 0$
central tracks	
elasticity	$z > 0.95$
theta of the tracks	$\Theta < 140^\circ$

<sup>a</sup>The dca' value is the distance of the closest approach of non-vertex fitted track to the vertex of this track in the r-phi-plane.

Table 6.2: Overview of the applied cuts for elastic  $J/\psi$  candidates.

table 6.3 the binning in the variables  $|t|$  and  $W_{\gamma p}$  are displayed for the three energies. Since in the high energy data sample is about a factor of 10 more statistics available, than in the medium one, it was possible to use there a finer binning.

### 6.3 Extract the Number of $J/\psi$ Events

An Example of an invariant mass distribution for events selected by the  $J/\psi$  finder and satisfying cuts in table 6.2 is shown in figure 6.2. The invariant mass is calculated according

high energy run period (proton energy $E_p = 919$ GeV)			
Variable	number of bins	Bin edges	Unit
$ t $	11	[0, 0.05, 0.1, 0.15, 0.2, 0.3, 0.4, 0.55, 0.7, 0.9, 1.2]	GeV <sup>2</sup>
$W_{\gamma p}$	11	[40, 50, 60, 70, 80, 90, 100, 110]	GeV
med energy run period (proton energy $E_p = 575$ GeV)			
Variable	number of bins	Bin edges	Unit
$ t $	7	[0, 0.05, 0.1, 0.2, 0.3, 0.5, 0.8, 1.2]	GeV <sup>2</sup>
$W_{\gamma p}$	5	[20, 40, 50, 60, 80]	GeV
low energy run period (proton energy $E_p = 460$ GeV)			
Variable	number of bins	Bin edges	Unit
$ t $	7	[0, 0.05, 0.1, 0.2, 0.3, 0.5, 0.8, 1.2]	GeV <sup>2</sup>
$W_{\gamma p}$	7	[20, 35, 45, 52, 60, 70, 80, 100]	GeV

Table 6.3: Overview of the used binning to calculate the cross section in the variables  $|t|$  and  $W_{\gamma p}$  for the three proton energies used in this thesis.

to the formula

$$m_{e^+e^-} = \sqrt{2m_e^2 + 2|\vec{p}_1||\vec{p}_2|(1 - \cos(\theta_e))}, \quad (6.1)$$

where  $m_e$  is the electron mass,  $p_i$  the momenta of the two found tracks and  $\theta_e$  the angle between these tracks. Besides the expected mass peak around 3.1 GeV, also a broader background distribution is visible.

To determine the differential  $|t|$  and  $W_{\gamma p}$  cross section, it is necessary to determine an invariant mass distribution for each bin described in table 6.3. These distributions are fitted to extract the number of  $J/\psi$  events decaying into two electrons.

As can be seen in figure 6.2 the peak shape is not symmetric. On the left side, the so called radiative tail is visible, due to energy loss of the electrons in the tracking detectors caused by bremsstrahlung. A Gaussian or a Breit-Wigner distribution can therefore not be sufficient for a description, because they use a constant parameter, sigma ( $\sigma$ ) for a Gaussian, to control the behaviour of the shape. Instead a modified Gaussian [25] is used for the signal. It uses, compared to a “normal” Gaussian, an additional parameter  $r$ , which controls the declining on the radiative tail side. The new variable sigma  $\sigma'$  is defined by

$$\sigma' = \sigma + r [ |m - m_\psi| - (m - m_\psi) ].$$

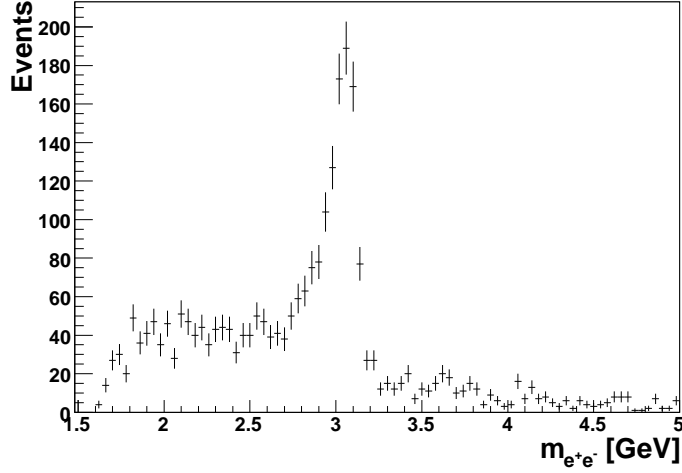


Figure 6.2: Example for an invariant mass distribution for the two electrons taken from the high energy sample in the range  $0 \text{ GeV}^2 < |t| < 0.05 \text{ GeV}^2$ . Only events are used which satisfy all cuts given in table 6.2.

Where  $m_\psi$  means the expectation value of the  $J/\psi$  mass. Thus the signal fitting function is

$$S(m) = N_{\text{sig}} \rho_S(m) \quad \text{with} \quad \rho_S(m) = C_S \exp \left( \frac{(m - m_\psi)^2}{2(\sigma + r[|m - m_\psi| - (m - m_\psi)])^2} \right),$$

where  $N_{\text{sig}}$  represents the number of signal events and  $C_S$  is the normalisation factor such that  $\int \rho_S(m) = 1$ .

The background function was chosen as

$$B(m) = N_{\text{BG}} \rho_{\text{BG}}(m) \quad \text{with} \quad \rho_{\text{BG}}(m) = C_{\text{BG}} (m - c_0)^{c_1} e^{c_2(m - c_0)}.$$

Again  $C_{\text{BG}}$  is the normalisation factor for the background distribution and  $N_{\text{BG}}$  stands for the number of background events. The fit parameters  $c_0$ ,  $c_1$  and  $c_2$  have actually no physical interpretation.

Finally these two distributions are added and form the total fitting function

$$f(m) = S(m) + B(m) = N_{\text{sig}} \rho_S(m) + N_{\text{BG}} \rho_{\text{BG}}(m).$$

The fit is done as an extended likelihood fit with the RooFit package [33]. To get a better convergence performance, first the background function is fitted simultaneously in the sidebands  $[c_0, 2.5]$  and  $[3.5, 5]$ . The signal function is fitted in the peak region  $[2.6, 3.2]$ . Only afterwards the combination is fitted with input parameters taken from the previous fits to the background and the signal. In figure 6.3, 6.4, 6.5, 6.6, 6.7 and 6.8 the fits in  $|t|$  and  $W_{\gamma p}$

bins for the three different energies are shown. The thick blue line represents the combined fit of signal and background distribution, whereas the thin dashed blue line show the background and the red thin line the signal part.

The background drops with increasing  $|t|$  and  $W_{\gamma p}$ . Unfortunately this causes problems with the background fit, since it is getting harder to estimate the background function in the side bands. The cut off at about  $m_{e^+e^-} \simeq 1.6 \text{ GeV}$  is based on the minimal momentum of the tracks ( $p_t^{\text{min}} = 0.8 \text{ GeV}$ ) required by the  $J/\psi$  finder.

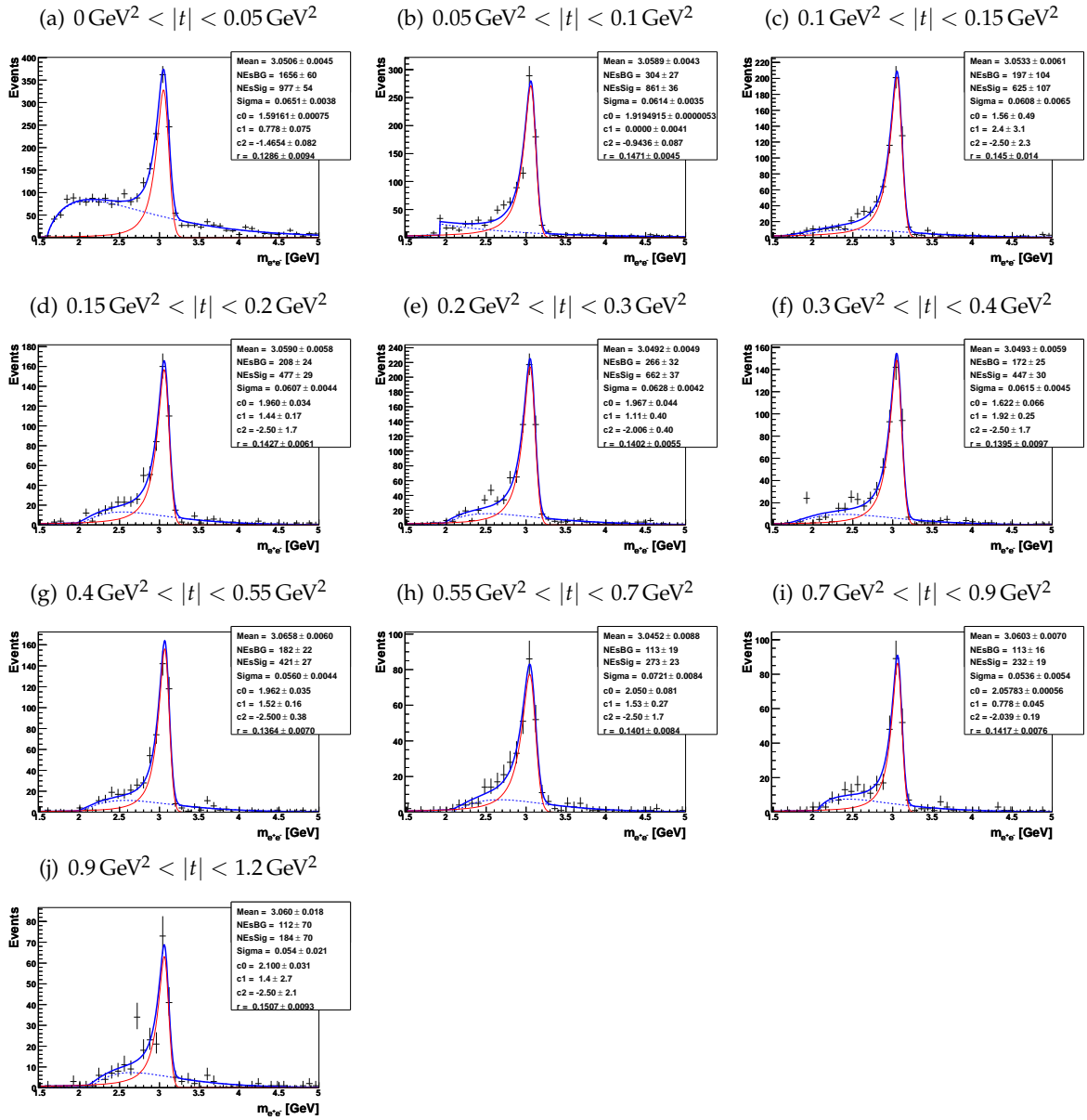


Figure 6.3: Fits of the invariant mass distribution in  $|t|$  bins for high energy period. The thick blue line is the combined fit of background and signal distribution, the dashed thin blue line represents the background and the thin red line the signal function.

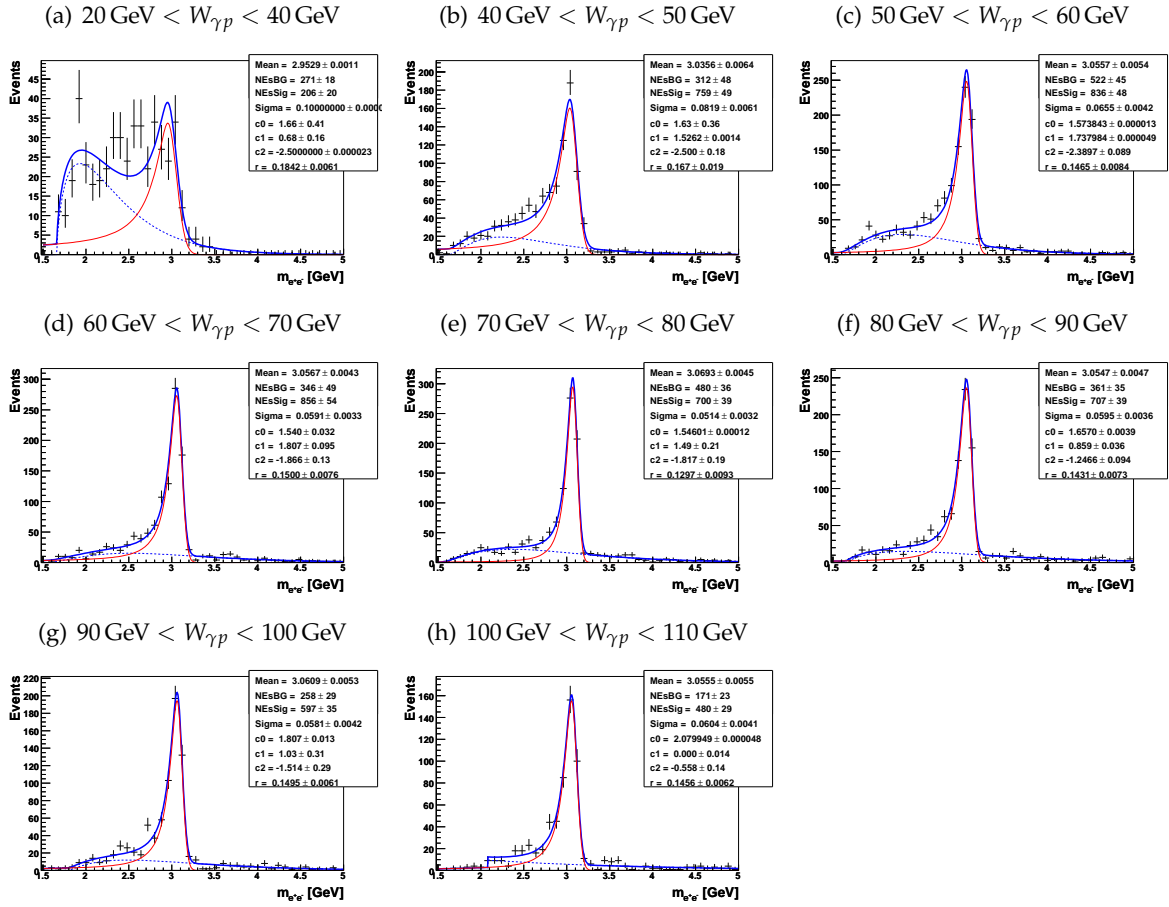


Figure 6.4: Fits of the invariant mass distribution in  $W_{\gamma p}$  bins for high energy period. The thick blue line is the combined fit of background and signal distribution, the dashed thin blue line represents the background and the thin red line the signal function. The first bin is not used for the cross section because of too much background.

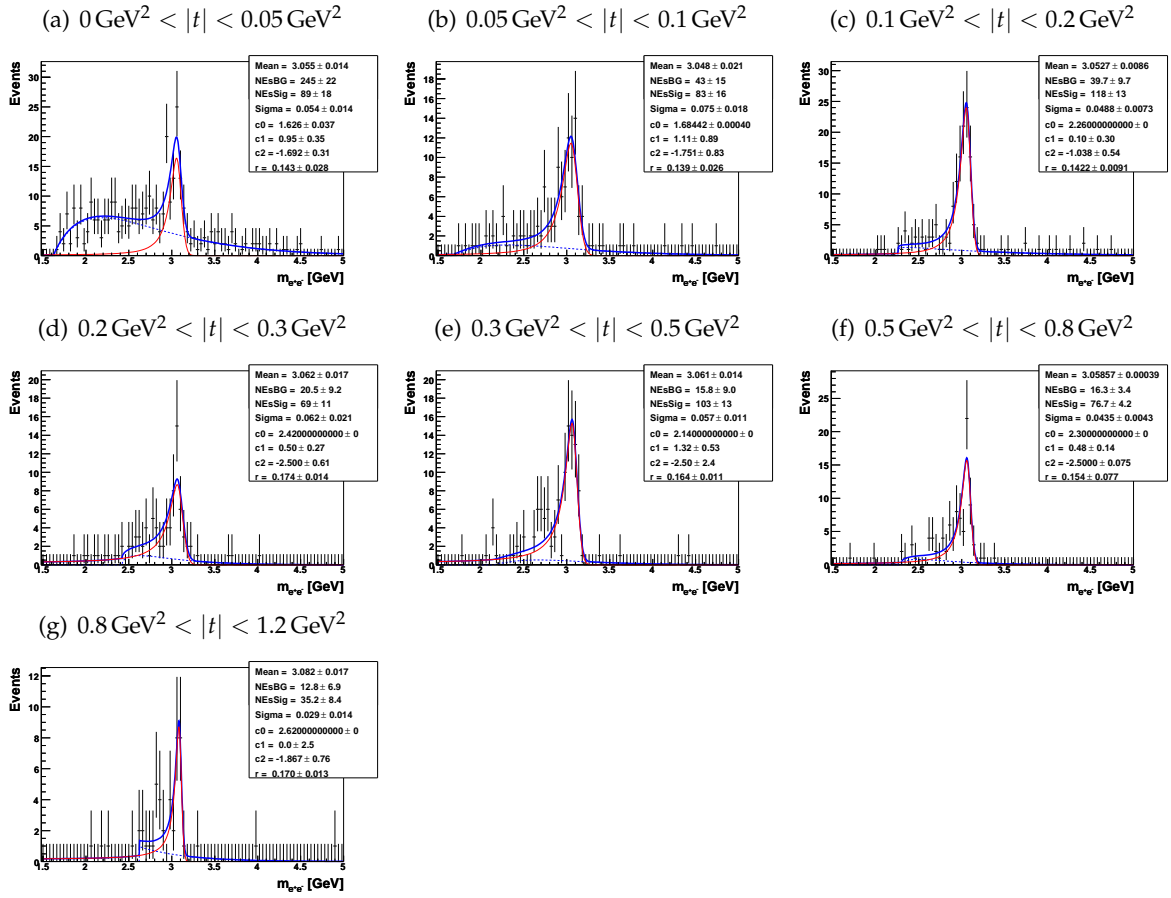


Figure 6.5: Fits of the invariant mass distribution in  $|t|$  bins for medium energy period. The thick blue line is the combined fit of background and signal distribution, the dashed thin blue line represents the background and the thin red line the signal function.

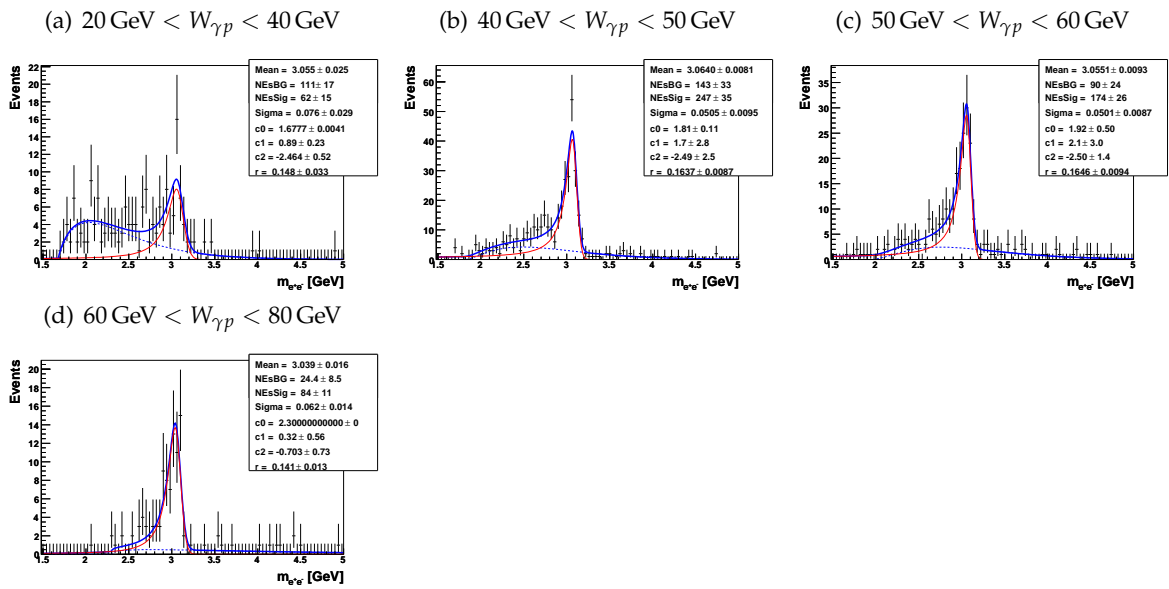


Figure 6.6: Fits of the invariant mass distribution in  $W_{\gamma p}$  bins for medium energy period. The thick blue line is the combined fit of background and signal distribution, the dashed thin blue line represents the background and the thin red line the signal function.

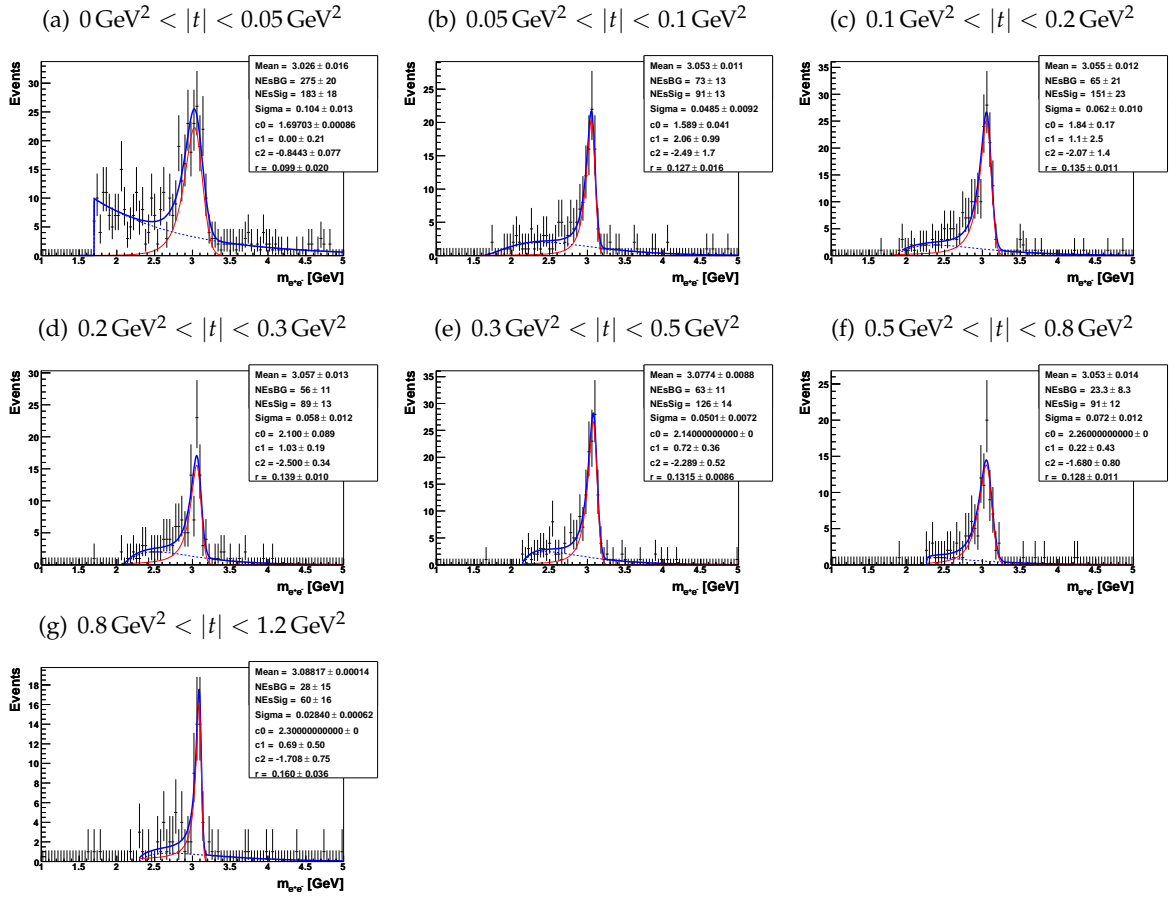


Figure 6.7: Fits of the invariant mass distribution in  $|t|$  bins for low energy period. The thick blue line is the combined fit of background and signal distribution, the dashed thin blue line represents the background and the thin red line the signal function.

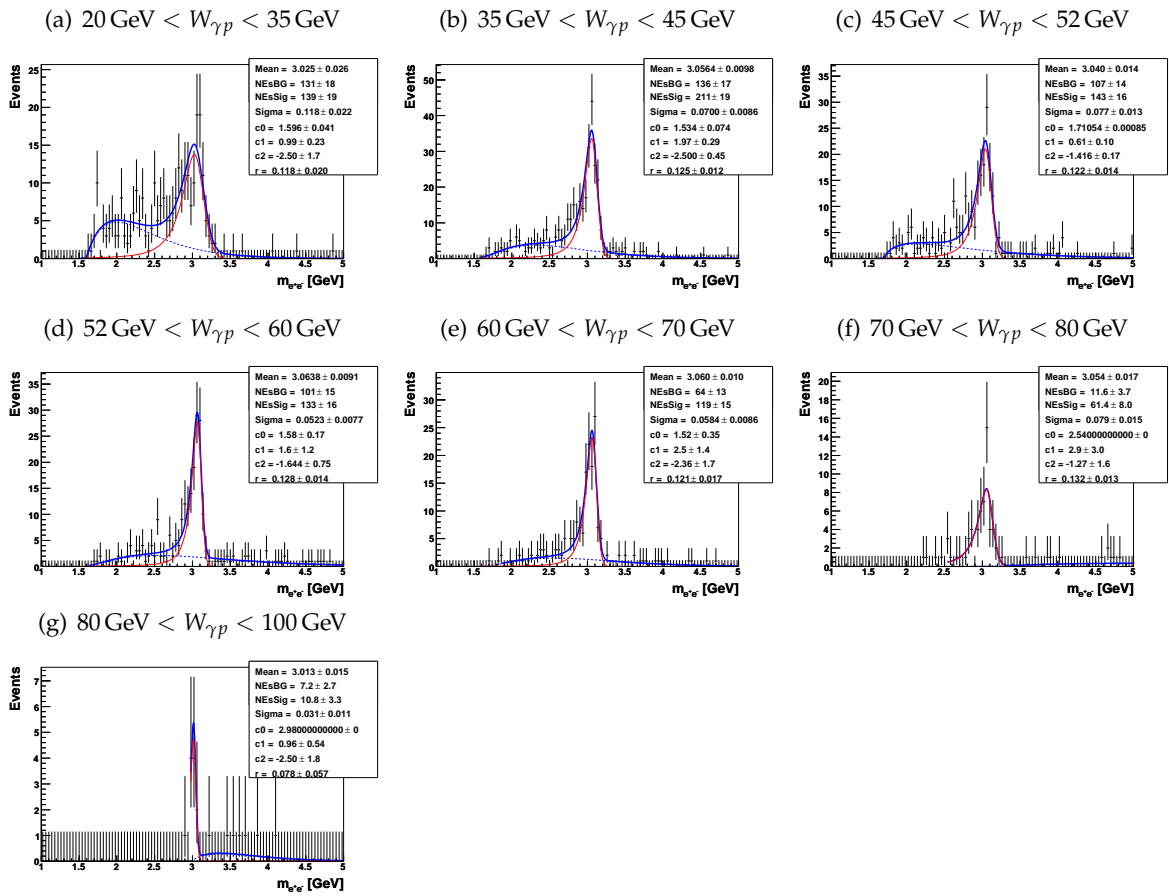


Figure 6.8: Fits of the invariant mass distribution in  $W_{\gamma p}$  bins for low energy period. The thick blue line is the combined fit of background and signal distribution, the dashed thin blue line represents the background and the thin red line the signal function.



# Chapter 7

## Efficiencies

In the last chapter the number of  $J/\psi \rightarrow e^+e^-$  events are calculated. Here the other important ingredients to calculate the cross section, the efficiencies, are examined. There are three different parts which form together the total efficiency. The first inefficiency is related to the detector. The second part of inefficiencies accounts for the selection cuts, since not only background events are thrown away. However the separation of these two is artificial. Finally the third inefficiency is due to the triggering conditions.

In the following all three parts will be described.

### 7.1 Geometric Acceptance and Reconstruction Efficiency

The geometric acceptance of a detector describes the fraction of particles which could have possibly be seen by the detector, i.e. where the detector has actually sensitive material to detect particles. The inefficiency is partly based on the beam pipe and the cracks<sup>1</sup>, where no sensitive material exist. But actually the main contribution is based on the geometric design of the CJC, which is needed to reconstruct the trajectory of the tracks. Also the acceptance of the EMLP and the cut  $\Theta_T < 140^\circ$  belongs to this group. Since not all particles, which fly through detector sensitive material, cause a reconstructible signal in the detector, an additional inefficiency, called single particle reconstruction efficiency, has to be considered.

The geometric acceptance and reconstruction efficiency could be calculated from measured data, but in this thesis MC is used. This is possible, because it was already shown in chapter 4 that MC and data are in well agreement.

The combination of geometric acceptance and reconstruction efficiency is described by

$$\epsilon_{acc+rec} = \frac{N_{J/\psi}^{rec}}{N_{J/\psi}^{gen}}, \quad (7.1)$$

where  $N_{J/\psi}^{rec}$  means the number of  $J/\psi$  candidates found by the elastic track-track  $J/\psi$  finder and satisfying  $\Theta_T < 140^\circ$  and EMLP  $> -1$  are considered. Whereas the cut EMLP  $> -1$

---

<sup>1</sup>Passage between two detector modules on a barrel, where the detector is not or less sensitive is called a ( $\phi$ -)crack. For example the dead area between the 8 LAr modules on a barrel. In these regions the *ElectronMLPDiscriminator* (EMLP) does not work.

discards all events in a LAr crack and  $N_{J/\psi}^{\text{gen}}$  is the number of generated  $J/\psi$  events.

Figure 7.1 shows the geometric acceptance and reconstruction efficiency  $\varepsilon_{\text{acc+rec}}$  for the three energy regions (high, med(ium) and low) as function of  $|t|$  (a,b) and  $W_{\gamma p}$  (c,d). The given error bars show the statistical errors on the MC sample. Two binnings are displayed (a,c) are equidistant and (b,d) use the same binning as in the data. In Figure 7.2 this efficiency is displayed as a function of the theta angle of both lepton tracks,  $\Theta_T$ , (a), and of theta for only the track with smaller (larger) theta,  $\Theta_{\text{low}}$  ( $\Theta_{\text{high}}$ ) (b)-(c). The transverse momentum of both tracks,  $p_{t,T}$ , and transverse momentum for only the track with smaller (larger) transverse momentum,  $p_{t,\text{low}}$  ( $p_{t,\text{high}}$ ), is given in (d)-(f). In the plots in figure 7.1 and 7.2 only events in the kinematic region of photoproduction ( $Q_e^2 < 1 \text{ GeV}^2$ ) are considered.

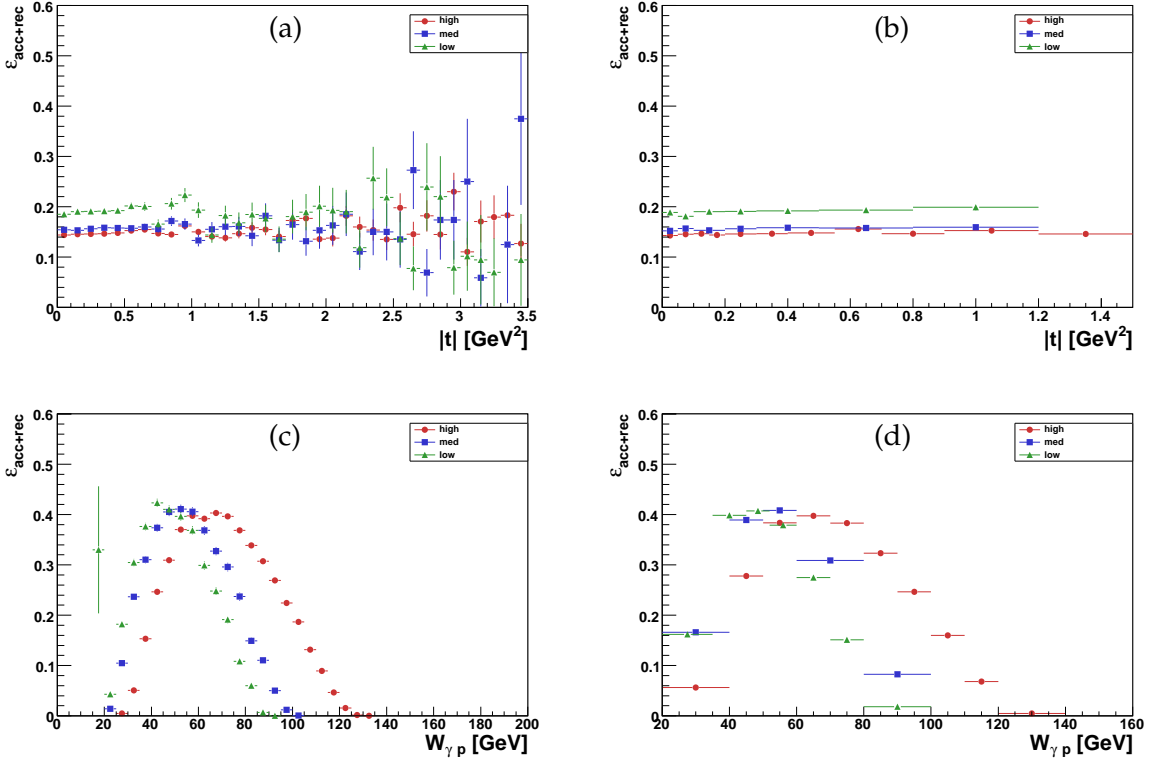


Figure 7.1: Geometric acceptance and reconstruction efficiency of the H1 detector for the three energy regions (high are red circles, medium are blue squares and low are green triangles) calculated from the elastic DiffVM MC samples. The efficiencies are shown as a function of  $|t|$  (a,b) and  $W_{\gamma p}$  (c,d). (a,c) use an equidistant binning and (b,d) use the same binning as in the data. The error bars show the statistical errors.

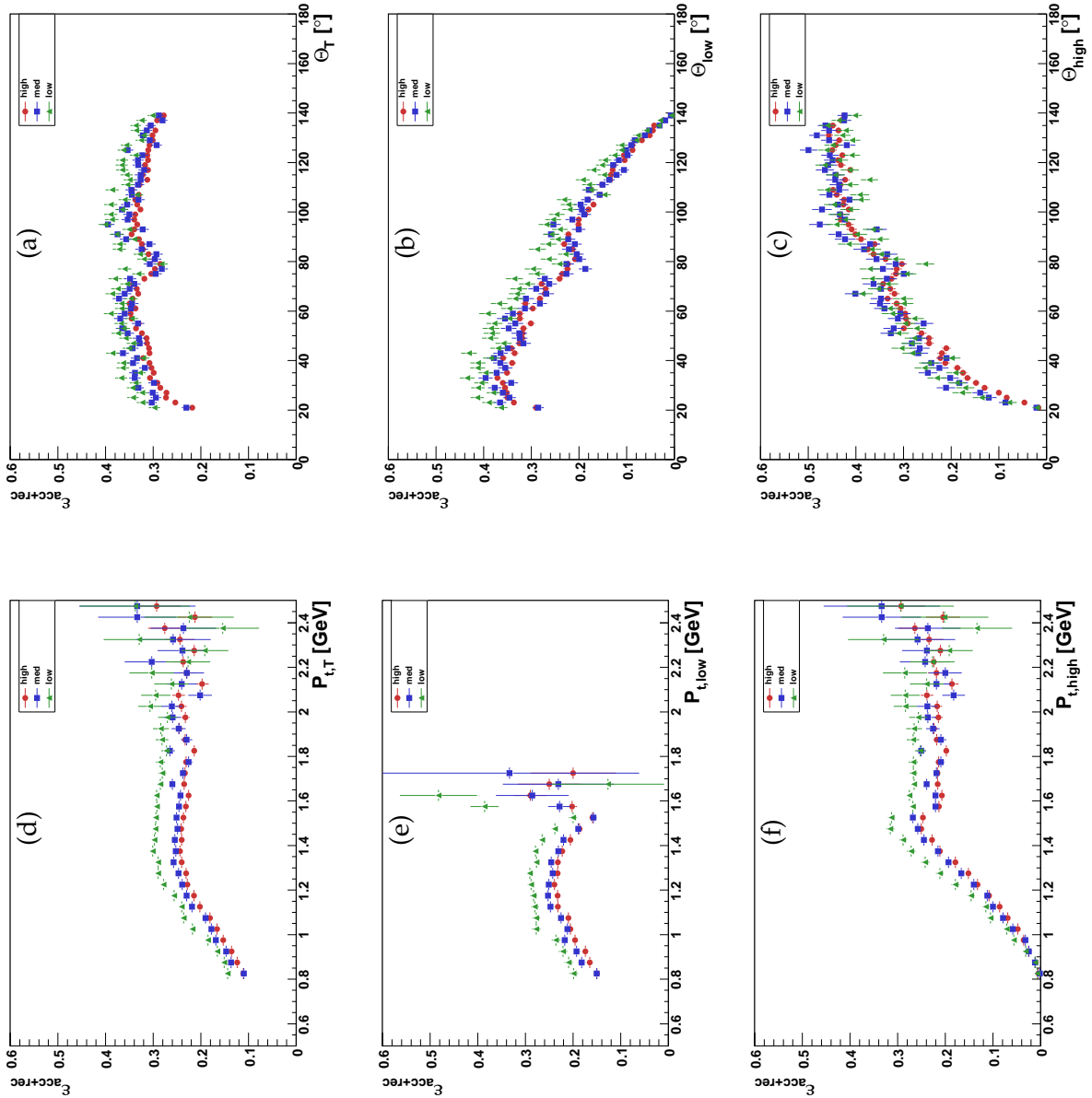


Figure 7.2: Geometric acceptance and reconstruction efficiency of the H1 detector for the three energy regions (high are red circles, medium are blue squares and low are green triangles) calculated from the elastic DiffVM MC samples. The efficiencies are shown as a function of the theta angle of both tracks  $\Theta_T$  (a), theta of the track with smaller (larger) theta  $\Theta_{\text{low}}$  ( $\Theta_{\text{high}}$ ) (b),(c), transverse momentum of both tracks  $p_{t,T}$  (d), transverse momentum of the tracks with smaller (larger)  $p_t$   $p_{t,\text{low}}$  ( $p_{t,\text{high}}$ ) (e), (f). The error bars show the statistical errors.

## 7.2 Selection Efficiency

The events reconstructed in the geometrical acceptance of the detector have to satisfy the selection cuts, listed in table 6.2, apart from the cut  $\Theta < 140^\circ$  already applied for the acceptance/reconstruction efficiency. Additionally the  $t$  and  $W_{\gamma p}$  region cuts are used. The selection efficiency is given by

$$\varepsilon_{sel} = \frac{N_{J/\psi}^{\text{rec,sel}}}{N_{J/\psi}^{\text{rec}}}, \quad (7.2)$$

where  $N_{J/\psi}^{\text{rec,sel}}$  are the number of elastic track-track  $J/\psi$  candidates in the geometric acceptance, that are reconstructed and passed the selection and phase space region cuts of  $|t|$  and  $W_{\gamma p}$ .  $N_{J/\psi}^{\text{rec}}$  are the elastic track-track  $J/\psi$  candidates which are reconstructed and satisfy the geometric acceptance.

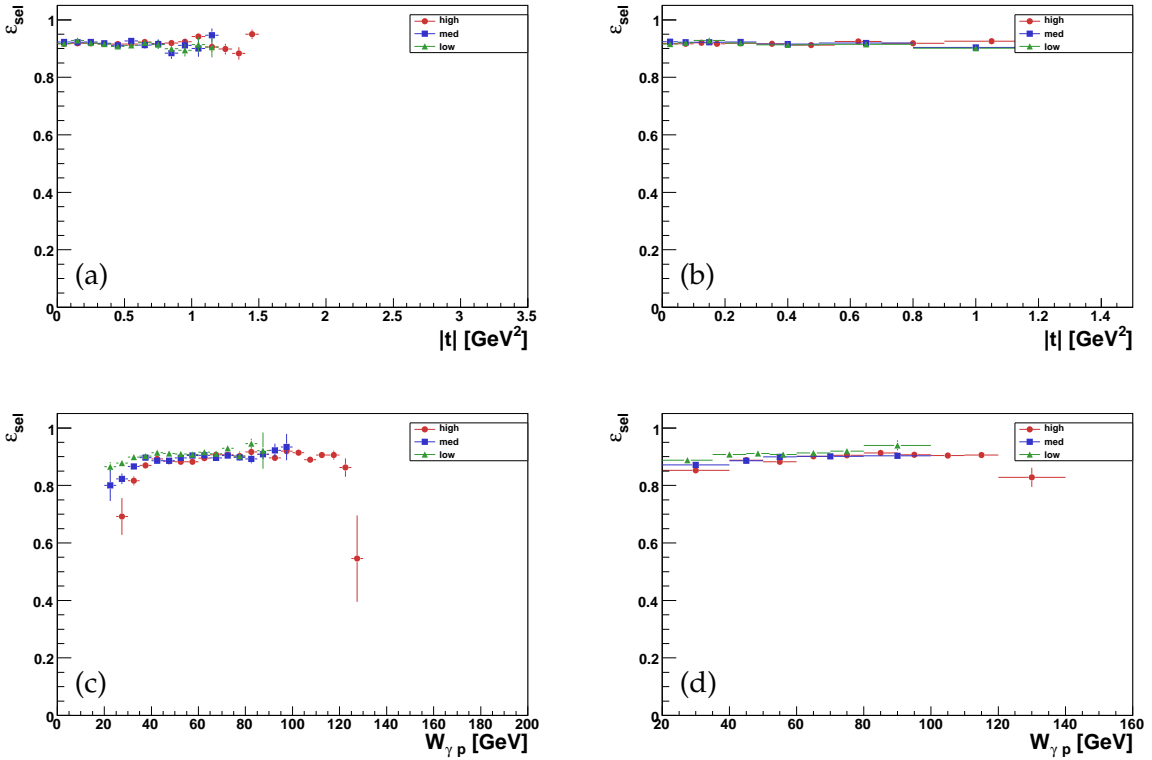


Figure 7.3: Selection cut (cuts specified in table 6.2, but the cut  $\Theta < 140^\circ$  is not used) efficiency of the H1 detector for the three energy regions (high are red circles, medium are blue squares and low are green triangles) calculated from the elastic DiffVM MC samples. The variables  $|t|$  (a,b) and  $W_{\gamma p}$  (c,d) are shown. (a,c) use an equidistant binning and (b,d) use the same binning as in the data. The error bars show the statistical errors.

The overall selection efficiency of all these cuts are shown in figure 7.3 and 7.4 for the same variables as in section 7.1. (The given error bars show the statistical errors on the MC sample.) Again only events with  $Q_e^2 < 1 \text{ GeV}^2$  are used.

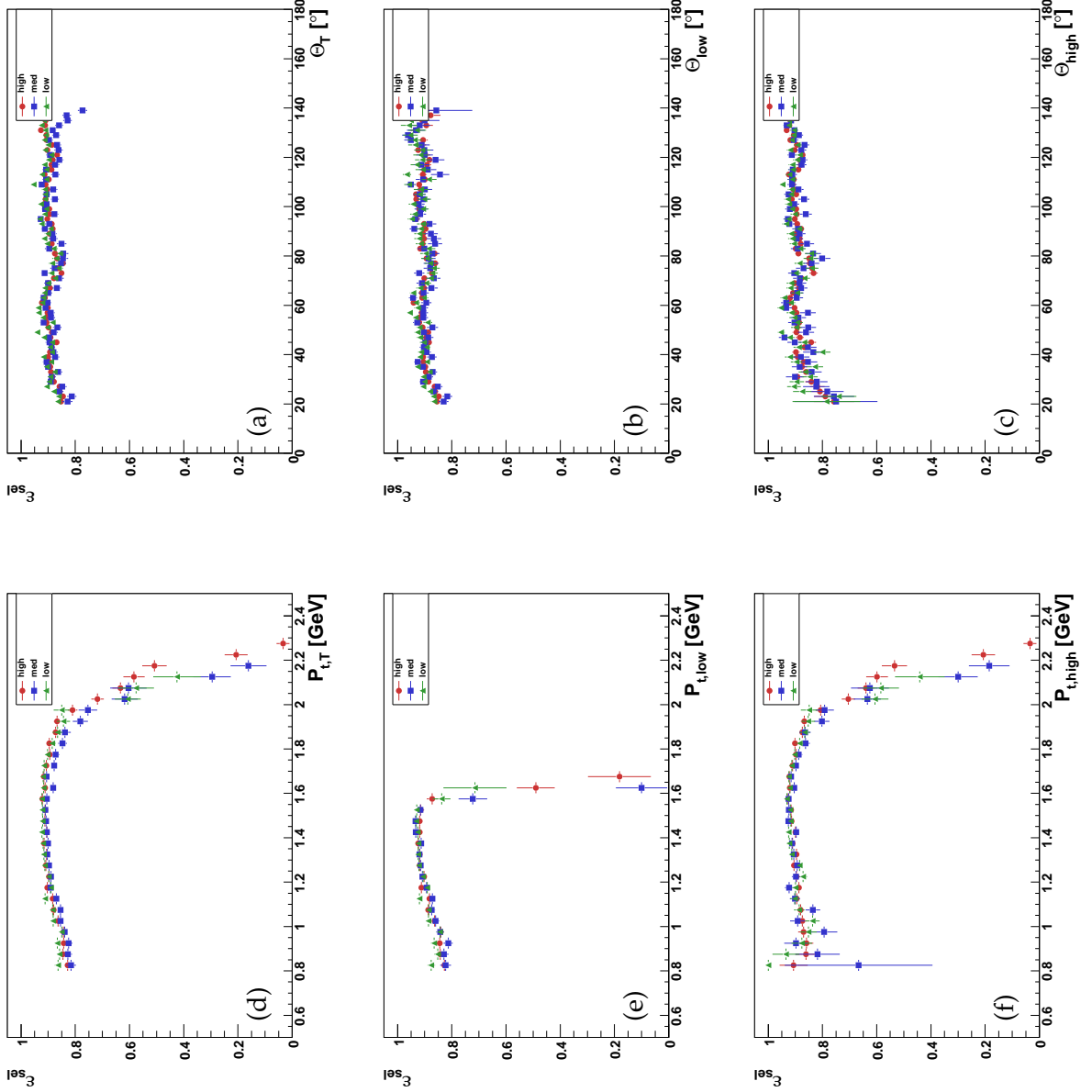


Figure 7.4: Selection cut (all cuts specified in table 6.2, except the cut  $\Theta < 140^\circ$  is not used) efficiency of the H1 detector for the three energy regions (high are red circles, medium are blue squares and low are green triangles) calculated from the elastic DiffVM MC samples. The variables  $|t|$  (a,b) and  $W_{\gamma p}$  (c,d) are shown. (a,c) use an equidistant binning and (b,d) use the same binning as in the data. The efficiencies are shown as a function of the theta angle of both tracks  $\Theta_T$  (a), theta of the track with smaller (larger) theta  $\Theta_{\text{low}}$  ( $\Theta_{\text{high}}$ ) (b),(c), transverse momentum of both tracks  $p_{t,T}$  (d), transverse momentum of the tracks with smaller (larger)  $p_t$   $p_{t,\text{low}}$  ( $p_{t,\text{high}}$ ) (e), (f). The error bars show the statistical errors.

The plots show that the inefficiencies from these cuts are quite small and the efficiencies are around 90%. Therefore the main inefficiency is not produced by the selection cuts, but

by the acceptance/reconstruction given from the detector. This also means that the electron identification, done by the EMLP, has a high selection efficiency.

To a better understanding which cut variable causes the inefficiencies, the cuts are sequential applied by a logical AND. This is shown in figure 7.5. Supplementary to the cuts given in table 6.2 the elastic track-track  $J/\psi$  finder is split in its components. The variable  $NumJPsi$  means the number of  $J/\psi$  events found by all finders together.  $JPsi$  track track requires also that the found  $J/\psi$  are reconstructed by two tracks and  $JPsi$  elastic that they found by the elastic  $J/\psi$  finder.

As mentioned above the main inefficiency from the electron identification through the variable EMLP is based on the acceptance, due to the cracks. In figure 7.5 only the combination of crack rejection and electron identification is given. The efficiency taken is  $\varepsilon = \frac{N(\text{MLP}>0)}{N} = \varepsilon_{\text{crack}}\varepsilon_{\text{elec id}}$ , whereas the crack efficiency is given by  $\varepsilon_{\text{crack}} = \frac{N(\text{MLP}>-1)}{N}$  and the pure electron identification is  $\varepsilon_{\text{elec id}} = \frac{N(\text{MLP}>0)}{N(\text{MLP}>-1)}$ .

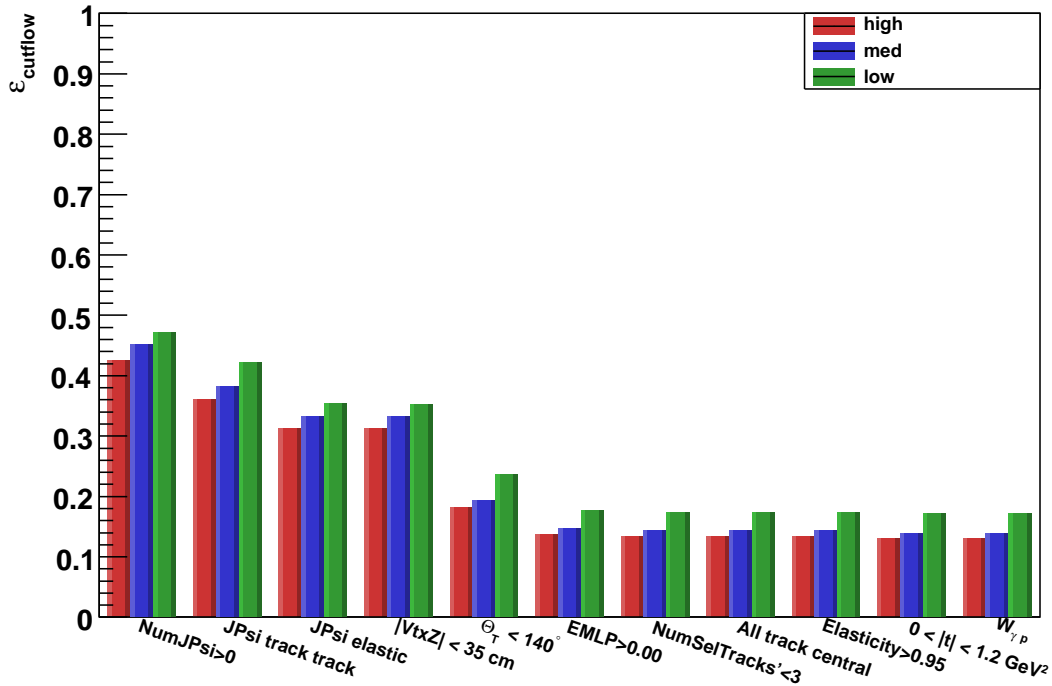


Figure 7.5: The efficiency showed in a bin uses all left cuts and the cut from the binning itself. For the whole sample only photoproduced events ( $Q_e^2 < 1$ ) are used.  $NumJPsi$  is the number of  $J/\psi$  events found by all  $J/\psi$  finders.  $JPsi$  track track means the number of  $J/\psi$  found by the track-track  $J/\psi$  finder,  $JPsi$  elastic are the number of elastic track-track  $J/\psi$  found by the corresponding finder. The plots are produced from the DiffVM MC samples for the three energy regions. The red bars represent the high energy sample, blue the medium and green the low one. The last bin shows the additional cut on the  $W_{\gamma p}$  region given in table 6.3.

### 7.3 Combined Acceptance and Selection Efficiency

The total efficiency, i.e. the product of acceptance, reconstruction and selection efficiency is shown in figure 7.6 as a function of  $|t|$  and  $W_{\gamma p}$ .

As can be seen in the plots, the total efficiency in  $|t|$  shows the same behaviour for all three energy regions. There is a small difference between them of about 2%. The source of this deviation is not clear and would require further investigation.

In  $W_{\gamma p}$  the peak of the efficiency is shifted with respect to lower  $W_{\gamma p}$  for the low and medium energy run. This is expected because the geometry of the detector is not changed for the different centre of mass energies  $s$ , but the dependence of  $W_{\gamma p}$  on  $s$  is

$$W_{\gamma p} \propto \sqrt{s},$$

as shown in Appendix C. Therefore a shift of about  $\sqrt{\frac{460 \text{ GeV}}{920 \text{ GeV}}} \simeq 0.7$  from the high energy period to the low energy period makes perfectly sense.

### 7.4 Trigger Efficiency

In contrast to the efficiencies described in the previous sections, the trigger efficiency can be calculated directly from the data, if it is possible to find an independent reference sample. For this a sub-trigger is needed, which does not share any trigger conditions with the efficiencies to calculate for.

If such a reference trigger – also called monitor trigger – exists, the trigger efficiency can be calculated by

$$\epsilon_{\text{trigger}} = \frac{N_{\text{mon \&\& trigger}}}{N_{\text{mon}}},$$

where  $N_{\text{mon}}$  represents the number of events the monitor trigger was firing and  $N_{\text{mon \&\& trigger}}$  the number of events the monitor trigger and the trigger were turned on.

There exist a collection of SpaCal-triggers which fulfil the condition of independent trigger elements. In this thesis as monitor trigger  $s0$ ,  $s1$ ,  $s2$  and  $s3$  are used. However events triggered by the SpaCal detector typically have  $Q^2 > 1 \text{ GeV}^2$ , but the analysis is only considering photoproduction events with  $Q^2 < 1 \text{ GeV}^2$ . To obtain a reasonable sample, the cut  $Q_e^2 < 1$  is omitted for the trigger efficiency calculation from data, but kept for MC. The other cuts are the same as used for the analysis, so all cuts given in table 6.2 and the cuts for the  $W_{\gamma p}$  region. Only the cut on  $|t|$  is relaxed to  $|t| < 3.2 \text{ GeV}^2$ , which correspond to  $P_{t,J/\psi} < 1.8 \text{ GeV}$ .

Events with  $Q_e^2 > 1 \text{ GeV}^2$ , as allowed in the data sample, have a scattered electron with an angle  $\Theta'_e$  drifting away from  $\pi$ , see equation 2.2. Therefore with increasing  $Q_e^2$  the trajectory of the scattered electron will reach the geometric acceptance of the CJC and thus can

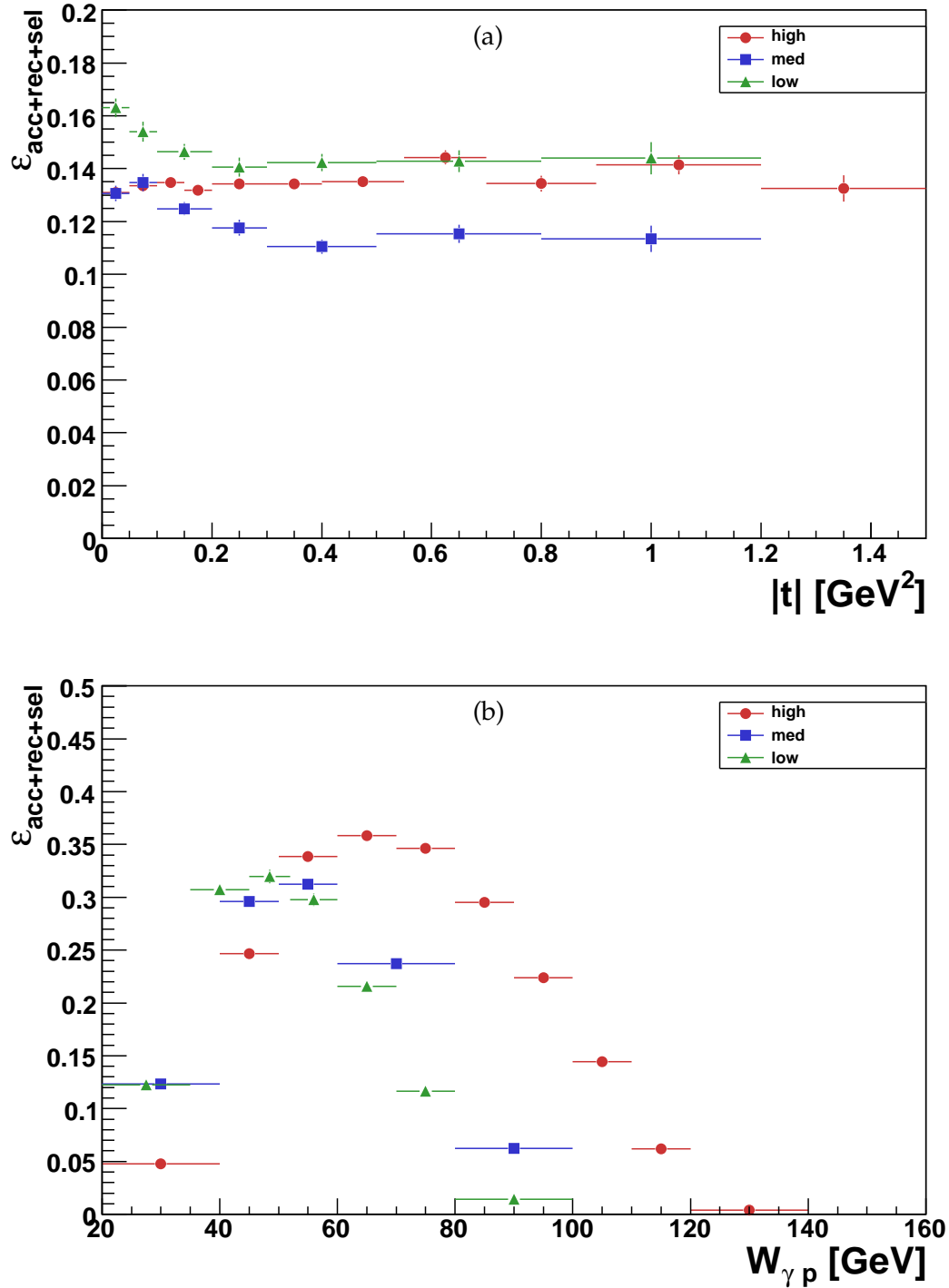


Figure 7.6: Acceptance, reconstruction and selection efficiency for the three energy regions calculated from the elastic DiffVM MC samples. It is shown in the variables  $|t|$  (a) and  $W_{\gamma p}$  (b). For photoproduction events with  $Q_e^2 < 1$  GeV. The error bars indicate the statistical uncertainty.

produce an additional track. Therefore it is possible that an event with an elastic produced  $J/\psi$  decaying into two electrons will generate three tracks. This case has to be considered, therefore the variable  $N_{\text{tracks, w/o scat elec}}$  is defined. It counts all tracks but subtract one, if it is identified as the scattered electron. As indicated in table 6.2 the cut used is  $N_{\text{tracks, w/o scat elec}} = 2$ .

To get better statistical accuracy, it would be preferable to use the trigger simulation instead of the data. This procedure is permitted if the MC simulation, especially the FTT simulation, has been proven to describe the data properly, which for instance is shown in [34, 35]. An additional crosscheck for the sub-trigger  $s59$  is given in figure 7.7 and 7.8, where the efficiency from data is compared to the one calculated from MC. In figure 7.7 the trigger efficiency is shown as a function of the transverse momentum of the  $J/\psi$ ,  $P_{t,J/\psi}$ , (a),  $W_{\gamma p}$ , (b) the theta angle of the  $J/\psi$ ,  $\Theta_{J/\psi}$ , (c) and the phi angle of the tracks,  $\phi_T$ , (d). In figure 7.8 as a function of the transverse momentum,  $P_{t,T}$ , of both tracks (a) and of the smaller (larger) (b),(c) transverse momentum,  $P_{t,low}$  ( $P_{t,high}$ ), are given and the theta angle,  $\Theta_T$ , for both tracks (d) and for the smaller (larger) (e),(f) angle,  $\Theta_{low}$  ( $\Theta_{high}$ ).

In order to increase the number of events in the data, the whole data sample from 2006/07 running with all three energies samples are used. But only the 2006 runs are considered with the same  $s59$  trigger conditions as they were applied for 2007.

Because MC agrees with data, for the calculation of the cross section the trigger efficiency will be taken from MC simulation instead of the one calculated by data. This procedure then also allows to determine the trigger efficiency,  $\varepsilon_{\text{Trigger}}$ , in regions of  $|t|$ , where the data do not provide statistically sufficient samples.

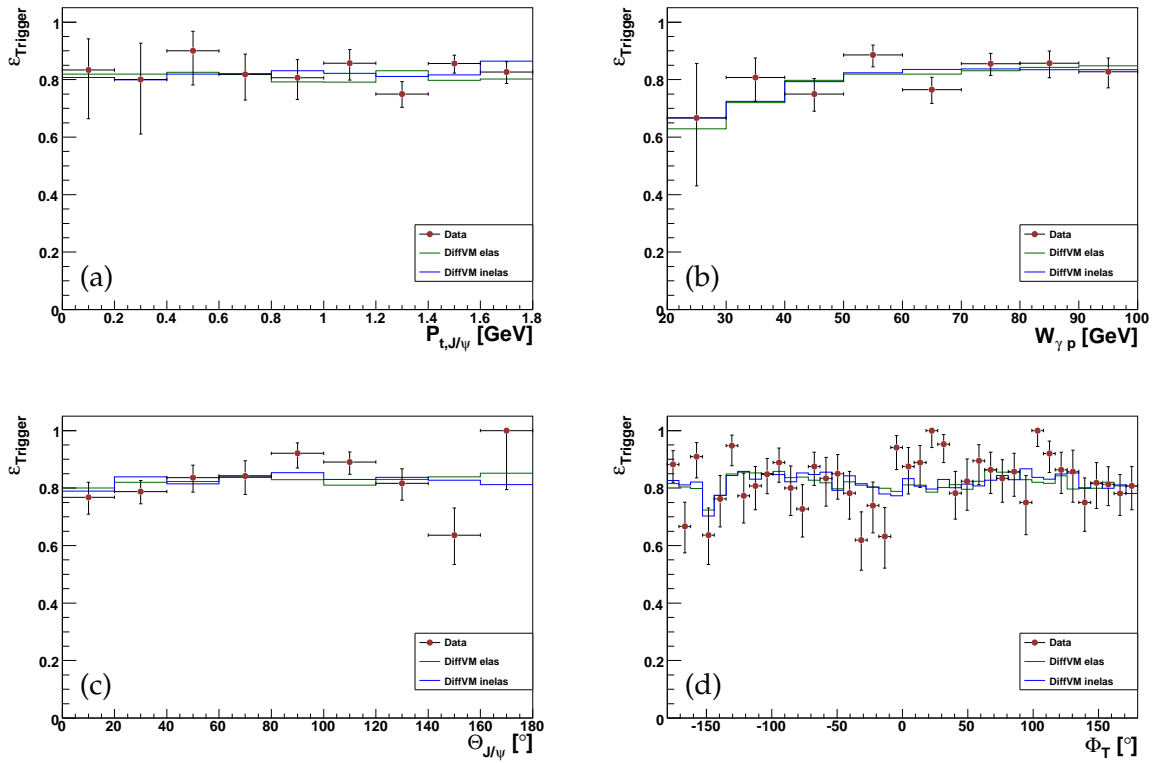


Figure 7.7: Comparison of the trigger efficiency,  $\epsilon_{\text{Trigger}}$ , of the  $s59$  sub-trigger determined from data (red points), from elastic (green) and inelastic (blue) MC as functions of the transverse momentum of the  $J/\psi$ ,  $P_{t,J/\psi}$ , (a),  $W_{\gamma p}$  (b), theta angle of the  $J/\psi$ ,  $\Theta_{J/\psi}$ , (c) and the phi angle of the lepton tracks,  $\phi_T$ , (d). For the data all events from 2006/07 are taken into account.

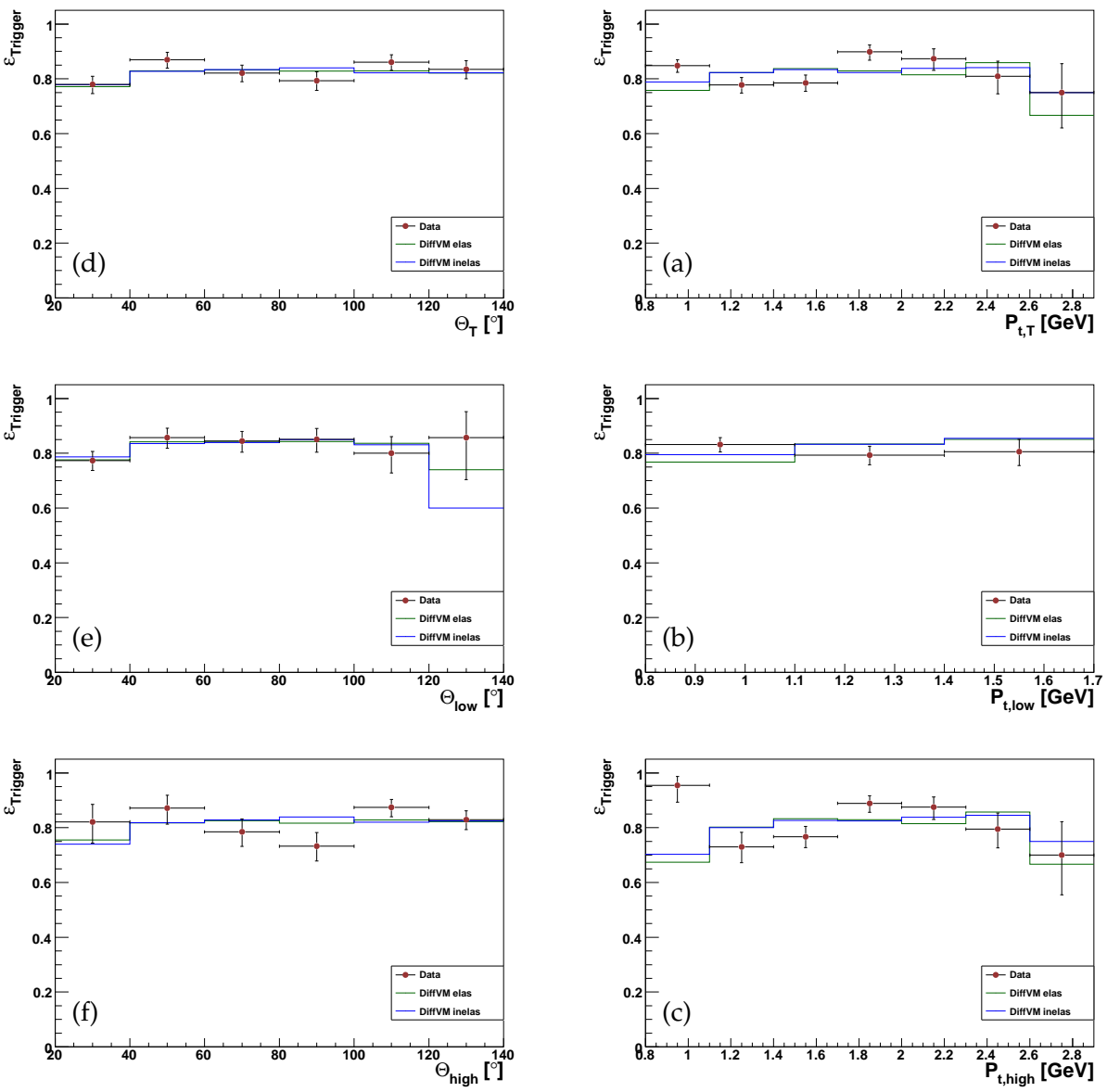


Figure 7.8: Comparison of the trigger efficiency,  $\epsilon_{\text{Trigger}}$ , of the s59 sub-trigger determined from data (red points), from elastic (green) and inelastic (blue) MC as functions of the transverse momentum,  $P_{t,T}$ , of both lepton tracks (a), transverse momentum of the track with smaller (larger)  $p_{t,}$   $P_{t,low}$  ( $P_{t,high}$ ), (b)/(c), the theta angle,  $\Theta_T$ , of both lepton tracks (d) and the theta angle of the track with smaller (larger) theta,  $\Theta_{low}$  ( $\Theta_{high}$ ), (e)/(f). For the data all events from 2006/07 are taken into account.



# Chapter 8

## Elastic Event Selection

In chapter 6 the extraction of the number of  $J/\psi \rightarrow e^+e^-$  events in the chosen  $|t|$  and  $W_{\gamma p}$  bins was performed. But the final goal is still to measure the elastic cross section, without contribution from inelastic processes. Therefore the inelastic events have to be separated from the elastic ones. If it would be possible to find a variable in which those two separate well, one simply could cut on it, but such a variable does – unfortunately – not exist. Instead a different technique will be used.

Inelastic events do not have an outgoing proton, instead hadrons which should be directed along the beam pipe as well, are expected. But there should be also a spread in the transverse direction of these hadrons. This spread can be used to detect inelastic events. But still there are inelastic events which are not detected because the spread is too small, which even increases with higher  $|t|$ , or for reason of detector inefficiencies. But on the other side – and that is the crucial point – also elastic events can produce a signal, since the proton can interact or even hit the beam pipe (which also increases with higher  $|t|$  [9]), or a signal occurs just induced by a background process. Further it is possible that a signal is produced based only on electronic noise<sup>1</sup>.

Therefore one has to correct for this misinterpretation of elastic as inelastic events and vice versa. This will be done by unfolding.

### 8.1 Forward Tagging

If a signal occurs in one of the forward detectors (see below) one is not able to say, whether it is caused by an inelastic or by an elastic event. Hence a signal in one of the forward detectors, which exceeds the threshold of the applied cut, will be referred as an inelastic tagged event; or simply as a tagged event.

Four forward detectors, the PLUG calorimeter (PLUG), the liquid argon detector (LAr10)<sup>2</sup>,

---

<sup>1</sup>In this thesis contribution from electronic noise was not taken into account. In first order this effect is negligible but for a better understanding of the differences between data and MC this effect should be considered.

<sup>2</sup>For tagging inelastic events with the liquid argon detector (LAr) normally the energy deposition with  $\theta < 10^\circ$  is taken. As abbreviation is used LAr10.

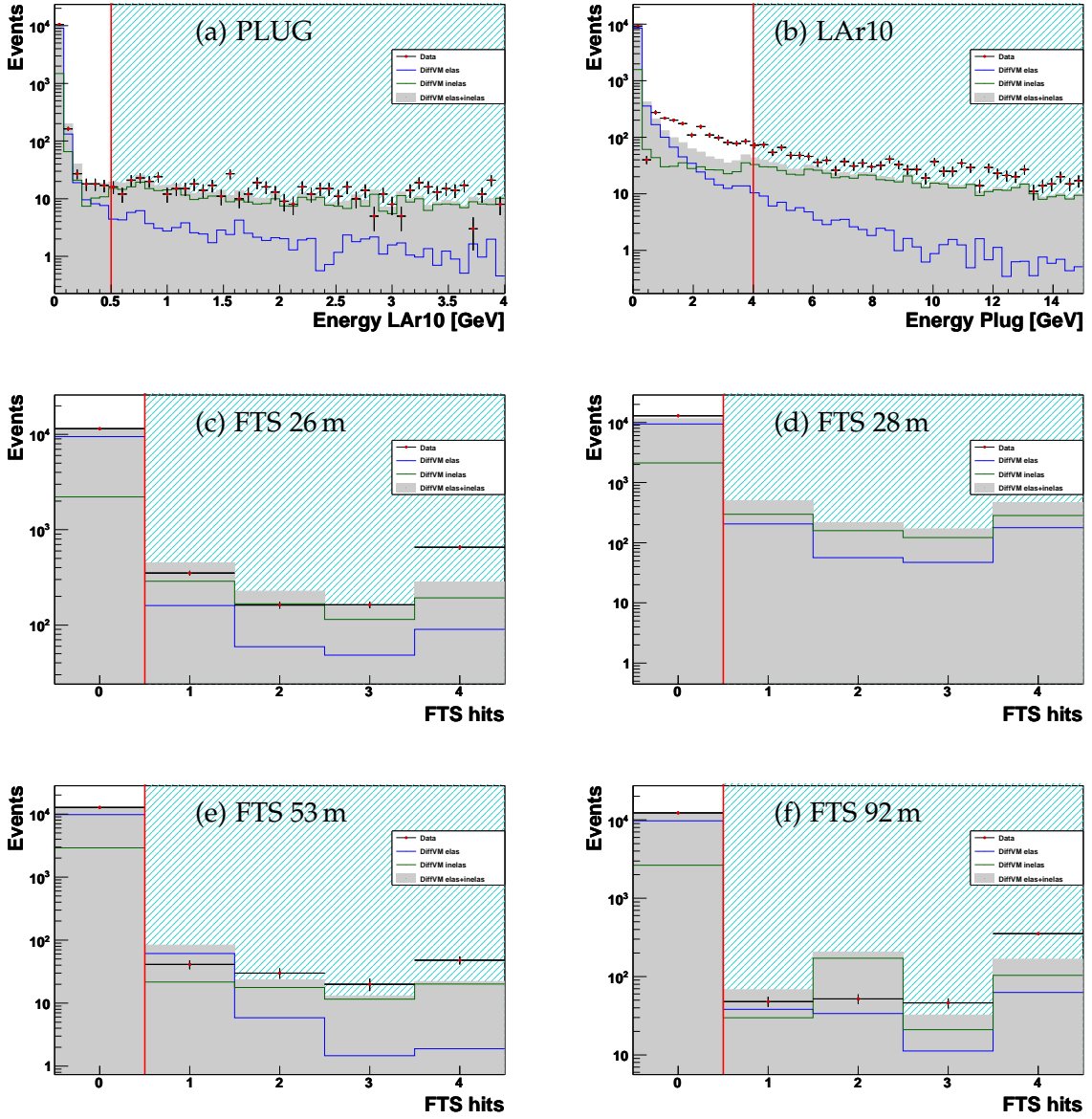


Figure 8.1: Hit multiplicity for PLUG (a), LAr10 (b), FTS layer 1 at  $z = 26$  m (c), FTS layer 2 at  $z = 28$  m (d), FTS layer 1 at  $z = 53$  m (e) and FTS layer 1 at  $z = 92$  m (f) detectors. Only high energy data are displayed. The vertical red lines mark the beginning of the tagging region (green shaded). The green histograms represent the elastic, the blue the inelastic MC events; stacked they give the grey filled histograms. The red points are the data.

the forward muon detector (FMD) and the forward tagging system (FTS), are available for this tagging. (Details to the forward detectors can be found in [18] for LAr, PLUG and FMD.)

To check that the simulation describes the forward detectors, the hit multiplicity of these

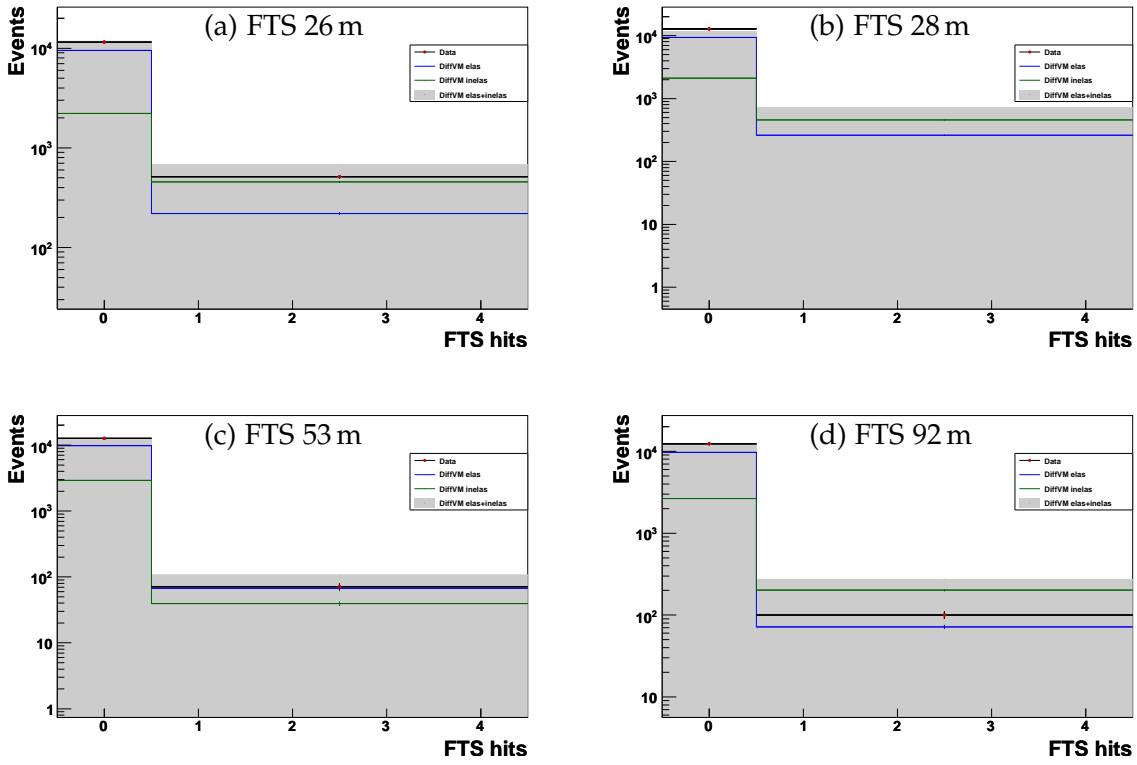


Figure 8.2: Same hit distributions as in figure 8.1 for the four FTS layers (a)-(d), but the bins for 2, 3 and 4 hits are combined and displayed in one bin. Again only high energy data are displayed.

detectors are compared with the data. Hit multiplicity plots show the number events against the number of hits in the FMD and FTS detectors and for PLUG and LAr10 the number of events against the deposit energy in the calorimeter. They are given in figure 8.1 - 8.2 for the high energy run.

The LAr10 detector hit multiplicity is given in figure 8.1(a) and shows a very good description of the simulation. Nearly as good is the description of the PLUG calorimeter shown in 8.1(b). The hit multiplicity for the four layers of the FTS detectors are displayed in 8.1(c)-(f). The hit distributions are well described for the first and third layer, but not for the second and fourth. Since the tag condition for FTS will be, that if a hit occurs in one of the FTS layers then the event is tagged, it may be better just to show tagged and not tagged events. This is done in figure 8.2, where the four layers are shown, but the 2, 3 and 4 hits are combined in one bin. The description is getting better, but the layer 2 ( $z = 28$  m) shows no response in data for the high energy period of 2007, therefore the description is not reliable and thus it was not used in this analysis. The layer 4 ( $z = 92$  m) shows also a deviation between data and MC, probable because the simulation is getting worse with increasing distance from the interaction point. Therefore only the layers 1 and 3 are used.

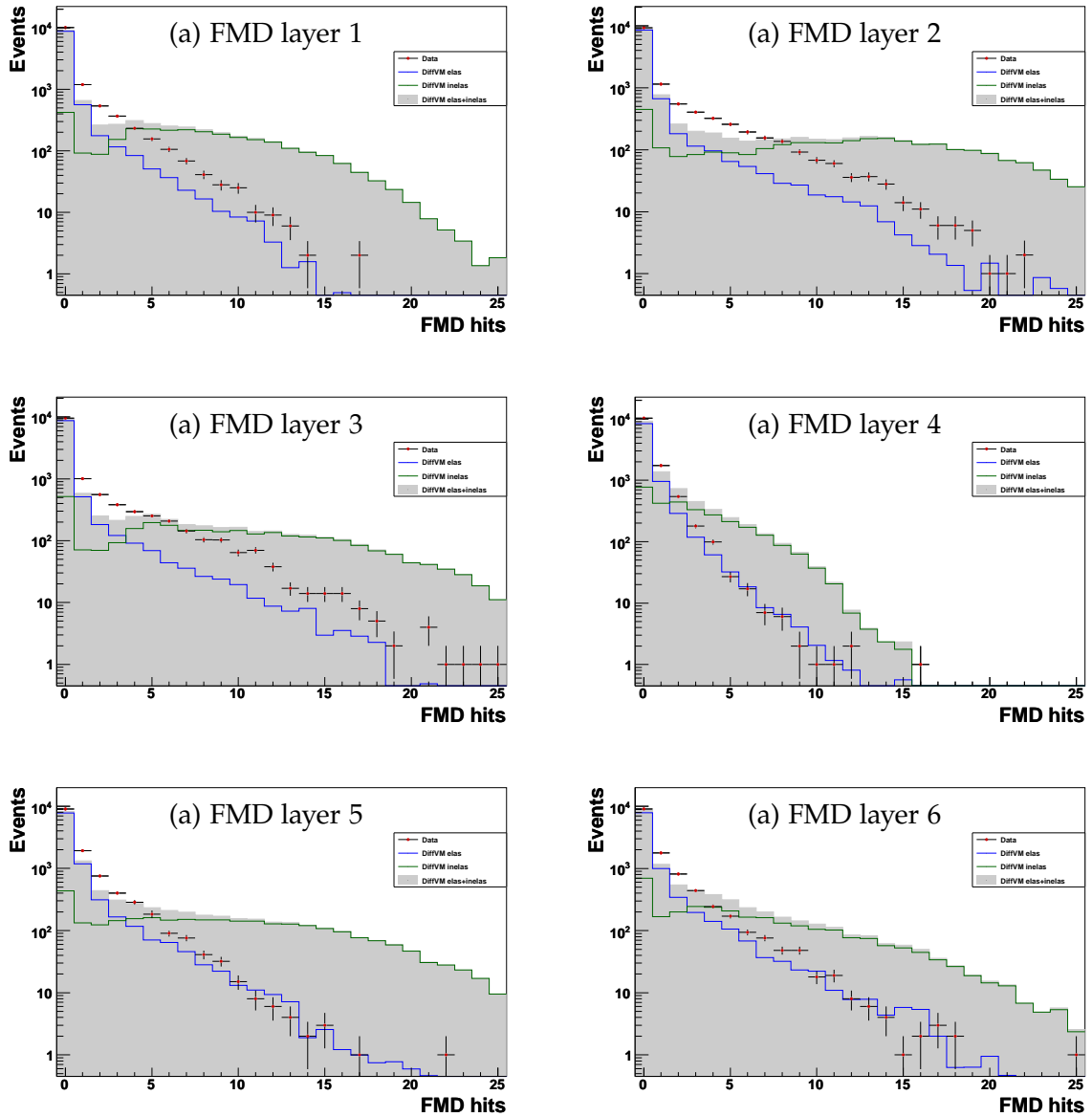


Figure 8.3: Hit multiplicity for FMD layer 1 to 6 (a)-(f). Only high energy data are displayed. The green histograms represent the elastic, the blue the inelastic MC events; stacked they give the grey filled histograms. The red points are the data.

In figure 8.3 the hit distribution for the 6 FMD layers are given. As can be seen the simulation and the data show totally different behaviour for large hit numbers. It seems that the data follow more the distribution of the elastic simulation than of the combination of elastic and inelastic MC. Therefore the FMD is not taken into the tag condition.

The conditions for the separate sub-detectors are summarised in table 8.1. Combined with a logical “OR”-statement, they form the statement to decide between tagged and not

forward detector	tag condition	description
PLUG	$E_{\text{PLUG}} > 4 \text{ GeV}$	Energy in PLUG calorimeter larger then 4 GeV
LAr10	$E_{\text{LAr10}} > 0.5 \text{ GeV}$	Energy in all cells within $\theta < 10^\circ$ of LAr calorimeter larger then 0.5 GeV
FMD	-	Is not used (see text)
FTS	$N_{\text{hit}}^{\text{FTS}} > 0$	At least one hit in the 8 layers (4 each) of the FTS station at 26 m (layer 1) and 53 m (layer 3).

Table 8.1: Conditions for the forward sub-detectors for tagging as inelastic events. Combined with a logical “OR”-statement they form the tagging condition.

tagged events.

## 8.2 Unfolding Procedure

As described above, both elastic and inelastic processes contribute to tagged events. This means one can write the number of tagged events  $N_{\text{tag}}$  as

$$N_{\text{tag}} = \varepsilon_{\text{tag}}^{\text{elas}} N_{\text{elas}} + \varepsilon_{\text{tag}}^{\text{inelas}} N_{\text{inelas}}, \quad (8.1)$$

where  $N_{\text{elas}}$  and  $N_{\text{inelas}}$  represent the number of elastic and inelastic events and  $\varepsilon_{\text{tag}}^{\text{elas}} = \frac{N_{\text{tag}}^{\text{elas}}}{N_{\text{elas}}}$ ,  $\varepsilon_{\text{tag}}^{\text{inelas}} = \frac{N_{\text{tag}}^{\text{inelas}}}{N_{\text{inelas}}}$  stand for the tagging efficiencies for the two processes. In the same way, it is possible to write the number of not tagged events  $N_{\text{tag}}^{\text{not}}$  as

$$N_{\text{tag}}^{\text{not}} = (1 - \varepsilon_{\text{tag}}^{\text{elas}}) N_{\text{elas}} + (1 - \varepsilon_{\text{tag}}^{\text{inelas}}) N_{\text{inelas}}. \quad (8.2)$$

For simplification one can write equation 8.1 and 8.2 in matrix notation and get

$$\begin{pmatrix} N_{\text{tag}} \\ N_{\text{tag}}^{\text{not}} \end{pmatrix} = \underbrace{\begin{pmatrix} \varepsilon_{\text{tag}}^{\text{elas}} & \varepsilon_{\text{tag}}^{\text{inelas}} \\ 1 - \varepsilon_{\text{tag}}^{\text{elas}} & 1 - \varepsilon_{\text{tag}}^{\text{inelas}} \end{pmatrix}}_A \begin{pmatrix} N_{\text{elas}} \\ N_{\text{inelas}} \end{pmatrix} \quad (8.3)$$

If one think of the physical process as they really happen, for example the proton is scattered elastically but it can either be tagged or not, then the equation (8.1) should be read from the right to the left side. Similar can be said about equation (8.2). Unfortunately only the left side, the numbers of tagged and not tagged events, can be measured. But the number of elastic and inelastic events are of interest and have to be determined. Therefore the equation (8.3) has to be read from the left to the right side, so one is forced to invert the matrix  $A$ . The inversion can be done analytically. The components for  $N_{\text{elas}}$  and  $N_{\text{inelas}}$

written separately give

$$N_{\text{elas}} = N_{\text{sig}} \frac{f_{\text{tag}} - \epsilon_{\text{tag}}^{\text{inelas}}}{\epsilon_{\text{tag}}^{\text{elas}} - \epsilon_{\text{tag}}^{\text{inelas}}} \quad \text{and} \quad N_{\text{inelas}} = N_{\text{sig}} \frac{\epsilon_{\text{tag}}^{\text{elas}} - f_{\text{tag}}}{\epsilon_{\text{tag}}^{\text{elas}} - \epsilon_{\text{tag}}^{\text{inelas}}}, \quad (8.4)$$

where  $N_{\text{sig}} = N_{\text{tag}} + N_{\overline{\text{tag}}} = N_{\text{elas}} + N_{\text{inelas}}$  is the total number of  $J/\psi$  extracted from the fits (chapter 6.1.4) and  $f_{\text{tag}} = \frac{N_{\text{sig}}^{\text{tag}}}{N_{\text{sig}}}$  the fraction of tagged events in the data sample. Since the physical processes, as they really take place, can be expressed by reading equation (8.3) from right to the left side, it follows that the tagging efficiencies cannot be measured from data, thus only the calculation from MC samples is possible.

Above described deconvolution procedure can now be done in each of the analysis bins, thus in  $|t|$  and  $W_{\gamma p}$  bins.

### 8.3 Forward Tagging Efficiencies

In figure 8.4 and 8.5 the tagging efficiencies for the combined tagging conditions given in table 8.1 are shown as a function of  $|t|$  (c.f. fig 8.4) and  $W_{\gamma p}$  (c.f. fig 8.5) for the high energy sample. Figure (a) shows the elastic tag efficiency  $\epsilon_{\text{tag}}^{\text{elas}}$ , (b) the inelastic tag efficiency  $\epsilon_{\text{tag}}^{\text{inelas}}$  and (c) the fraction of tagged events in data  $f_{\text{tag}}$ .

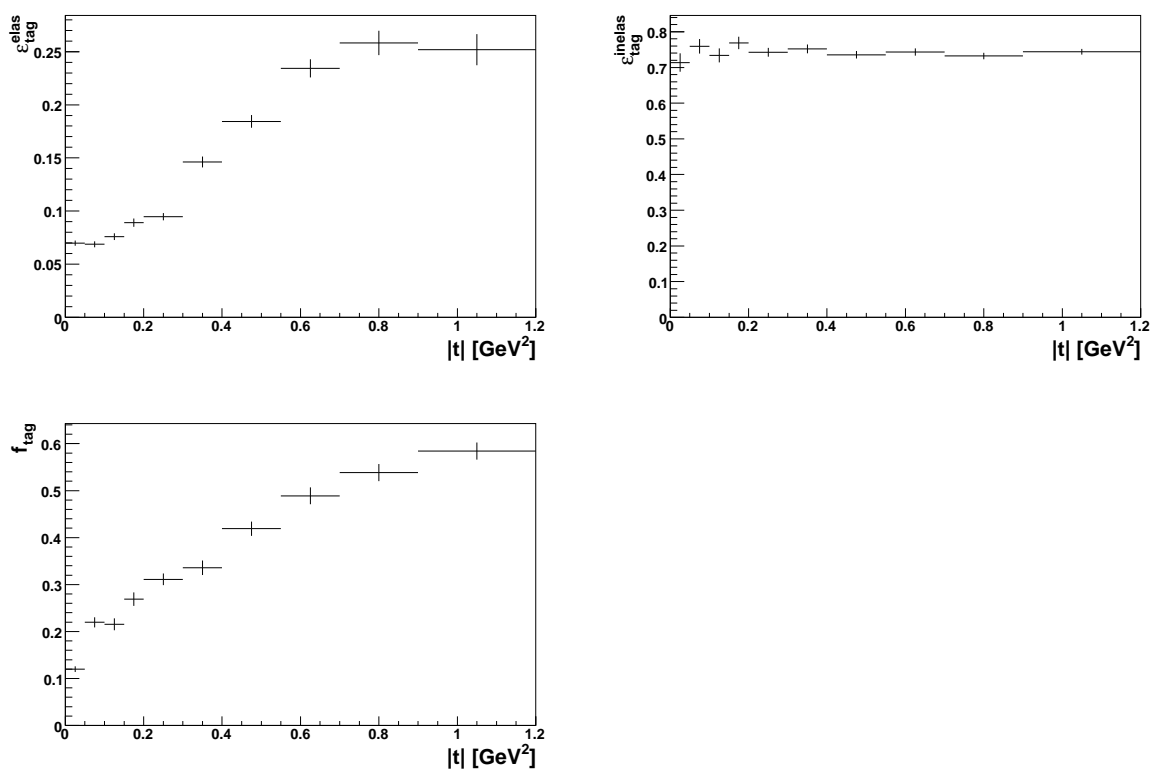


Figure 8.4: Tagging efficiencies showed for elastic,  $\epsilon_{\text{tag}}^{\text{elas}}$ , (a), inelastic,  $\epsilon_{\text{tag}}^{\text{inelas}}$ , (b) and the fraction of tagged events in data,  $f_{\text{tag}}$ , is given in (c) as a function of  $|t|$  for the high energy period.

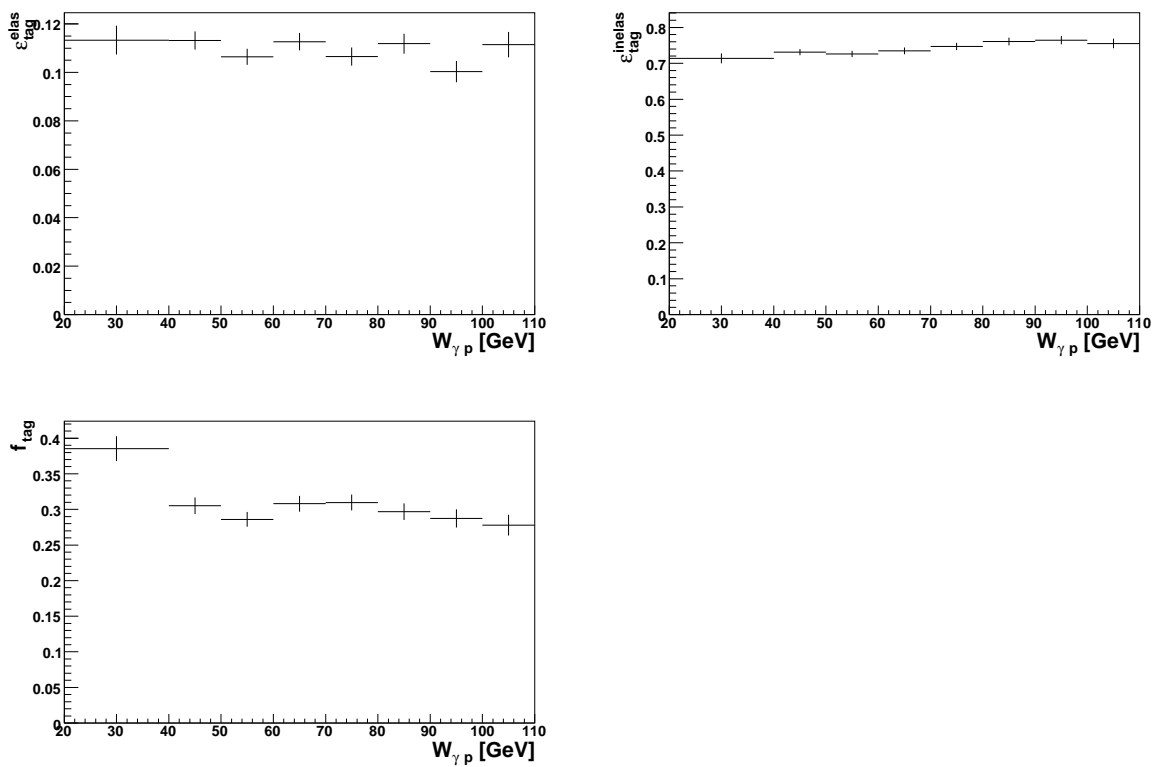


Figure 8.5: Tagging efficiencies showed for elastic,  $\epsilon_{\text{tag}}^{\text{elas}}$ , (a), inelastic,  $\epsilon_{\text{tag}}^{\text{inelas}}$ , (b) and the fraction of tagged events,  $f_{\text{tag}}$ , in data is given in (c) as a function of  $W_{\gamma p}$  for the high energy period.

# Chapter 9

## Cross Section Calculation and Results

In this chapter all distributions, variables and numbers are combined to calculate the differential photon proton cross sections of elastic  $J/\psi$  photoproduction with subsequent decay in an electron positron pair ( $J/\psi \rightarrow e^+e^-$ ) for the three different energy regions high, medium and low of the year 2007. Cross sections are quoted for  $Q_e^2 < 1 \text{ GeV}^2$  and with  $W_{\gamma p}$  and  $|t|$  phase space as displayed in table 6.3. The definition of the differential cross section in  $|t|$ ,  $\frac{d\sigma}{d|t|}$ , is given by the equation

$$\frac{d\sigma}{d|t|} = \frac{1}{\Phi_\gamma^T} \frac{N_{J/\psi}^{\text{elas}}(\Delta t)}{\mathcal{L} \mathcal{BR} \varepsilon_{\text{tot}} \Delta t}. \quad (9.1)$$

Where  $N_{J/\psi}^{\text{elas}}(\Delta t)$  means the number of elastic  $J/\psi$  events in the bin  $\Delta t$ , given by the deconvolution of the fitted number of selected events.  $\Phi_\gamma^T$  represents the integrated photon flux over the  $W_{\gamma p}$  region used for the analysis. It is calculated from equation 2.5 by numerical integration. The values are listed in Appendix E.  $\mathcal{L}$  is the integrated luminosity listed in table 5.1.  $\mathcal{BR}$  means the branching ration of the decay  $J/\psi \rightarrow e^+e^-$ , which is according to [36] ( $5.94 \pm 0.06$ )%.  $\varepsilon_{\text{tot}}$  is the total efficiency from the geometric acceptance, reconstruction, selection cuts multiplied by the trigger efficiency and  $\Delta t$  is the bin width of the used  $|t|$  bins.

The cross section depending on  $W_{\gamma p}$  is given by

$$\sigma(W_{\gamma p}) = \frac{1}{\Phi_\gamma^T} \frac{N_{J/\psi}^{\text{elas}}(\Delta W_{\gamma p})}{\mathcal{L} \mathcal{BR} \varepsilon_{\text{tot}}}, \quad (9.2)$$

where  $N_{J/\psi}^{\text{elas}}(\Delta W_{\gamma p})$  is the number of elastic  $J/\psi$  events in the bin  $\Delta W_{\gamma p}$ .

In figure 9.1(a) the cross section as a function of  $|t|$  and in (b) of  $W_{\gamma p}$  for the three energy regions are drawn. The red circles represent the high energy, the blue squares the medium and the green triangles the low energy data. The error bars only show the statistic error. In figure also the earlier H1 measurement [4] is given, represented by the black stars (statistical and systematic errors are combined shown for the H1 points).

A fit is performed according to chapter 2 with the functions

$$\frac{d\sigma_{\gamma p}}{d|t|} = \frac{d\sigma_{\gamma p}}{d|t|} \Big|_{|t|=0} e^{-b_0|t|}, \quad \text{and} \quad \sigma_{\gamma p}(W_{\gamma p}) = \sigma_0 W_{\gamma p}^\delta$$

and yields to

$$\frac{d\sigma_{\gamma p}}{d|t|} \Big|_{|t|=0} = (250.9 \pm 17.3(\text{stat.})) \text{ nb/GeV}^2 \quad \text{and} \quad b_0 = (4.7 \pm 0.3(\text{stat.})) \text{ GeV}^{-2},$$

$$\sigma_0 = (2.2 \pm 0.9(\text{stat.})) \text{ nb} \quad \text{and} \quad \delta = 0.79 \pm 0.10.$$

There is a good agreement between the earlier H1 [4] and this measurement visible in figure 9.1. The phase space for the  $W_{\gamma p}$  plots are the same  $|t| < 1.2 \text{ GeV}^2$  for both analysis, but for the  $|t|$  plots the phase space of the H1 measurement is  $40 \text{ GeV} < W_{\gamma p} < 160 \text{ GeV}$  and therefore different. Thus a comparison of  $d\sigma_{\gamma p}/d|t| \Big|_{|t|=0}$  is not reasonable.

Also the fit values of this earlier H1 measurement, which are

$$b_0 = (4.630 \pm 0.060(\text{stat.})_{-0.163}^{+0.043}(\text{syst.})) \text{ GeV}^{-2} \quad \text{and} \quad \delta = 0.75 \pm 0.03(\text{stat.}) \pm 0.03(\text{syst.}),$$

are within the errors comparable.

Additional the overview of the elastic cross section in the photoproduction region for all vector mesons including this measurement as a function of  $W_{\gamma p}$  is given in figure 9.2.

## 9.1 Systematic Uncertainties

The error bars in figure 9.1 only take the statistical error into account. But also the systematic uncertainties have to be considered. Possible sources for systematic uncertainties are

- trigger efficiency
- single track efficiency
- branching ratio
- luminosity
- MC statistic
- fit
- decay of  $\psi(2S) \rightarrow J/\psi$ .

But within the scope of this thesis, they could not have been studied.

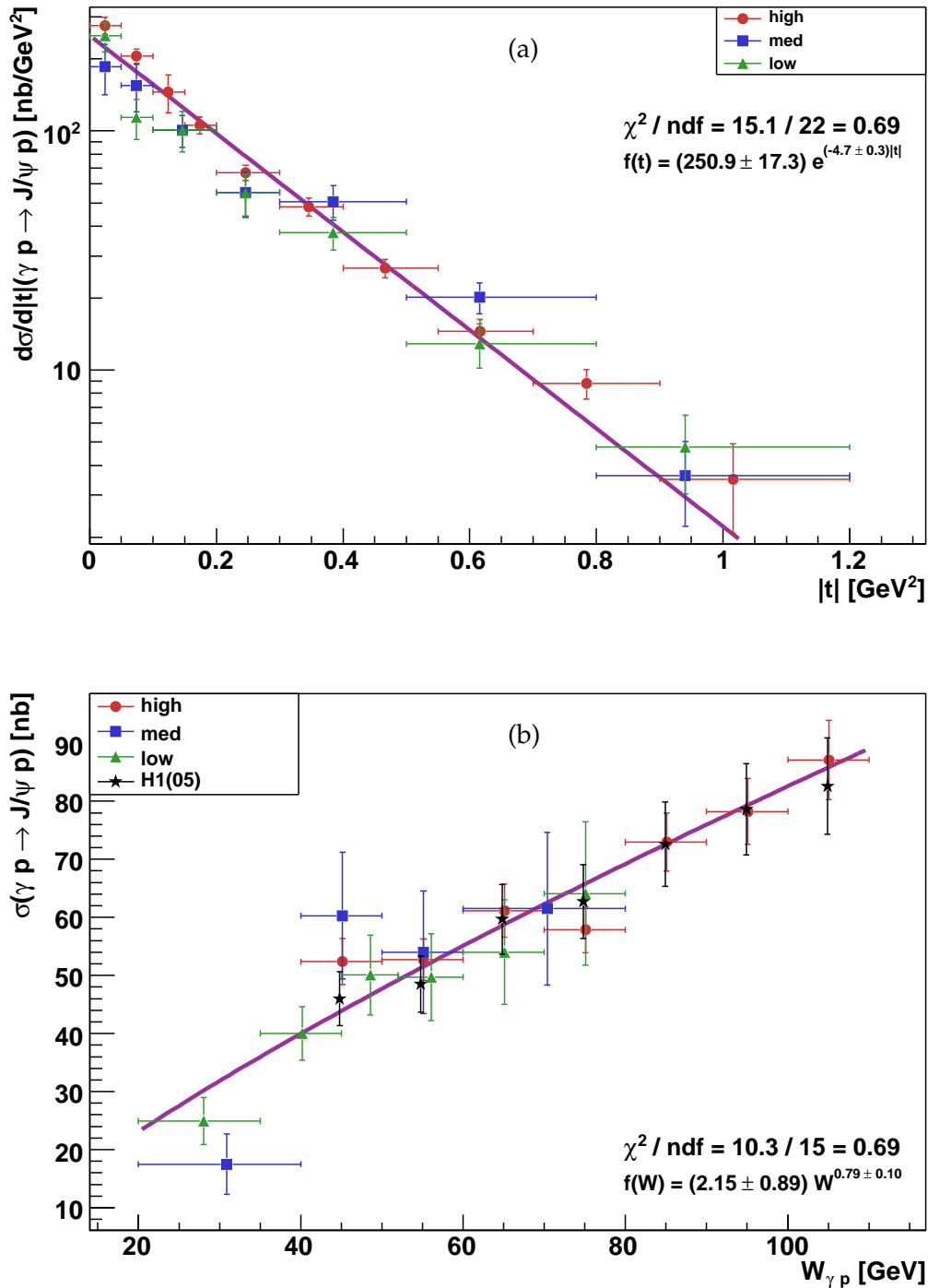


Figure 9.1: Differential cross section as a function of  $|t|$  (a) and  $W_{\gamma p}$  (b). All three energy regions are shown, red circles represent the high energy period, blue squares the medium energy and the low energy is given by the green triangles. Also the earlier measurement of H1 [4] is shown as black stars in (b). (For the fit only measured points from this analysis are used.)

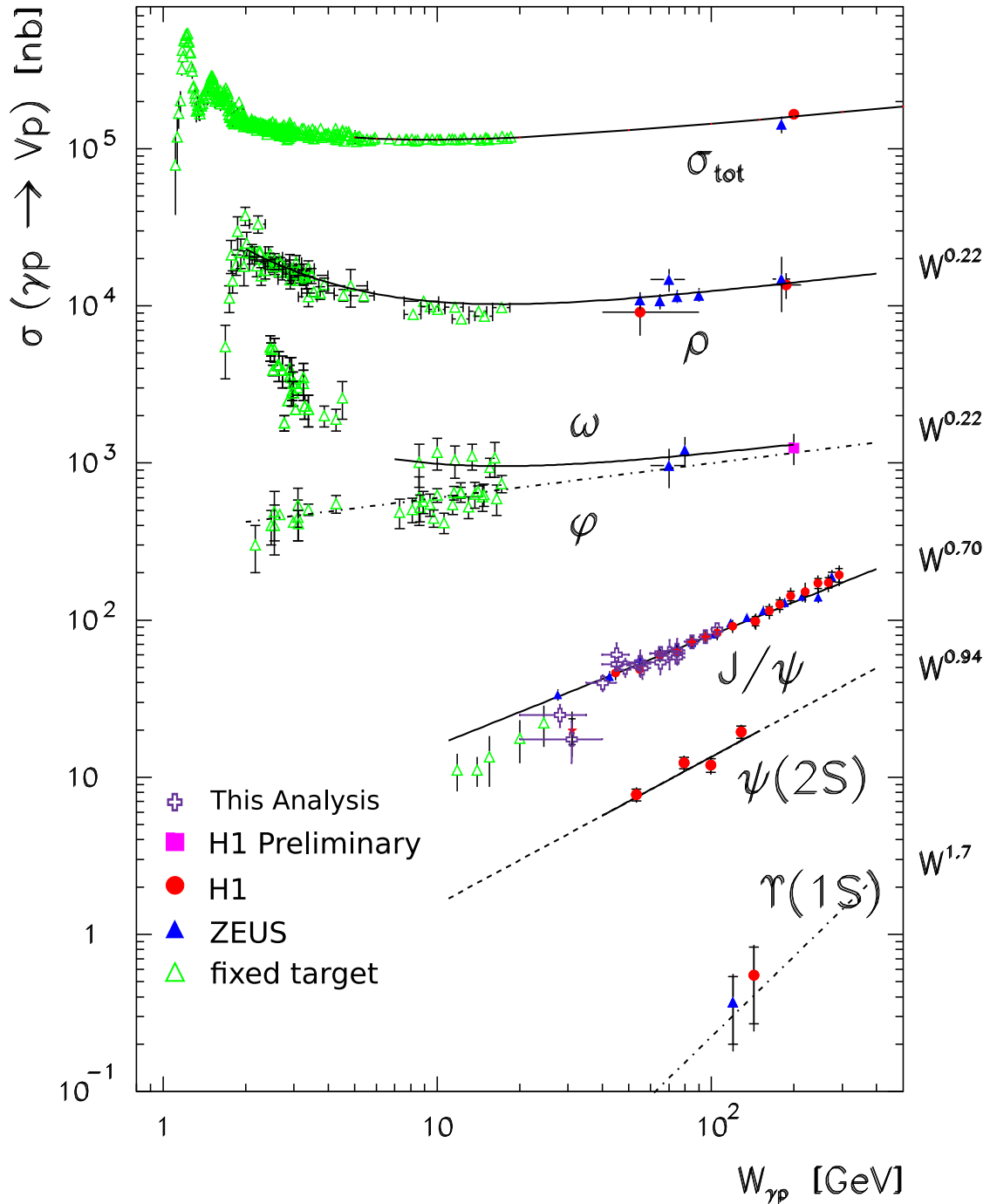


Figure 9.2: Overview of the dependence of the elastic cross section of several vector meson production and of the total photon proton cross section on the center of mass energy in the photon proton rest frame  $W_{\gamma p}$  in the photoproduction region. The purple crosses represent this measurement, whereas all three energy regions are considered. The other parts of the figure are taken from [1]. The green triangles originate from fix-target experiments; for  $J/\psi$  they are extracted from [2, 3]<sup>2</sup>. The red circles represent the H1 measurements; for  $J/\psi$  they are extracted from [4] and the red star measurement point is coming from [5]. The blue triangles represent the Zeus measurement; for  $J/\psi$  they are extracted from [6].

## 9.2 Summary

In this thesis it was shown that the low and medium energy runs of HERA II from the year 2007 can be used to determine  $\sigma_{\gamma p}(W_{\gamma p})$  in regions of the phase space between fix-target and earlier HERA data with reasonable precision. The results determined here agree with the expected  $W_{\gamma p}$ - and  $t$ -dependence of  $J/\psi$  production.



# Appendix A

## Bin Centre Correction

To make a fit and also by drawing a graph of the cross section, the position of the points on the abscissa has to be known. Problematic is that some bins are very broad and thus the question is, where one should put the measured point of this bin, is not so easy to answer. If the shape of the function is flat then the point should lay exactly in the middle of the bin. But if this is not the case then the bin centre will wander. The processes which correct this effect is called bin centre correction.

The expectation value of a bin centre can be written as

$$\langle t \rangle = \frac{\int_{t_{\min}}^{t_{\max}} dt t \frac{d\sigma}{dt}}{\int_{t_{\min}}^{t_{\max}} dt \frac{d\sigma}{dt}}. \quad (\text{A.1})$$

Here the differential cross section,  $\frac{d\sigma}{dt}$ , represents the real probability density function according to which the bin centre should be arranged. Since exactly this function should be measured, it is necessary to make an assumption about the shape (the normalisation cancels because of the fraction in equation (A.1)). And then the proper parameters of the function will be found iteratively. First fitting the data with the assumed function and afterwards rearrange the bin centre according to the found function.

The distribution for the cross section in  $|t|$  was chosen as an exponential

$$\frac{d\sigma}{d|t|} \propto e^{c|t|},$$

and for  $W_{\gamma p}$  as a power function

$$\sigma(W) = W^\delta.$$

But that's not the whole story, the photon flux has to be considered as well for the  $W_{\gamma p}$

correction, because it depends on the  $W_{\gamma p}$  itself. The expectation value for  $W_{\gamma p}$  is<sup>1</sup>

$$\langle W \rangle = \frac{\int_{W_{\min}}^{W_{\max}} dW W \Phi_{\gamma}^T(W) \sigma(W)}{\int_{W_{\min}}^{W_{\max}} dW \Phi_{\gamma}^T(W) \sigma(W)}, \quad (\text{A.2})$$

where  $\Phi_{\gamma}^T(W) = \int_{Q_{\min}^2}^{Q_{\max}^2} dQ^2 \mathcal{F}_{\gamma}^T(W, Q^2)$ . Although it is possible to integrate this term analytically, it is determined by numerical integration.

---

<sup>1</sup>For clarity of the equation  $W \equiv W_{\gamma p}$  is used.

## Appendix B

### Kinematical limit for $Q^2$

Here a short calculation for the  $Q_{\min}^2 \simeq m_e^2 \frac{y^2}{1-y}$  is given in the region of  $m_e \ll |\vec{k}|, |\vec{k}'|$ , where  $m_e$  the electron mass,  $\vec{k}$  and  $\vec{k}'$  the momentum of the incoming and outgoing electron represent.

(1) First  $Q^2$  is defined as

$$Q^2 \equiv -q^2 = -(k - k')^2 \quad (\text{B.1})$$

$$= -[2m_e + 2k \cdot k'] \quad \text{with } k \cdot k' = E_e E'_e - |\vec{k}| |\vec{k}'| \cos \Theta_e \quad (\text{B.2})$$

$$\text{and } E_e = \sqrt{|\vec{k}|^2 + m_e^2} \simeq |\vec{k}| + \frac{1}{2} \frac{m_e^2}{|\vec{k}|} + \dots \quad (\text{B.3})$$

if only the first two orders in the expansion of  $E_e$  is taken one gets

$$Q^2 \simeq -2 \left[ m_e^2 - |\vec{k}| |\vec{k}'| (1 - \cos \Theta_e) - \frac{1}{2} m_e^2 \left( \frac{|\vec{k}|}{|\vec{k}'|} + \frac{|\vec{k}'|}{|\vec{k}|} \right) \right], \quad \text{if } m_e \ll |\vec{k}|, |\vec{k}'| \quad (\text{B.4})$$

(2)  $Q^2$  is going to be minimal, if  $1 - \cos \Theta_e \rightarrow 0$  which is equivalent with  $\Theta_e \rightarrow 0$ , therefore

$$Q_{\min}^2 \simeq -2 \left[ m_e^2 - \frac{1}{2} m_e^2 \left( \frac{|\vec{k}|}{|\vec{k}'|} + \frac{|\vec{k}'|}{|\vec{k}|} \right) \right], \quad \text{if } m_e \ll |\vec{k}|, |\vec{k}'| \quad (\text{B.5})$$

(3) The above term can be rewritten with the use of

$$y = \frac{P \cdot q}{P \cdot k} = 1 - \frac{P \cdot k'}{P \cdot k} \quad (\text{B.6})$$

where

$$P \cdot k' = E_P E'_e - |\vec{P}| |\vec{k}'| \cos \Theta_1 \quad \text{with } \Theta_1 = \pi - \Theta_e, \text{ so } \cos \Theta_1 \rightarrow -1 \quad (\text{B.7})$$

and by using equation B.3 and only take the leading order, it is possible to write

$$\frac{P \cdot k'}{P \cdot k} \simeq \frac{2|\vec{P}||\vec{k}'|}{2|\vec{P}||\vec{k}|} = \frac{|\vec{k}'|}{|\vec{k}|}, \quad \text{if } m_e \ll |\vec{k}|, |\vec{k}'| \quad (\text{B.8})$$

(4) And the combination of equation B.5, B.6 and B.8 leads to

$$Q_{\min}^2 \simeq m_e^2 \frac{y^2}{1-y}, \quad \text{if } m_e \ll |\vec{k}|, |\vec{k}'| \quad (\text{B.9})$$

# Appendix C

## Minimal $W_{\gamma p}$

$W_{\gamma p}$  is given in chapter 2 as

$$W_{\gamma p} \simeq \sqrt{ys - Q^2}.$$

In the kinematical region of photoproduction,  $Q^2$  is small and therefor can be neglected. And  $y$  can be reconstructed by  $y_{mh} = \frac{E_\psi - p_{\psi,z}}{2E_e}$  with  $E_\psi$  the energy of the  $J/\psi$  and  $p_{\psi,z}$  the z-component of the momentum of the  $J/\psi$ . Whereas

$$E_\psi - p_{\psi,z} = (E_1 - p_{1,z}) + (E_2 - p_{2,z}) \text{ with } p_{i,z} = |\vec{p}| \cos \Theta_i \quad (\text{C.1})$$

$$\text{with } E_i \simeq |\vec{p}_i| \text{ for small masses} \quad (\text{C.2})$$

$$\simeq p_{1,t} \frac{1 - \cos \Theta_1}{\sin \Theta_1} + p_{2,t} \frac{1 - \cos \Theta_2}{\sin \Theta_2} \quad (\text{C.3})$$

$$(\text{C.4})$$

$p_i$  and  $E_i$  are the momentum and the energy of the decay products of the  $J/\psi$ . Together with  $s \simeq 4E_p E_e$  one can write

$$W_{\gamma p} = \sqrt{2E_p \left[ p_{1,t} \frac{1 - \cos \Theta_1}{\sin \Theta_1} + p_{2,t} \frac{1 - \cos \Theta_2}{\sin \Theta_2} \right]}. \quad (\text{C.5})$$

The minimum of  $W_{\gamma p}$  can therefore be calculated by

$$W_{\gamma p}^{\min} = \sqrt{4E_p p_{t,\min} \frac{1 - \cos \Theta_{\min}}{\sin \Theta_{\min}}}. \quad (\text{C.6})$$

In figure C.1 a graph of  $W_{\gamma p}^{\min}$  according to formula C.6 in the variables  $p_{t,\min}$  and  $\Theta_{\min}$  is showed. (For the energy of the proton was 920 GeV used.) One can see that the lower limit of  $W_{\gamma p}$  is given by the minimal transverse momentum of the track  $p_{t,\min}$  and of the minimal  $\Theta$  angle. The minimal angel is  $20^\circ$  given by the acceptance of the CJC and the minimal transverse momentum is 0.8 GeV given by the  $J/\psi$  finder and by the trigger.

For the three energy regions the theoretical minimal values which could be reached are summarised in table C.1.

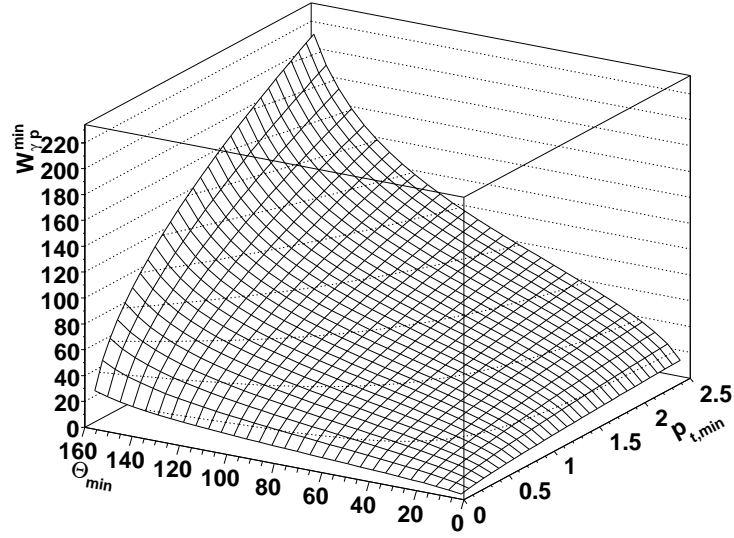


Figure C.1:  $W_{\gamma p}^{min}$  plotted against  $p_{t,min}$  and  $\Theta_{min}$  of the tracks of the electrons.

energy region	proton energy [GeV]	$W_{\gamma p}^{min}$ GeV
high	920	23
medium	575	18
low	460	16

Table C.1: Overview of the minimal values of  $W_{\gamma p}$  which could theoretically reached.

# Appendix D

## Cross Section Values

Data set	$W_{\gamma p}$ [GeV]	$\langle W_{\gamma p} \rangle$ [GeV]	$\sigma$ [nb]
high	40 – 50	45.1	$52.4 \pm 4.0$
	50 – 60	55.1	$52.7 \pm 3.6$
	60 – 70	65.1	$61.2 \pm 4.5$
	70 – 80	75.1	$57.9 \pm 3.9$
	80 – 90	85.1	$73.0 \pm 5.0$
	90 – 100	95.1	$78.2 \pm 5.6$
	100 – 110	105.1	$87.1 \pm 6.8$
medium	20 – 40	30.9	$17.5 \pm 5.2$
	40 – 50	45.1	$60.3 \pm 10.9$
	50 – 60	55.1	$54.0 \pm 10.6$
	60 – 80	70.4	$61.5 \pm 13.1$
low	20 – 35	28.0	$24.9 \pm 4.0$
	35 – 45	40.2	$40.0 \pm 4.6$
	45 – 52	48.6	$50.1 \pm 6.8$
	52 – 60	56.1	$49.7 \pm 7.5$
	60 – 70	65.1	$54.0 \pm 9.0$
	70 – 80	75.1	$64.1 \pm 12.4$
	80 – 100	90.3	$68.1 \pm 25.6$

Table D.1: Photoproduction cross section for the elastic process  $\gamma p \rightarrow J/\psi p$  in bins of  $W_{\gamma p}$  for  $|t| < 1.2$  GeV for the three different energy regions (high, medium and low) from the runs of the year 2007.  $\langle W_{\gamma p} \rangle$  indicates the bin centre value in the  $W_{\gamma p}$  range considered. Only the statistical error on the cross section is given.

Data set	$ t $ [GeV <sup>2</sup> ]	$\langle  t  \rangle$ [GeV <sup>2</sup> ]	$\sigma$ [nb/GeV <sup>2</sup> ]
high	0.00 – 0.05	0.02	276.1 ± 22.7
	0.05 – 0.10	0.07	205.6 ± 13.9
	0.10 – 0.15	0.12	145.3 ± 26.0
	0.15 – 0.20	0.17	105.8 ± 8.6
	0.20 – 0.30	0.25	67.0 ± 4.9
	0.30 – 0.40	0.35	48.2 ± 4.2
	0.40 – 0.55	0.47	26.7 ± 2.4
	0.55 – 0.70	0.62	14.5 ± 1.8
	0.70 – 0.90	0.78	8.8 ± 1.2
	0.90 – 1.20	1.02	3.5 ± 1.4
medium	0.00 – 0.05	0.02	185.5 ± 44.1
	0.05 – 0.10	0.07	154.9 ± 34.9
	0.10 – 0.20	0.15	100.8 ± 15.3
	0.20 – 0.30	0.25	55.4 ± 11.9
	0.30 – 0.50	0.38	50.6 ± 8.3
	0.50 – 0.80	0.62	20.1 ± 3.0
	0.80 – 1.20	0.94	3.6 ± 1.4
low	0.00 – 0.05	0.02	249.5 ± 35.3
	0.05 – 0.10	0.07	113.8 ± 21.7
	0.10 – 0.20	0.15	101.1 ± 19.5
	0.20 – 0.30	0.25	55.1 ± 11.0
	0.30 – 0.50	0.38	37.6 ± 5.9
	0.50 – 0.80	0.62	12.9 ± 2.7
	0.80 – 1.20	0.94	4.8 ± 1.7

Table D.2: Differential photoproduction cross section for the elastic process  $\gamma p \rightarrow J/\psi p$  measured in  $|t|$  bins in the kinematical ranges of  $W_{\gamma p}$  as given in table 6.3 for the three different energy regions (high, medium and low) from the runs of the year 2007.  $\langle |t| \rangle$  indicates the bin centre value in the  $|t|$  range considered. Only the statistical error on the cross section is given.

# Appendix E

## Photon Flux Factors

Data set	$W_{\gamma p}$ [GeV]	$\langle W_{\gamma p} \rangle$ [GeV]	$\Phi_{\gamma}^T$
high	40 – 50	45.1	0.022
	50 – 60	55.1	0.017
	60 – 70	65.1	0.014
	70 – 80	75.1	0.012
	80 – 90	85.1	0.010
	90 – 100	95.1	0.008
	100 – 110	105.1	0.007
	40 – 110		0.091
medium	20 – 40	30.9	0.073
	40 – 50	45.1	0.021
	50 – 60	55.1	0.016
	60 – 80	70.4	0.024
	20 – 80		0.134
low	20 – 35	28.0	0.058
	35 – 45	40.2	0.024
	45 – 52	48.6	0.013
	52 – 60	56.1	0.012
	60 – 70	65.1	0.013
	70 – 80	75.1	0.010
	20 – 80		0.130

Table E.1: Photon flux factors  $\Phi_{\gamma}^T$  used to calculate the  $\gamma p$  from the  $ep$  cross section for the three different energy regions (high, medium and low). The lines at the end of every data set period are used to calculate the differential cross section as functions of  $|t|$ , whereas the others are used to calculate the cross section as a function of  $W_{\gamma p}$ .



# Bibliography

- [1] H1 Collaboration, *Combined H1 ZEUS Figures on Heavy Quark Physics*, [http://www-h1.desy.de/h1work/hq/figures/vmall\\_col.ps](http://www-h1.desy.de/h1work/hq/figures/vmall_col.ps).
- [2] B. H. Denby et al., E516 Collaboration, “*Inelastic and Elastic Photoproduction of  $J/\psi(3097)$* ”, *Phys. Rev. Lett.*, **52**(10) 795–798, Mar 1984.
- [3] M. Binkley et al., E401 Collaboration, “ *$J/\psi$  Photoproduction from 60 to 300 GeV/c*”, *Phys. Rev. Lett.*, **48**(2) 73–76, Jan 1982.
- [4] The H1 Collaboration, “*Elastic  $J/\psi$  production at HERA*”, *European Physical Journal C*, **46** 585–603, June 2006.
- [5] C. Adloff et al., [H1], “*Elastic photoproduction of  $J/\psi$  and  $Y$  mesons at HERA*”, *Phys. Lett.*, **B483** 23–35, 2000.
- [6] S. Chekanov et al., ZEUS Collaboration, “*Exclusive photoproduction of  $J/\psi$  mesons at HERA*”, *The European Physical Journal C - Particles and Fields*, **24** 345–360, 2002.
- [7] A. Gute A. Levy, M. Ferstl, *Lectures on QCD*, chapter Low-x physics at HERA, pages 347–477, *Lecture Notes in Physics*. Springer Berlin / Heidelberg, 1997.
- [8] V. A. Saleev and A. V. Shipilova, “*Relative contributions of fusion and fragmentation mechanisms in  $J/\psi$  photoproduction at high energy*”, *Physical Review D (Particles and Fields)*, **75**(3) 034012, 2007.
- [9] Niklaus E. Berger, *Measurement of Diffractive  $\phi$  Meson Photoproduction at HERA with the H1 Fast Track Trigger*, PhD thesis, ETH, 2007.
- [10] G. Alberi and G. Goggi, “*Diffraction of subnuclear waves*”, *Physics Reports*, **74**(1) 1 – 207, 1981.
- [11] Gerhard A. Schuler and Torbjörn Sjöstrand, “*Towards a complete description of high-energy photoproduction*”, *Nuclear Physics B*, **407**(3) 539 – 605, 1993.
- [12] Ursula Bassler and Gregorio Bernardi, “*On the Kinematic Reconstruction of Deep Inelastic Scattering at HERA: the  $\Sigma$  Method*”, *NUCL.INSTRUM.METH.A*, **361** 197, 1995.
- [13] Vladimir Chekelian, *The Structure of Hadrons*, In *Lepton-Photon Interactions, LP '97*, page 29, 1998.
- [14] C. F. V. Weizsäcker, “*Ausstrahlung bei Stößen sehr schneller Elektronen*”, *Zeitschrift für Physik*, **88** 612–625, September 1934.

- [15] E. J. Williams, "Nature of the High Energy Particles of Penetrating Radiation and Status of Ionization and Radiation Formulae", *Physical Review*, **45** 729–730, May 1934.
- [16] V. M. Budnev, I. F. Ginzburg, G. V. Meledin and V. G. Serbo, "The two-photon particle production mechanism. Physical problems. Applications. Equivalent photon approximation", *Physics Reports*, **15**(4) 181 – 282, 1975.
- [17] I. Abt, et al., H1 Collaboration, "The H1 detector at HERA", *Nuclear Instruments and Methods in Physics Research Section A: Accelerators, Spectrometers, Detectors and Associated Equipment*, **386**(2-3) 310 – 347, 1997.
- [18] I. Abt, et al., H1 Collaboration, "The tracking, calorimeter and muon detectors of the H1 experiment at HERA", *Nuclear Instruments and Methods in Physics Research Section A: Accelerators, Spectrometers, Detectors and Associated Equipment*, **386**(2-3) 348 – 396, 1997.
- [19] R. D. Appuhn, et al., H1 Collaboration, "The H1 lead/scintillating-fibre calorimeter", *Nuclear Instruments and Methods in Physics Research Section A: Accelerators, Spectrometers, Detectors and Associated Equipment*, **386**(2-3) 397 – 408, 1997.
- [20] F.D. Aaron, et al., H1 Collaboration, "Measurement of the proton structure function  $F_L(x, Q^2)$  at low  $x$ ", *Physics Letters B*, **665**(4) 139 – 146, 2008.
- [21] H. Cronstrm, et. al., H1 Collaboration, "The H1 forward muon spectrometer", *Nuclear Instruments and Methods in Physics Research Section A: Accelerators, Spectrometers, Detectors and Associated Equipment*, **340**(2) 304 – 308, 1994.
- [22] T. Nicholls, et al., H1 Collaboration, "Performance of an electromagnetic lead/scintillating-fibre calorimeter for the H1 detector", *Nuclear Instruments and Methods in Physics Research Section A: Accelerators, Spectrometers, Detectors and Associated Equipment*, **374**(2) 149 – 156, 1996.
- [23] A. Baird, E. Elsen, Y. H. Fleming, M. Kolander, S. Kolya, D. Meer, D. Mercer, J. Naumann, P. R. Newman, D. Sankey, A. Schoening, H. C. Schultz-Coulon and Ch Wissing, "A Fast High Resolution Track Trigger for the H1 Experiment", *IEEE Transactions on Nuclear Science*, **48** 1276, 2001.
- [24] A. Mastroberardino B. List, "DIFFVM - A Monte Carlo generator for diffractive processes in ep scattering", DESY-PROC-1999-02, page 396, 1999, Hamburg (DESY).
- [25] Michael Steder, *Measurement of Inelastic Charmonium Production at HERA*, PhD thesis, Universität Hamburg, 2008.
- [26] M. Williams, M. Bellis and C. A. Meyer, "Multivariate side-band subtraction using probabilistic event weights", ArXiv e-prints, September 2008.
- [27] Max Christoph Urban, *The new CIP2k z-Vertex Trigger for the H1 Experiment at HERA*, PhD thesis, Universität Zürich, 2004.
- [28] Max Urban, *Trigger Elements from the CIP2k*, 2004.

- [29] Lee West, *How to use Heavy Flavour Working Group Track, Muon and Electron Selection Code H1PHAN Version  $\geq$  3.00/00*, 2007.
- [30] *Track Selection: H1TrkFinder*,  
<https://www-h1.desy.de/icas/oop/finders/lwtrackfinder/trackfinderframe.ps.gz>.
- [31] Roger A. Halg, *Electron Identification in Heavy Quark Decays at the H1 Experiment*, Master's thesis, ETH, 2007.
- [32] Michel Sauter, H1UserSoftLeptonId (Soft electron identification),  
<https://www-h1.desy.de/icgi-h1wiki/moin.cgi/AnalysisSoftware/Meeting2008-03-26?action=AttachFile&do=get&target=H1UserSoftLeptonId.pdf>, 2008.
- [33] D. Kirkby W. Verkerke, *RooFit Users Manual v2.91*,  
[ftp://root.cern.ch/root/doc/RooFit\\_Users\\_Manual\\_2.91-33.pdf](ftp://root.cern.ch/root/doc/RooFit_Users_Manual_2.91-33.pdf), 2008.
- [34] H1 Collaboration, "*D\* production at low  $Q^2$  with the H1 detector at HERA*", 34th International Conference on High Energy Physics, ICHEP2008, 2008.
- [35] H1 Collaboration, "*Measurement of  $K^{*\pm}$  Production in Deep Inelastic ep Scattering at HERA*", H1 preliminary, submitted to 34th International Conference on High Energy Physics, ICHEP2008, 2008.
- [36] C. Amsler et al., "*Review of Particle Physics*", *Physics Letters B*, **667**(1-5) 1 – 6, 2008, Review of Particle Physics.



# Acknowledgements

I would like to thank Prof. Christoph Grab for making this diploma thesis possible and supervising me. A very special thank goes to my tutor Michel Sauter for his strong support during the whole time, for having always an open ear for questions and for introducing me in the daily business of a particle physicist. I also would like to thank Michael Steder for allowing me to use his preselected data, Mira Krämer for processing the MC files, Tobias Zimmerman, Benno List, Andreas W. Jung and Niklaus Berger for unhesitatingly answering questions. A special thank goes to all people in the particle physics institute in Zürich, especially Lea, Giovanna, Lukas, Alex, Andrea, Michael and Carmelo, for the pleasant lunch and coffee break time. On a more personal note I want to thank my family and friends for their support and encouragement during these past years of studies.